

ABSTRACT

MALLIK, SUSHMIT. A Small Airborne Particulate Matter Sensor using a Parabolic Mirror. (Under the direction of Dr. John F. Muth).

Airborne particulate matter poses a serious threat to human health. Traditionally, particulate matter sensors have been rather large, expensive and stand-alone instruments, or hand held instruments that require operator attention to make measurements for occupational exposure. Very few attempts have been made to make wearable particulate monitors. The principle barrier has been keeping the cost of the system low and reducing the size of the sensor while maintaining sensitivity. Another consideration for wearable particulate sensor is keeping power consumption of the system low to reduce the need recharging or battery replacement.

In this thesis, the design of a low power, wearable and a relatively low cost sensor is explored. From Mie scattering theory, it is known that the forward scattered light at small angles is of maximum intensity. It's been a challenge to isolate these small angle pulses from the main laser beam. In this sensor design, a reflective optical design is proposed which collects the small angle light pulses and uses them to count the number of particles, while keeping the dimensions of the sensor small. In this design, tests showing detection of particle sizes ranging from 1.5 μm to 6.39 μm , with a theoretical lower limit of 0.19 μm . Sensitivity to smoke particles is also demonstrated. A prototype was interfaced to a microcontroller and LCD display.

© Copyright 2014 by Sushmit Mallik

All Rights Reserved

A Small Airborne Particulate Matter Sensor using a Parabolic Mirror

by
Sushmit Mallik

A thesis submitted to the Graduate Faculty of
North Carolina State University
in partial fulfillment of the
requirements for the degree of
Master of Science

Electrical Engineering

Raleigh, North Carolina

2014

APPROVED BY:

Dr. John F. Muth
Committee Chair

Dr. Robert Kolbas

Dr. Edward Grant

DEDICATION

To my parents and brother.

BIOGRAPHY

Sushmit Mallik was born on October 12, 1990 in Kolkata, West Bengal, India. He completed his schooling from Kendriya Vidyalaya, No.1, Salt Lake, Kolkata (West Bengal), India. He completed his undergraduate degree (B.Tech in Electronics & Communication Engineering) at SRM University, Chennai, India in May, 2012. In Spring, 2011, he was a visiting student at The University of Wisconsin, Madison, USA. He developed an interest in Optoelectronics and Device Physics during that time. He was a Student Research Assistant under Dr. Kenneth Wong at The University of Hong Kong, where he worked on his senior year project on Distributed Fiber Optic Temperature and Strain Sensing, from December 2011 – March 2012. He is currently pursuing a M.S. in Electrical Engineering from North Carolina State University. Currently, he is working on developing low cost airborne particulate matter sensors which can be low power and have a wearable form factor. His research interests include optical sensors, novel electro-optical materials, device & process engineering and interaction of light with nanostructures and their applications.

ACKNOWLEDGMENTS

I thank Dr. Muth for trusting me and my abilities for this project. I have learnt a lot under your guidance. Working with you for the last two years has been an enriching experience, academically and otherwise. I thank Dr. Kolbas and Dr. Grant for accepting to serve as committee members.

I would like to thank my labmates, Yifan Wang, Benjamin Decker, Abhishek Malhotra, Leandra Brickson, Wencong Zhu, Bryan Maione, Subharup Gupta Roy, David Luo for their awesome support, in classes and research. A special thanks to Yifan, Ben, Abhishek and Leandra for spending a lot of time with me to provide feedback for my ideas, numerous times. Asia Gray-Battle, it wouldn't have been possible to complete the project without your support with the lab equipment and orders. Thanks to Joe Matthews and Rudy Salas for all the lab training and electronic components. I thank Fabian for helping me out with SolidWorks in the beginning. Ankit, Subharup, Shikhar, Swapnil, Bharat, Sahil, Mihir, Raunaq, Subbu, Hardik, Nehal, Kirti, Anand, Gaurav; thank you for making this journey a joyous and memorable affair. Special thanks to Swapnil Shah for helping me out and giving valuable advice during circuit design and debugging. Thank you Joyeeta Sharma, for your constant belief in me and never ending support, which kept me going in difficult times. Thank you, mom & dad and my little brother. Your love gave me strength and conviction to complete the project.

TABLE OF CONTENTS

LIST OF FIGURES	vi
Chapter 1 Introduction	1
1.1. Fundamentals of particulate matter exposure	2
1.2. Effect of particulate matter (PM) on health	4
1.3. Outline of thesis	6
REFERENCES	7
Chapter 2 Literature Review	8
2.1. Commercial sensors	20
2.1.1. Dylos sensor test	24
REFERENCES	27
Chapter 3 Light Scattering Theory	29
3.1. Introduction	29
3.2. Rayleigh Theory	35
3.3. Mie Theory	36
3.4. Light Scattering Behavior	38
REFERENCES	43
Chapter 4 System Level Design	44
4.1. Optics	45
4.2. Circuit Design	53
4.2.1. Transimpedance amplifier	54
4.2.2. Bandwidth and SNR calculations	59
4.3. Embedded systems/interfaces	61
4.3.1. ADC considerations	62
4.3.2. Static threshold counting algorithm	62
4.3.3. Dynamic threshold counting algorithm	65
4.3. CAD/Prototyping	69
4.4. Power consumption estimate	74
REFERENCES	75
Chapter 5 Experiments & Analysis of Results	76
5.1. Initial bench-top experiment	76
5.2. Sensor design test	81
5.3. Statistical counting	91
5.4. Test with different flow rates	93
5.5. Test with smoke	99
5.6. Test after interfacing with TI MSP 430 microcontroller and LCD	101
REFERENCES	107
APPENDICES	108
Appendix A – MATLAB Code	109
Appendix B – MSP 430 Code	111

LIST OF FIGURES

Figure 1.1 Effect of PM	2
Figure 1.2 Comparison of PM 10 and PM 2.5	3
Figure 2.1 Schematic of the A10	10
Figure 2.2 Schematic of the Palas WELAS 2100	11
Figure 2.3 Schematic of the Grimm 1.109 OPC	12
Figure 2.4 TEM₀₀ experimental apparatus	13
Figure 2.5 TEM₀₀ power output during particle passage	14
Figure 2.6 Schematic of multiple ratio system	15
Figure 2.7 Schematic of CPC	16
Figure 2.8 Schematic of the system	18
Figure 2.9 Schematic of a low cost particulate matter counter	19
Figure 2.10 The RTI MPEM device	20
Figure 2.11 Dylos sensor	21
Figure 2.12 Sharp GP2Y1010AU0F Optical Dust Sensor	22
Figure 2.13 Shinyei PPD42NS Dust Sensor	23
Figure 2.14 Dylos sensor data (Absolute counts)	25
Figure 2.15 Dylos sensor data (mass/volume)	26
Figure 3.1 Light scattering by an induced dipole moment due to an incident EM wave	30
Figure 3.2 Coordinate geometry for Rayleigh and Mie scattering	32
Figure 3.3 Angular scattering intensity	33
Figure 3.4 Dependence of scattering cross-section vs scattering angle	39
Figure 3.5 Extinction efficiency vs size parameter	40
Figure 3.6 Differential scattering cross-section vs Particle diameter	42
Figure 4.1 System level block diagram	44
Figure 4.2 Intensity distribution of scattered light for 2.5 μm particle with $n = 1.3$	46
Figure 4.3 Intensity distribution of scattered light for 5 μm particle with $n = 1.33$	46
Figure 4.4 Intensity distribution of scattered light for 10 μm particle with $n = 1.33$	47
Figure 4.5 Angular distribution of scattered intensity for 2.5 μm water drop	48
Figure 4.6 Angular distribution of scattered intensity for 5 μm water drop	48
Figure 4.7 Angular distribution of scattered intensity for 10 μm water drop	48
Figure 4.8 Schematic of the parabolic mirror	49
Figure 4.9 Key specifications of the parabolic mirror	49
Figure 4.10 Optical design of the sensor	50
Figure 4.11 Laser diode	51
Figure 4.12 Spot size in ideal case	52
Figure 4.13 Spot size in reality	52
Figure 4.14 Thorlabs FDS1010 photodiode	53
Figure 4.15 Responsivity of FDS1010	53
Figure 4.16 Circuit level block diagram	53
Figure 4.17 Transimpedance Circuit with Modeled Elements	55
Figure 4.18 TI MSP 430 G2553	61

Figure 4.19 Static threshold counting algorithm.....	63
Figure 4.20 Code profiling results.....	64
Figure 4.21 ADC response.....	66
Figure 4.22 MSP430 interfacing to LCD.....	67
Figure 4.23 Dynamic threshold counting algorithm flowchart.....	69
Figure 4.24 Top part of the prototype.....	70
Figure 4.25 Bottom part of the prototype.....	70
Figure 4.26 Bottom part of the prototype (Back Side view).....	70
Figure 4.27 1 st 3D printed prototype.....	70
Figure 4.28 CAD design 2nd version.....	71
Figure 4.29 Tapered Flow inlet.....	71
Figure 4.30 3D printed version.....	72
Figure 4.31 Total forward field after scattering by on-axis and off-axis particles.....	73
Figure 5.1 Initial bench top experiment.....	76
Figure 5.2 Response with flow OFF.....	77
Figure 5.3 Response with flow ON.....	78
Figure 5.4 Response with Si amplified photodetector.....	79
Figure 5.5 FFT of Response with Si amplified photodetector.....	81
Figure 5.6 Schematic of the sensor test setup.....	82
Figure 5.7 SKC cyclone: relation between input flow rate and 50% cut-off point of particle size.....	84
Figure 5.8 Extrapolated particle size vs flow rate curve.....	85
Figure 5.9 Picture of the sensor test setup.....	85
Figure 5.10 Response when flow is OFF.....	86
Figure 5.11 Light scattering response with $R_F = 270 \text{ k}\Omega$	87
Figure 5.12 Light scattering response with $R_F = 330 \text{ k}\Omega$	87
Figure 5.13 FFT when flow is OFF.....	89
Figure 5.14 FFT of light scattering response with $R_F = 270 \text{ k}\Omega$	89
Figure 5.15 FFT of light scattering response with $R_F = 330 \text{ k}\Omega$	90
Figure 5.16 Probability distribution with $R_F = 270 \text{ k}\Omega$	91
Figure 5.17 Probability distribution with $R_F = 330 \text{ k}\Omega$	92
Figure 5.18 Probability distribution for small particles transitioning various intensities of a focused Gaussian beam.....	93
Figure 5.19 Measurements for water particles.....	94
Figure 5.20 Comparative FFT analysis.....	96
Figure 5.21 Comparative FFT analysis (Zoomed in version).....	97
Figure 5.22 Signal peak due to individual particle.....	98
Figure 5.23 Test result from smoke experiment.....	100
Figure 5.24 Probability distribution with smoke particles.....	100
Figure 5.25 Test with microcontroller.....	102
Figure 5.26 Noise when microcontroller is OFF.....	103
Figure 5.27 Noise when microcontroller is ON.....	104
Figure 5.28 Result of test using microcontroller.....	106

Chapter 1 Introduction

The advent of rapid prototyping methods and inexpensive off the shelf components, low power microcontrollers, low power sensors has resulted in a remarkable growth of the wearable electronics industry [1]. This growth fuels the need of wearable sensors. Personalized health care and monitoring has emerged as one of the grand challenges for engineering in recent times because the high healthcare and related monitoring equipment costs has been a limiting factor in its effectiveness. A personal sensor that can monitor exposure to particulate matter and provide real-time data analysis to the user is a direct application of a personalized health care and monitoring system. These sensors were perceived as stand – alone sensors, which has resulted in them being bulky and not suitable for personalized monitoring. Therefore, the commercially products available in the market for particulate matter sensing cannot be classified as truly wearable.

Rapid prototyping techniques like 3D printing, miniature fans, low power/small microcontroller packages, optics and peripheral electronics, it is possible to aggressively scale down the size of such sensors to a wearable form factor. In this thesis, the design and fabrication of such a sensor is explored.

1.1. Fundamentals of particulate matter exposure

Particulate matter is often abbreviated as PM and is defined as a complex mixture of extremely small particles and liquid droplets [2]. PM pollution is typically composed of components, including acids (such as nitrates and sulfates), organic chemicals, metals, and soil or dust particles. There is a direct correlation between the size of the particles and their potential for causing health problems. According to the EPA, the particles of sizes 10 μm or less pose the most severe threat because they generally pass through the throat and enter the lungs. This is visually shown in Figure 1.1 [4].

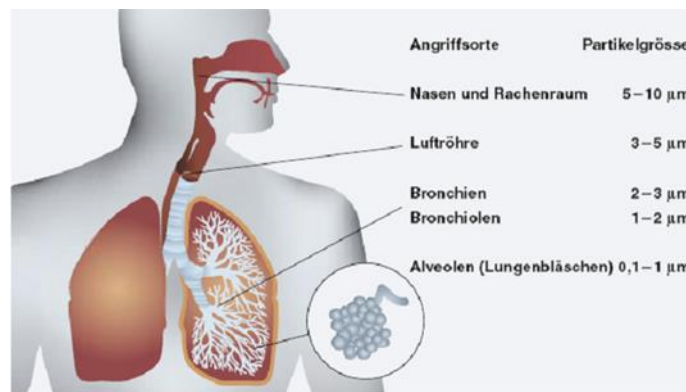


Figure 1.1 Effect of PM [4].

This can affect the heart and lungs adversely. The EPA groups PM pollution into two categories:

- ***Inhalable coarse particles:*** These particles are typically larger than 2.5 μm and less than 10 μm in size, often found near industrial areas or dusty roadways.

- ***Fine Particles:*** These particles are of the dimension, $2.5\ \mu\text{m}$ or smaller, typically found in smoke and haze. Such particles are directly emitted from sources like automobiles, factories, cooking stoves, forest fires, etc.

Particles with dimensions as small as $2.5\ \mu\text{m}$ can be pictured as being 30 times smaller than the diameter of the human hair which is about $70\ \mu\text{m}$ in size. Sometimes, these particles are known as *primary particles*, and are emitted directly from sources like construction sites, unpaved roads, fields, smokestacks or fires. Others form in complicated reactions in the atmosphere of chemicals such as sulfur dioxides and nitrogen oxides that are emitted from power plants, factories and automobiles. These are sometimes also known as *secondary particles*, which contribute to most of the PM pollution in USA. Figure 1.2 [3] illustrates the comparative particle sizes [3].

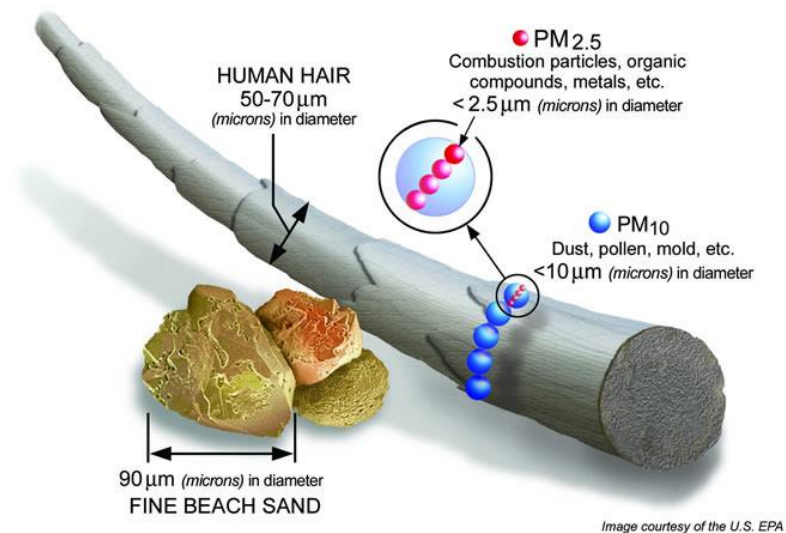


Figure 1.2 Comparison of PM 10 and PM 2.5 [3].

1.2. Effect of particulate matter (PM) on health

As mentioned in the previous section, the smaller the particulate matter size, the greater the chances of them travelling down the respiratory tract and hence a greater threat to health. They can get deep into the lungs and potentially into the blood stream. Exposure to such particles can affect both the lungs and the heart [2]. Numerous scientific studies have linked PM exposure to various kinds of health problems [3] such as:

- premature death in people with heart or lung disease
- nonfatal heart attacks
- irregular heartbeat
- aggravated asthma
- decreased lung function
- increased respiratory symptoms, such as irritation of the airways, coughing or difficulty breathing.

People with heart or lung diseases, children and older adults are the most likely to be affected by particle pollution exposure. The level of exposure to PM is also dependent on a person's physical activity. Increased physical activity and exercise causes people to breathe faster and as a result breathe in more particles than the normal rate. This presents a scenario where personal and wearable particulate matter sensors can be put use. For example, if someone is going for a run outside, he or she can track the PM exposure and might change course, if the person has a history respiratory ailments.

Older adults are also at risk if they have an undiagnosed heart or lung disease or diabetes. Even children are prone to enhanced exposure since their lungs are still developing and are more likely to have asthma or acute respiratory diseases, which can be aggravated when PM exposure is high. Next, the consequences of long term and short term exposures to PM exposure are described.

Long term exposures, are commonly experienced by people living in areas with persistently high PM concentrations, have been associated with problems such as reduced lung function and the development of bronchitis [3].

Short term exposures to particles can aggravate lung disease, causing asthma attacks and acute bronchitis and may also increase susceptibility to respiratory infections. It's also been related to heart attacks and arrhythmias [3]. Figure 1.1 [4] shows how deep into the respiratory tract, particulate matter can go based on their size.

1.3. Outline of thesis

In chapter 1, the issue of PM exposure and its effects on health were introduced and the motivation for a solution in a wearable form factor was discussed. Chapter 2 will go over the literature review. This will cover the overview of different sensing schemes used and their trade-offs. The commercially available sensors for particulate matter sensing will also be compared. In Chapter 3, the fundamentals of light scattering theory will be discussed and will be applied specifically to the light scattering by spherical particles of dimensions of our interests and, aided by simulations. Chapter 4 will discuss the system level design considerations. Chapter 5 will discuss the experiments and analysis. Finally, Chapter 6 will include the future work for improvement and conclusion.

REFERENCES

1. Michael Marschollek, Matthias Gietzelt, Mareike Schulze, Martin Kohlmann, Bianying Song, Klaus-Hendrik Wolf, “Wearable Sensors in Healthcare and Sensor-Enhanced Health Information Systems: All Our Tomorrows?”. *Health Inform Res.* 2012 June;18(2):97-104. <http://dx.doi.org/10.4258/hir.2012.18.2.97>.
2. <http://www.epa.gov/airquality/particulatematter/>
3. <http://www.naneos.ch/health.htm>
4. <http://www.epa.gov/airquality/particlepollution/basic.html>

Chapter 2 Literature Review

In this section, previous work in particulate matter sensing will be discussed and various optical sensing schemes will be highlighted with their pros and cons. Also, the performance of two popular commercial sensors, the high-end RTI MPEM and the mid-range Dylos sensor will be studied.

The optical sensing schemes can be fundamentally classified into two categories: optical scattering and optical extinction. In optical scattering, light, after being incident on a particle is scattered in a certain distribution of angles dictated by the Lorentz – Mie theory [1]. The scattered light pulses are then detected by a photo detector which converts the optical pulses into electrical signals. These signals are then counted per unit time to give an estimation of the particulate matter concentration.

In the optical extinction approach, the particles traversing through the light beam obstruct the beam. The transmitted light beam is monitored by a photo detector. The particles traversing through the beam cause momentary drops in the signal, which is counted in a similar way as the scattering method. Faxvog in 1972 showed an approach with the extinction method [2].

The UKA A10 [3], was designed and manufactured at the Universität Karlsruhe. Many other optical particle counters use similar designs. It uses an intense source of white light to illuminate a small sensing volume of located at the centre of the aerosol flow path. A combination of apertures placed in the optical path of the illumination and the two sensing (photomultiplier) branches, which are arranged at an observation angle of 90° opposing each other defines the sensing volume. The “twin-arm” design with two photomultiplier paths enables eliminating false signals due to particle traversing through the edge of the beam. This sensor detects, sizes and counts particles in a very precisely defined sensing volume which is much smaller than the flow path. However, concentration measurements require an independent calibration because they are based on the particle flux through that sensing volume. The schematic of this sensor is shown in Figure 2.1 [3].

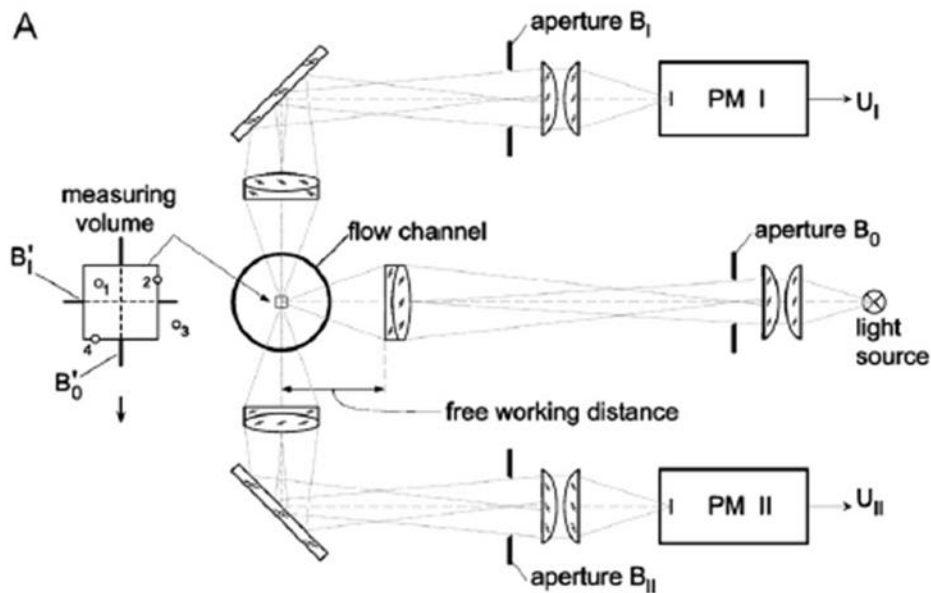


Figure 2.1 Schematic of the A10 [3].

The Palas WELAS 2100 [3] has a similar design as the A10, with a white light source and a scattering angle of 90° . A special feature of this design is the shape of its optical sensing volume which has a T-shaped cross-section, enabling the use of only one PMT instead of two as in the A10. This T-shape allows the elimination of false signals from particles travelling through edge of the beam based on the pulse length [3]. The WELAS devices are generally designed for portability, and the sensing volume of the Model 2100 is connected to the remainder of the device via optical fiber. The schematic of this sensor is shown in Figure 2.2 [3].

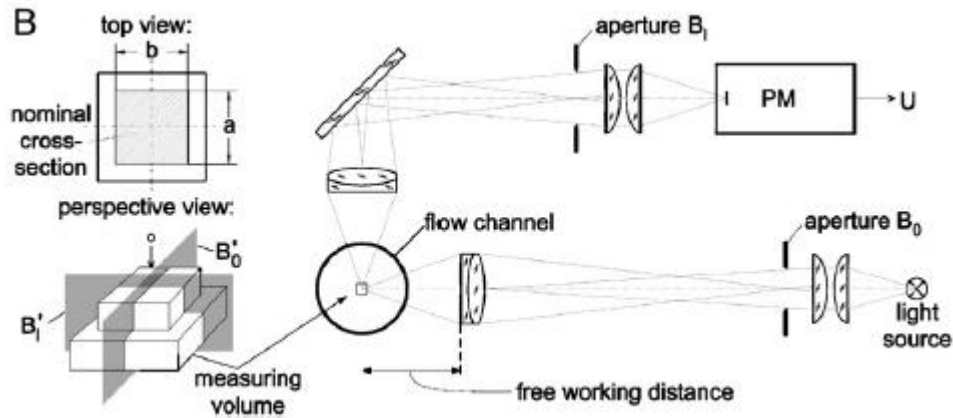


Figure 2.2 Schematic of the Palas WELAS 2100 [3].

The Grimm 1.109 uses a 683 nm laser diode to illuminate the aerosol beam and a parabolic to detect light pulses using a photodiode. The optical design collects the scattered light with a parabolic mirror (120°) on one side and an additional 18° on the opposing side. The wide angle optic increases the total amount of scattered light detected by the photosensor, close to the Rayleigh scattering domain. This results in an improvement in the signal to noise ratio. This leads to a decrease in the minimum particle size which can be detected (which is specified by the manufacturer as $0.25 \mu\text{m}$). It also smoothens out Mie scattering undulations caused by the monochromatic illumination, which reduces the sensitivity to particle shape.

As opposed to the two other OPCs, the 1.109 counts all particles entering the chamber. It measures absolute particle concentrations and should be more accurate in this regard. However, this design also increases the coincidence error and reduces the upper

concentration limit. This is not a problem because the device is primarily intended to measure environmental aerosols (which are usually at a lower concentration), whereas the other two are principally used for the measurement of industrial aerosols (e.g. filter testing). Figure 2.3 [3] shows the schematic of this sensor.

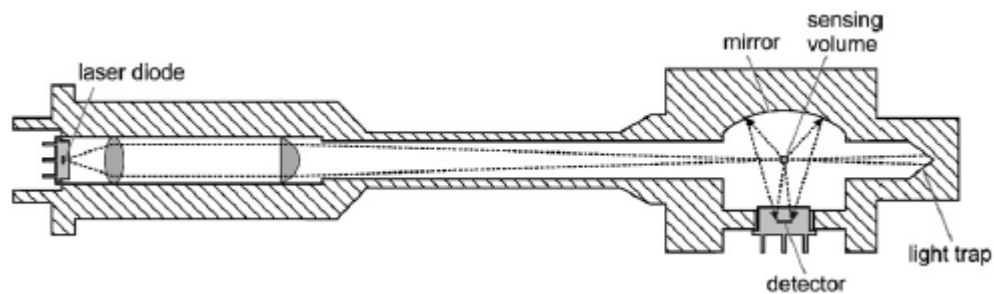


Figure 2.3 Schematic of the Grimm 1.109 OPC [3].

Another interesting variation of the optical extinction approach was shown by Shuster and Knollenberg by using an open cavity of a He-Ne gas laser oscillating at 632.8 nm was used to detect and size aerosol particles [4]. The laser behaves as a nonlinear amplifier of perturbations of the radiation within the resonant cavity. This mechanism can be used as a very sensitive technique for detecting and sizing aerosol particles. Particles injected in the radiation field of a laser cavity creates losses due to scattering, the net result being a power loss many times greater than that due to the geometric loss involved in classical extinction. The arrangement is shown in Figure 3. [4].

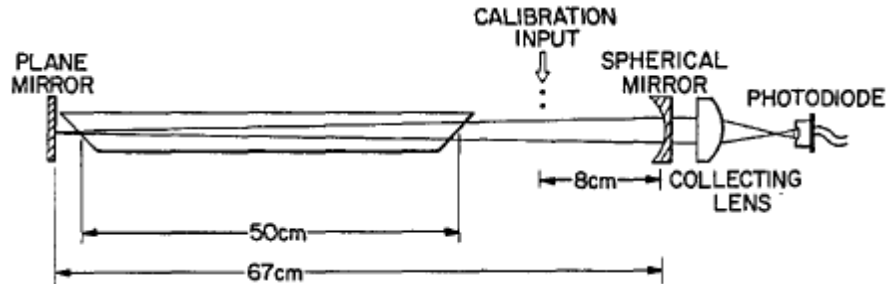


Figure 2.4 TEMoo experimental apparatus [4].

A He-Ne laser is used for introducing the beam in the open cavity bounded by a plane mirror and a spherical mirror. The plasma tube was used as a gain medium. The output of the laser was focused and monitored with a photodiode. The output of the photodiode was fed to an operational amplifier configured as a current-to-voltage converter. This output signal was AC-coupled to a pulse height detector. Particles (glass spheres) were dropped through the center of the laser beam by passing them through hypodermic needles positioned just above the beam center, about 8 cm from the mirror. The pulse amplitudes were measured digitally, while the pulse shape was recorded using an oscilloscope. The traversing particles cause extinction which cause a momentary drop in the output power. This is shown in Figure 2.5 [4].

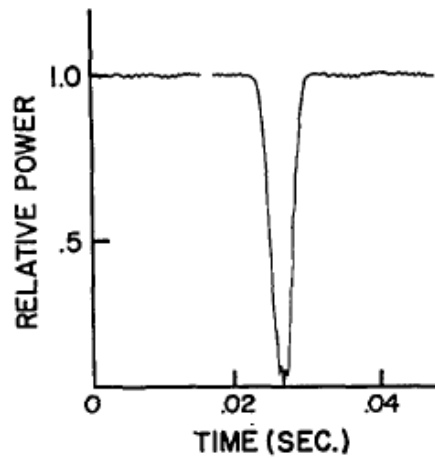


Figure 2.5 TEM₀₀ power output during particle passage [4].

This is a creative approach, which leverages the gain mechanism of a laser to achieve good signal to noise ratio, however the drawback is that it makes the design physically large and consumes a lot of power.

The Gaussian nature of the laser beam poses a problem in the accurate measurement of particles. Because of this, the system cannot differentiate between a small particle traversing through the center of the beam and a large particle passing through the edge of the beam, because the intensity of the scattered light is similar both cases. This problem can be eliminated by utilizing the ratio of light intensities scattered in two or more directions, cancelling the above mentioned effect. This was proposed by Hirleman et. al in 1980 [5]. The schematic is shown in Figure 2.6. [5].

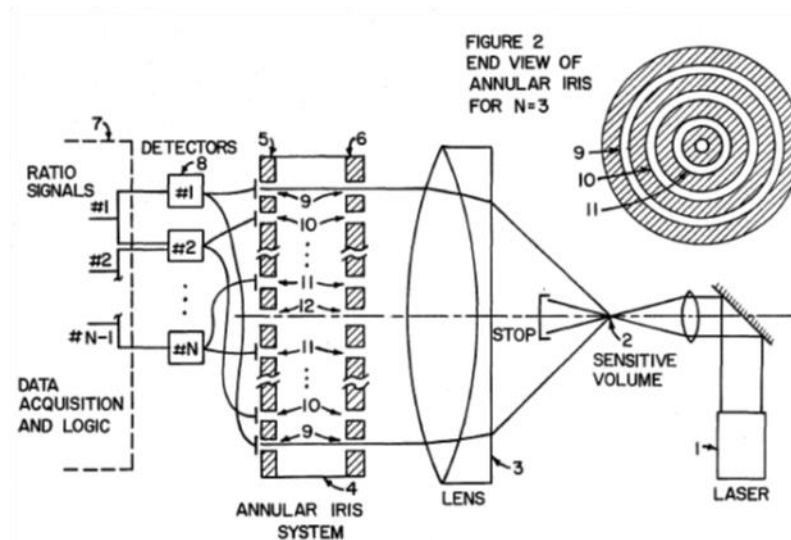


Figure 2.6 Schematic of multiple ratio system [5].

The system is made of a light source with a suitable wavelength. The beam is then confined to a small sensing volume using a converging lens. The scattered light is then collimated using another lens, which is passed through an annular iris system. This segregates the light scattered at various angles of interest. These optical pulses at various angles are then converted into electrical signals by an array of photodetectors. The output is then fed to a data acquisition system where the intensity ratios were computed and compared against a reference. The ratio of light scattered for at least one other pair of angles are simultaneously analyzed for each particle passing through the sensitive volume or particle sampling zone. The second ratio provides a consistency check on each particle analyzed. If the ratio measured at the second pair of angles corresponds to that predicted for the particle size within the valid range of the particular counter designed as indicated by the ratio measured at the primary pair of angles, then the particle can be counted. Otherwise, the particle would be

ignored as being a size outside the range of the counter where particles are accurately sized. The major advantage of this approach is the ability to negate the effects of Gaussian intensity profile of the laser which can lead to false measurements. However, such an approach consumes a sizeable space and the power consumption is on the higher side due to the use of multiple detectors.

There is another class of particle counters known as condensation particle counters (CPC). These instruments enlarge particles by condensation so that they can be detected by optical means. They can provide direct measurement of particle number concentrations. Such a CPC is shown by Hering et. al [6]. The schematic of this system is shown in Figure 2.7 [6].

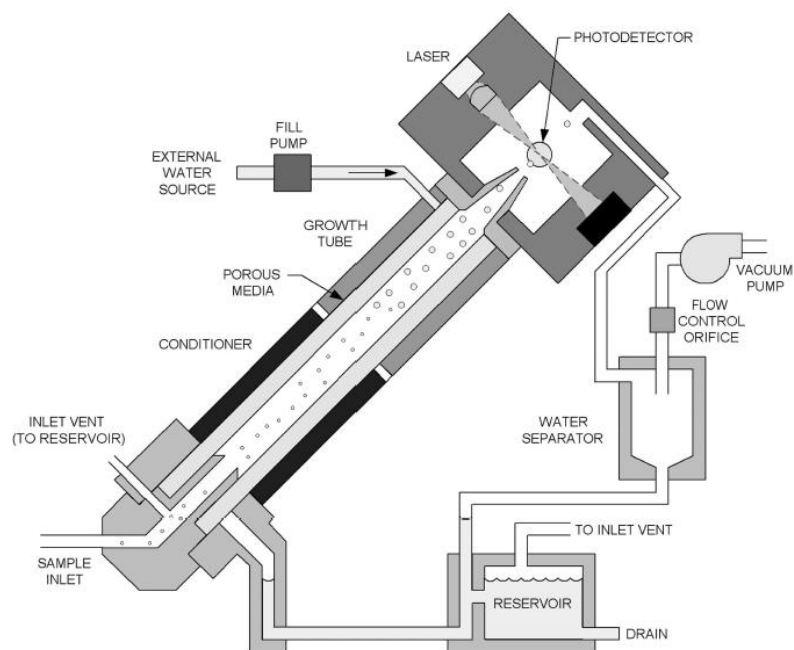


Figure 2.7 Schematic of CPC [6].

The major components of this system are the inlet, conditioner, growth tube, and optical head. The conditioner serves to normalize the temperature and relative humidity of the entering airflow. Particle activation and growth occurs in the growth tube. Once grown, particles are detected by right angle scattering within the optical head. The flow exits through a cooled water separator that drains to a waste water reservoir. The flow is monitored by means of a pressure drop across the downstream metering orifice whose temperature is held constant [6].

Particle counters have also been used for laser induced fluorescence applications [7]. The organic content of marine spray aerosols was probed using laser induced fluorescence, which excites the fluorescence of chlorophyll-a contained in the phytoplanktons. In-vivo chlorophyll-A has a main broad absorbance peak at ~440nm and two main fluorescence peaks at ~670 and ~720nm. The aerosol is probed with a laser having a wavelength in the range of 400-460nm to allow maximum absorption and induce a maximum yield of fluorescence. The instrument stimulates and collects a total fluorescence signal from each probed aerosol particle in order to determine the ratio of elastic scattered light at laser wavelength to fluoresced light. Simultaneously, it allows particle sizing through collection of the elastically scattered laser light, and a flux measurement by determining the rate of particles that pass. The schematic of the system is shown in Figure 2.8 [7].

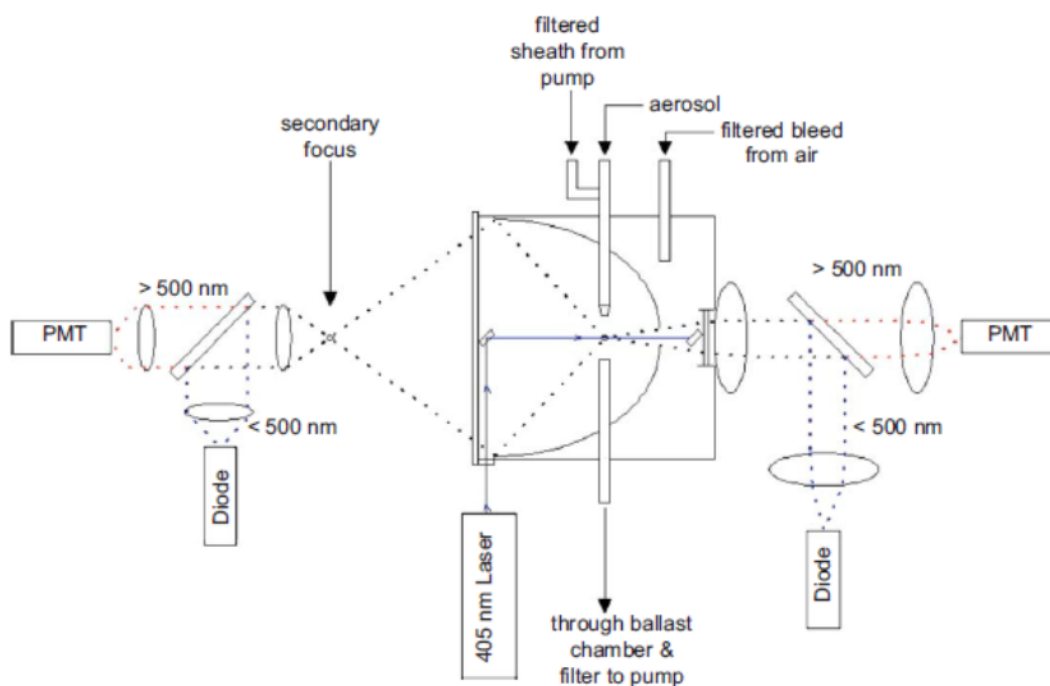


Figure 2.8 Schematic of the system [7].

The main advantage of this design is that it allows back and forward scattered light to be collected simultaneously. However, the fluorescence signature also has a very short lifetime on the order of nanoseconds making the fluorescence output almost simultaneous to the elastic scattered light signal. This necessitates the use of highly sensitive photomultiplier tubes (PMTs) to maximize signal to noise ratio, consuming a lot of space and power.

In recent times, there has been an interest in building low cost particulate matter sensors with small form factors. The schematic of a low cost particulate matter sensor [8] is shown in Figure 2.9 [8].

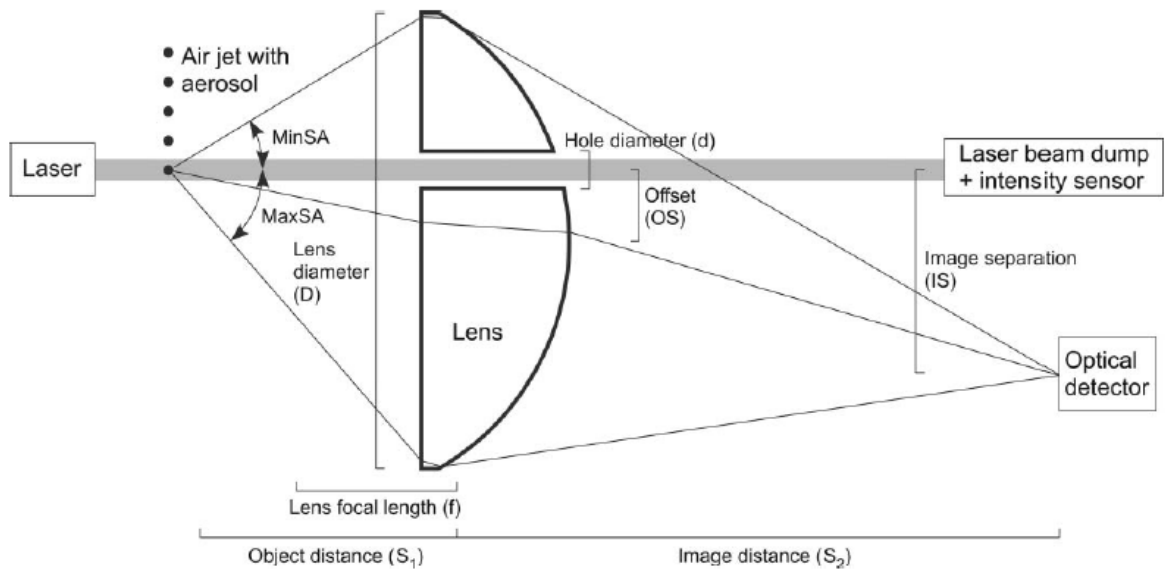


Figure 2.9 Schematic of a low cost particulate matter counter [8].

In this design, the forward scattered light pulses are focused using a lens, since the forward scattered light is of higher intensity. A laser beam crosses an imaging lens parallel to its optical axis via a hole drilled through the lens. The hole is offset from the lens optical axis. A particle-containing air jet intersects with the laser beam outside the lens focal plane. The forward scattered light pulses, by a particle were imaged to a point that is offset from the laser beam. An optical detector is used to measure the scattered light at the image spot. The optical detector signal can be related to the particle size if the refractive index is known. The

advantage of this scheme is that the forward scattered light is collected which helps improve the signal to noise ratio [8]. The drill hole feature isolates the scattered light pulses from the main beam. A drawback arises from the Gaussian nature of the beam. Since the intensity of the beam decreases exponentially radially, big particles traversing through the edge of the beam and small particles traversing through the centre of the beam will have comparable scattered intensities, which makes the detection process difficult and inaccurate to an extent.

2.1. Commercial sensors:

In this section, some of the popular commercial sensors available in the market will be discussed and compared [9-12]. The following lists out the main features of such sensors:

RTI MicroPEM™



Figure 2.10 The RTI MPEM device [9].

- Suitable for scientific work. With an accelerometer to help determine respiratory rate if worn on the body, to calculate exposure dose.

- Detection based on light scattering.
- Humidity and temperature measurement.
- No on screen display.
- Weight – 240 grams approx.
- Power - >36 hours on 3 AA Batteries.
- About \$2000.

Dylos Air Quality Monitor



Figure 2.11 Dylos sensor[10].

- On Screen display
- Real time monitoring of particle s of 0.5 micron and 2.5 micron size
- Weight – 2.5 lb.
- Dimensions – 177.8 x 114.3 x 76.2 mm

- Power – 4.5 W (adapter from wall)
- Detection based on light scattering.

Sharp GP2Y1010AU0F Optical Dust Sensor



Figure 2.12 Sharp GP2Y1010AU0F Optical Dust Sensor [11].

- Extremely cheap - \$11
- Needs interfacing with external microcontroller and display.
- Power – 140 mW
- Dimensions - $46.0 \times 30.0 \times 17.6$ mm
- Sensitivity - $0.5V/0.1mg/m^3$
- Detection based on light scattering.

Shinyei Model PPD42NS Dust Sensor



Figure 2.13 Shinyei PPD42NS Dust Sensor [12].

- Extremely cheap \$15
- Needs interfacing with external microcontroller and display.
- Power – 472.5 mW
- Dimensions - $59 \times 45 \times 22$ mm
- Minimum particle size > 1 μm
- Weight – 25 grams
- Detection based on light scattering.

2.1.1. Dylos sensor test:

In section the performance of the RTI MPEM and Dylos sensor is compared over a 2 hour period of cooking. The Dylos sensor reads out absolute particulate matter count/0.01 cubic feet. It is divided into two size bins, 'small' and 'big'. The 'small' category represents 1 μ m-5 μ m particles, whereas the 'big' category represents particle counts above 5 μ m. The RTI sensor reads out data in mass/volume (μ g/m³) and also takes into consideration, the ambient relative humidity to process this. To compare data from the two devices, the data from the Dylos sensor, i.e. absolute counts is converted to mass/volume units. This conversion is based on some strong assumptions [13], which is subject to further calibration and testing.

- All particles are spherical, with a density of 1.65E12 μ g/m³ [14].
- The radius of a PM2.5 particle is 0.44 μ m [15].
- The radius of a particle PM10 is 2.6 μ m [15].
- 0.01 cubic feet can be converted to m³ by multiplying by 3531.5.

With the knowledge of the particulate matter radius, it is possible to derive the volume and multiply by the particle density. This results in the following approximations of mass for each particle type:

- The mass of a particle in the PM2.5 channel is 5.89E-7 μ g
- The mass of a particle in the PM10 channel is 1.21E-4 μ g

The following equation [13] can be used to convert the number particles per 0.01 cubic feet to the number of micrograms per cubic meter and the results can be directly compared with other EPA data:

$$PM \text{ Concentration } (\mu\text{g}/\text{m}^3) = \text{Number of Particles} \times 3531.5 \times \text{Particle Mass} \quad (2.1)$$

It is important to consider the effect of humidity in the particulate matter concentration. With increased humidity levels, there might be some absorption leading to an increase in particulate mass. This can offset the readings to some amount if not corrected for. The RTI MPEM accounts for this but the Dylos sensor does not.

Figure 2.14 shows the absolute count data from the Dylos sensor over the two hour test period.

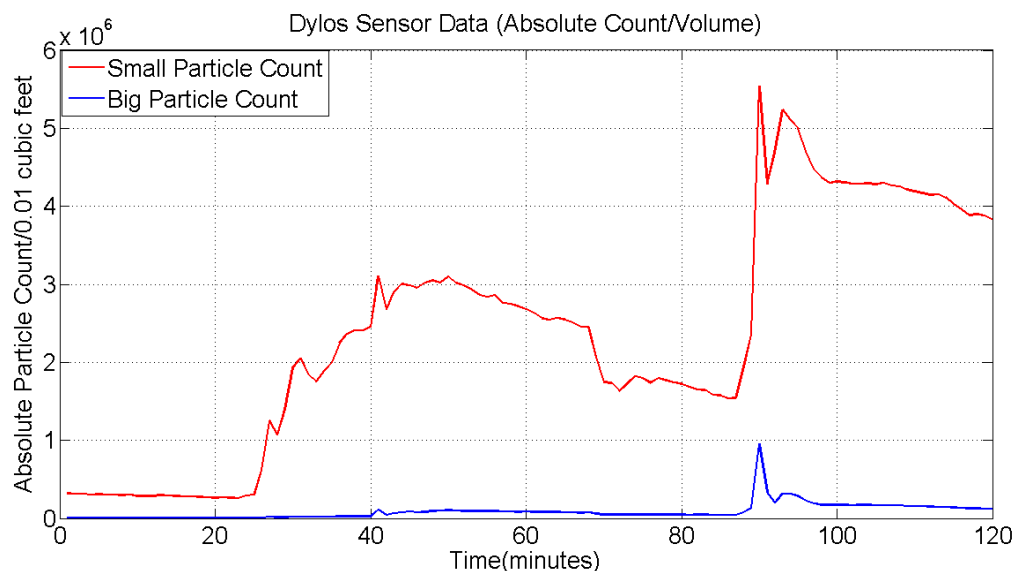


Figure 2.14 Dylos sensor data (Absolute counts)

As expected, the concentration of the smaller particles is larger than the larger particle size. Around the 90th minute during cooking, some spices were added, which led to a sudden spike in the particulate matter concentration. The Dylos sensor was able to respond to the change implying its robustness.

Figure 2.15 shows the Dylos sensor data after conversion to mass/volume units.

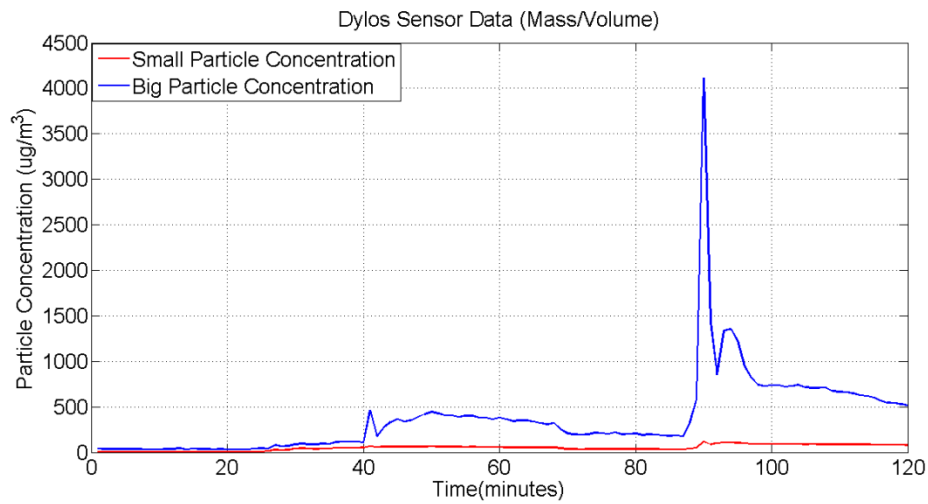


Figure 2.15 Dylos sensor data (mass/volume)

REFERENCES

1. B. Maheu, G. Gouesbet, G. Grehan, "A concise presentation of the generalized Lorenz-Mie theory for arbitrary location of the scatterer in an arbitrary incident profile", *J. Optics (Paris)*, vol. 19, no 2, pp. 59-67, 1988.
2. Frederick R. Faxvog, "Detection of Airborne Particles Using Optical Extinction Measurements", *Applied Optics*, Vol. 13, No. 8, August 1974.
3. Michael Heim, BenjaminJ.Mullins, HeinzUmhauer, Gerhard Kasper, "Performance evaluation of three optical particle counters with an efficient "multimodal" calibration method". *Aerosol Science*, Vol. 39, 1019–1031, 2008.
4. Burton G. Schuster and Robert Knollenberg, "Detection and Sizing of Small Particles in an Open Cavity Gas Laser", *Applied Optics*, Vol. 11, No. 7, July 1972.
5. Hirleman et. al, "Multiple Ratio Single Particle Counter", US Patent # 188121.
6. Susanne V. Hering , Mark R. Stolzenburg , Frederick R. Quant , Derek R. Oberreit & Patricia B. Keady, "A Laminar-Flow, Water-Based Condensation Particle Counter (WCPC)", *Aerosol Science and Technology*, 39:7, 659-672, 2005.
7. Oliver Ryan , Russell Greaney, S.Gerard Jennings, Colin D. O'Dowd, "Description of a biofluorescence optical particle counter", *Journal of Quantitative Spectroscopy & Radiative Transfer* 110 (2009) 1750–1754.

8. R. S. Gao , A. E. Perring , T. D. Thornberry , A. W. Rollins , J. P. Schwarz , S. J. Ciciora & D. W. Fahey, “A High-Sensitivity Low-Cost Optical Particle Counter Design”, *Aerosol Science and Technology*, 47:2, 137-145, 2013.
9. http://www.rti.org/page.cfm/Aerosol_Sensors
10. <http://www.dylosproducts.com/ornodcproair.html>
11. https://www.sparkfun.com/datasheets/Sensors/gp2y1010au_e.pdf
12. <http://www.sca-shinyei.com/pdf/PPD42NS.pdf>
13. http://wireless.ece.drexel.edu/air_quality/project%20files/Data%20Validation.pdf
14. Tittarelli, T. et al., “Estimation of particle mass concentration in ambient air using a particle counter,” *Atmospheric Environment*, vol. 42, pp. 8543-8548, 2008.
15. Lee, J. et al., “Seasonal variations of particle size distributions of PAHs at Seoul, South Korea,” *Air Quality Atmospheric Health*, vol. 1, pp. 57-68, 2008.

Chapter 3 Light Scattering Theory

3.1. Introduction

The following theory of light scattering essentially follows from [1] - [4]. The relevant aspects are discussed in the following sections.

Light scattering can be visualized as redirection of light when an electromagnetic (EM) wave interacts with an obstacle of non-homogeneity (in our case, particulate matter). Upon interaction, the electron orbits within the particles' constituent molecules are perturbed periodically with the same frequency as the electric field of the incident wave. This perturbation results in a periodic separation of charge inside the molecule, which results in an induced dipole moment. This oscillating dipole moment acts as a source of EM radiation, which results in scattered light. Most of the light scattered, is of the same frequency as the incident light, called elastic scattering. This phenomenon is a result of a complex interaction between the incident EM wave and the atomic/molecular structure of the scattering particle, and not a case of incident EM waves bouncing off the surface of the particles. This is shown in Figure 3.1 [3].

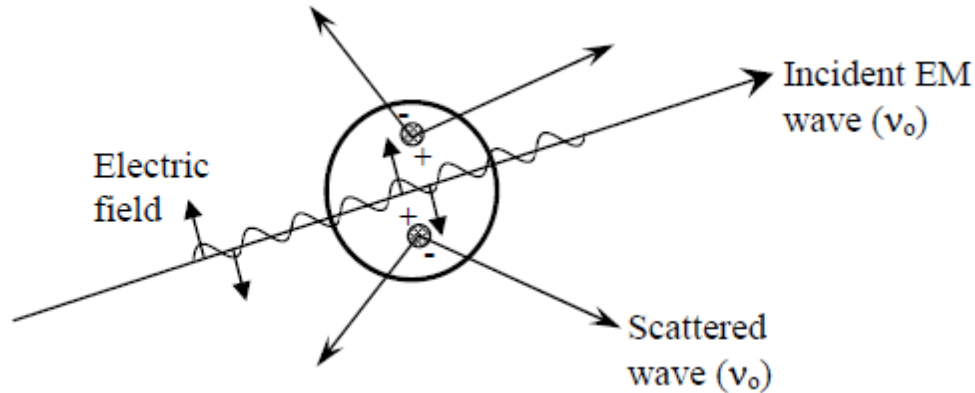


Figure 3.1 Light scattering by an induced dipole moment due to an incident EM wave [3].

Light scattering theory is usually explained by two theoretical frameworks: Rayleigh scattering and Mie scattering. Rayleigh scattering, strictly speaking is valid for small, dielectric (non-absorbing), spherical particles. Mie theory is applicable for general spherical scattering solution (absorbing or non-absorbing) without a particular bound on particle size. Mie scattering theory has no size limitations and converges to the limit of geometric optics for large particles. So, Mie theory can be used for describing most spherical particle scattering systems, including Rayleigh scattering.

Rayleigh scattering is preferred, due to the complexity of the Mie scattering formulation. The criteria for Rayleigh scattering are that $\alpha \ll 1$ and $|m|\alpha \ll 1$, where α is the dimensionless size parameter given by [3]:

$$\alpha = \frac{2\pi a}{\lambda} \quad (3.1)$$

where, a is the particle radius and λ is the relative scattering wavelength [3]:

$$\lambda = \frac{\lambda_o}{m_o} \quad (3.2)$$

and λ_o is the incident wavelength with respect to vacuum, and m_o is the refractive index of the surrounding medium. The refractive index of the scattering particle is given by m , represented by:

$$m = n - ik \quad (3.3)$$

where n is the refractive index of the sphere (i.e. n equals the speed of light in vacuum divided by the speed of light in the material), while the complex term is related to absorption. The commonly used absorption coefficient of the material (cm^{-1}) is related to the complex part of the refractive index via the relation [3]:

$$\text{Absorption Coefficient} = \frac{4\pi\kappa}{\lambda} \quad (3.4)$$

It should be noted that the value of k is never exactly zero for any material, but materials with a value approaching zero are termed dielectrics. The magnitude of the refractive index, m , as needed for the Rayleigh criteria, is given by the expression [3]:

$$|m| = \sqrt{(n^2 + \kappa^2)} \quad (3.5)$$

The Rayleigh criteria are valid when, $\alpha \ll 1$ and $|m|\alpha \ll 1$. This means that the particle is sufficiently small such that the particle encounters a uniform electric field at any moment, accordingly the time for penetration of the electric field is much less than the period of oscillation of the EM wave. However, in our case, the wavelength is in the nanometer range and the particle size in micron range, the Rayleigh criteria is not valid. The spherical

coordinate scattering geometry used for Mie and Rayleigh light scattering corresponding to a single incident light ray on a single spherical particle can be illustrated using Figure 3.2 [3].

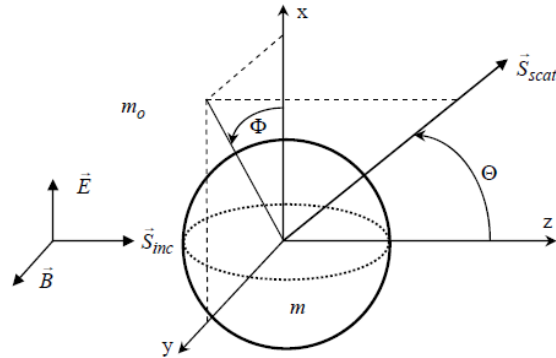


Figure 3.2 Coordinate geometry for Rayleigh and Mie scattering [3].

For each scattering angle (ϕ, θ) , the intensities (W/cm^2) of the scattered radiation, vertically and horizontally polarized with respect to the scattering plane, respectively, defined by the incident ray (of intensity I_0) and the scattered ray are defined by [3]:

$$I_{\phi} = I_0 \frac{\lambda^2}{4\pi^2 r^2} i_1 \sin^2 \phi \quad (3.6)$$

$$I_{\theta} = I_0 \frac{\lambda^2}{4\pi^2 r^2} i_2 \cos^2 \phi \quad (3.7)$$

The incident radiation produces similarly polarized scattered radiation if the particles are perfectly spherical. So, the scattering problem can be redefined in terms of the polarization states with respect to each other. Accordingly, equations 6 and 7 can be redefined in the following way [3]:

$$I_{VV} = I_0 \frac{1}{r^2} \sigma_{VV} \quad (3.8)$$

$$I_{HH} = I_o \frac{1}{r^2} \sigma_{HH} \quad (3.9)$$

In the equations above, the subscripts refer to the states of incident and scattered light respectively, with respect to the scattering plane. The subscripts, VV refer to both vertically polarized incident light and vertically polarized scattered light with respect to the scattering plane (i.e. $\phi = 90^\circ$). Similarly, the subscripts HH refer to both horizontally polarized incident light and horizontally polarized scattered light with respect to the scattering plane (i.e. $\phi = 0^\circ$). For unpolarized light, the scattering equation can be written as [3]:

$$I_{scat} = I_o \frac{1}{r^2} \sigma_{scat} \quad (3.10)$$

where σ_{scat} is the average of σ_{HH} and σ_{VV} . There is no dependence on ϕ . It is noted that the dependency of the above quantities on the scattering angle θ is through the differential cross sections [3], as detailed below. Equations 8-10 provide an expression for the *intensity* of light about a single scattered ray. These equations may also be reconsidered in terms of the rate of scattered *energy* into a defined solid angle, as shown in Figure 3.5 [3].

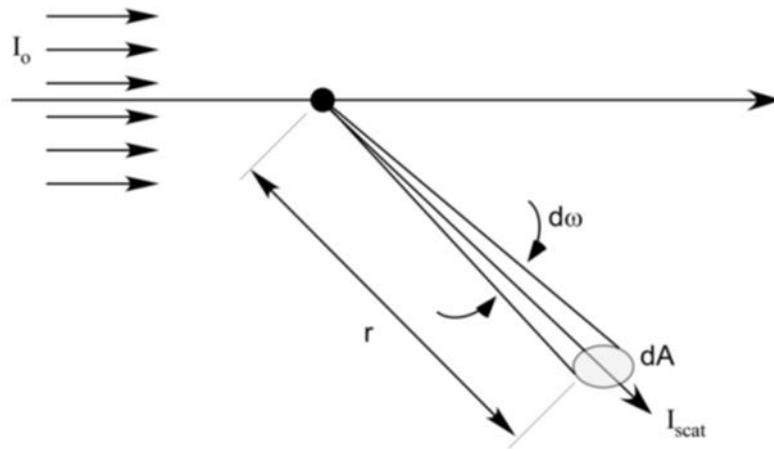


Figure 3.3 Angular scattering intensity[3].

Using the differential scattering cross section, the total scattered energy rate (W) striking dA is given by [3]:

$$E_{scat} = I_o \sigma_{scat} d\omega \quad (3.11)$$

where the solid angle $d\omega$ is related to the subtended area by $d\omega = dA/r^2$. Substitution of dA/r^2 for the solid angle and division of both sides by dA yields equation 3.10; hence the scattered intensity about the scattered ray I_{scat} .

The equations described above only account for the redistribution of incident radiation due to light scattering. However, the incident radiation may also be *absorbed* by the particle. The rate of the total amount of incident energy abstracted from the incident beam due to interactions with a single particle is calculated directly from the extinction cross section (cm^2). This is given by [3]:

$$E_{removed} = I_o \sigma_{ext} \quad (3.12)$$

The extinction cross section represents the loss of energy from the incident beam due to both scattering and absorption. The maximum cross section can then be expressed as [3]:

$$\sigma_{ext} = \sigma_{abs} + \sigma_{scat} \quad (3.13)$$

where σ_{abs} and σ_{scat} are the absorption and total scattering cross sections (cm^2) respectively. The latter quantity is calculated by integrating the differential cross section over 4π steradians. While the above equations allow calculation of the relevant scattering and extinction quantities based on the incident light intensity, the Rayleigh and Mie theories are

required to provide the appropriate expressions for calculation of the various cross-sections expressed above.

3.2. Rayleigh Theory

In the Rayleigh regime, the differential scattering cross sections are readily calculated from the following equations [3]:

$$\sigma_{VV} = \frac{\lambda^2}{4\pi^2} \alpha^6 \left| \frac{m^2 - 1}{m^2 + 2} \right|^2 \quad (3.14)$$

$$\sigma_{HH} = \sigma_{VV} \cos^2 \theta \quad (3.15)$$

These equations reveal several interesting phenomena. The differential scattering cross sections are proportional to the 6th power of particle size, and are inversely proportional to the 4th power of wavelength. The latter dependency gives rise to the blue color of the sky, as the air molecules (e.g. N₂ and O₂) are within the Rayleigh regime; hence the shorter blue light of the sun is more efficiently redirected out of the direct path of sunlight and subsequently redirected from all directions as scattered light. It is also observed that the vertical-vertical differential scattering cross section is independent of the observation angle θ , while the horizontal-horizontal differential scattering cross section has a minimum at 90°. This implies that unpolarized light will be strongly polarized at 90° observation for Rayleigh particles [3]. The total scattering cross section (cm²) and absorption cross section (cm²) are defined as [3]:

$$\sigma_{scat} = \frac{2\lambda^2}{3\pi} \alpha^6 \left| \frac{m^2 - 1}{m^2 + 2} \right|^2 \quad (3.16)$$

$$\sigma_{abs} = \frac{-\lambda^2}{\pi} \alpha^3 \text{Im} \left| \frac{m^2 - 1}{m^2 + 2} \right|^2 \quad (3.17)$$

The total extinction cross section (cm^2) is defined as a sum of the scattering and absorption cross sections [3]:

$$\sigma_{ext} = \sigma_{abs} + \sigma_{scat} \quad (3.18)$$

As represented in equations (16) and (17), the scattering cross section is proportional to α^6 , while the absorption cross section is proportional to α^3 . In the Rayleigh regime, the size parameter must be much less than 1, therefore the contribution of scattering (i.e. σ_{scat}) to the total extinction cross section is generally neglected for an absorbing particle ($k \neq 0$), and it is therefore assumed that $\sigma_{ext} = \sigma_{abs}$ [3].

3.3. Mie Theory

According to Mie theory, the differential scattering cross sections can be defined in terms of the angular intensity functions i_1 and i_2 . This is given by [3]:

$$\sigma_{VV} = \frac{\lambda^2}{4\pi^2} i_1 \quad (3.19)$$

$$\sigma_{HH} = \frac{\lambda^2}{4\pi^2} i_2 \quad (3.20)$$

The two equations are averaged to define the differential scattering cross section for unpolarized incident light [3]:

$$\sigma_{scat} = \frac{\lambda^2}{8\pi^2} (i_1 + i_2) \quad (3.21)$$

The intensity functions are calculated from the infinite series given by [2]:

$$i_1 = \left| \sum_{n=1}^{\infty} \frac{2n+1}{n(n+1)} [a_n \pi_n(\cos \theta) + b_n \tau_n(\cos \theta)] \right|^2 \quad (3.22)$$

$$i_2 = \left| \sum_{n=1}^{\infty} \frac{2n+1}{n(n+1)} [a_n \pi_n(\cos \theta) + b_n \tau_n(\cos \theta)] \right|^2 \quad (3.23)$$

In equations 22 and 23, the angular dependent functions, π_n and τ_n are expressed in terms of the Legendre polynomials by [2]:

$$\pi_n(\cos \theta) = \frac{P_n^{(1)}(\cos \theta)}{\sin \theta} \quad (3.24)$$

$$\tau_n(\cos \theta) = \frac{dP_n^{(1)}}{d\theta}(\cos \theta) \quad (3.25)$$

where the parameters a_n and b_n are defined as [2]:

$$a_n = \frac{\Psi_n(\alpha)\Psi'_n(m\alpha) - m\Psi_n(m\alpha)\Psi'_n(\alpha)}{\xi(\alpha)\Psi'_n(m\alpha) - m\Psi_n(m\alpha)\xi'_n(\alpha)} \quad (3.26)$$

$$b_n = \frac{m\Psi_n(\alpha)\Psi'_n(m\alpha) - \Psi_n(m\alpha)\Psi'_n(\alpha)}{m\xi(\alpha)\Psi'_n(m\alpha) - m\Psi_n(m\alpha)\xi'_n(\alpha)} \quad (3.27)$$

The size parameter is defined by [2]:

$$\alpha = \frac{2\pi a m_o}{\lambda_o} \quad (3.28)$$

Ψ and ξ are the Ricatti – Bessel functions which are defined in terms of the half – integer order Bessel function of the first kind $(J_{n+1/2}(z))$, where [2]:

$$\Psi_n(z) = \left(\frac{\pi z}{2}\right)^{\frac{1}{2}} H_{n+1/2}(z) = \Psi_n(z) + iX_n(z) \quad (3.29)$$

where, $H_{n+1/2}(z)$ is the half-integer-order Hankel function of the second kind, where the parameter X_n is defined in terms of the half-integer-order Bessel function of the second kind, $Y_{n+1/2}(z)$, as [2]:

$$X_n(z) = -\left(\frac{\pi z}{2}\right)^{\frac{1}{2}} Y_{n+1/2}(z) \quad (3.30)$$

Finally, the total scattering and extinction cross sections can be expressed as [2]:

$$\sigma_{scat} = \frac{\lambda^2}{2\pi} \sum_{n=0}^{\infty} (2n + 1) \text{Re}\{a_n + b_n\} \quad (3.31)$$

$$\sigma_{ext} = \frac{\lambda^2}{2\pi} \sum_{n=0}^{\infty} (2n + 1) \text{Re}(|a_n|^2 + |b_n|^2) \quad (3.32)$$

It is noted that the absorption cross section, σ_{abs} can be readily calculated knowing the above two using Equation 13.

3.4. Light Scattering Behavior

The plots below highlight some of the important characteristics in Mie and Rayleigh scattering for spherical particles for a range of conditions, including angular dependency and size dependency.

Figure 3.6 [3] shows the dependence of the differential scattering cross-section (σ_{scat}) as a function of scattering angle (θ) for particle sizes of 1.7 μm , 170 nm and 17 nm respectively, with refractive index, $m = 1.4 - 0i$, when incident upon light of wavelength, $\lambda = 532 \text{ nm}$.

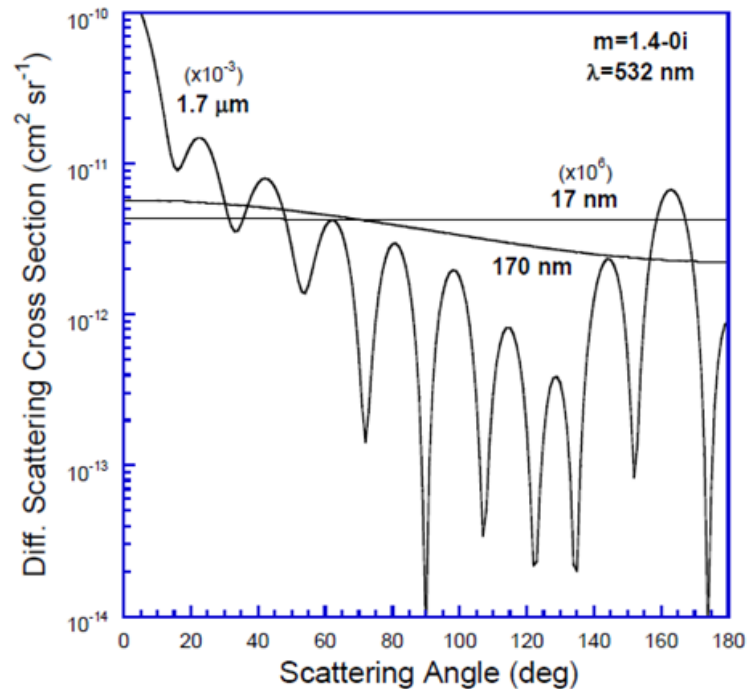


Figure 3.4 Dependence of scattering cross-section vs scattering angle [3].

Figure 3.6 [3] presents the differential scattering cross-section (σ_{scat}) as a function of scattering angle (θ). 0° is forward scattering and 180° is backscattering. The smallest particle size of 17 nm ($\alpha = 0.1$) is inside the Rayleigh regime, so the angular dependence is negligible. The 170 nm particle ($\alpha = 1.0$) is beyond the Rayleigh regime, and therefore displays some angular variation, with forward scattering beginning to show up. The 1.7 nm particle ($\alpha = 10$) is clearly in the Mie regime, where forward scattering dominates. The

“ripple” behaviour as a function of scattering angle is characteristic of Mie scattering, and is due to the complex interactions of scattered and refracted rays that result in constructive and destructive interference along different paths (i.e. different scattering angles). Note the scale factors in parentheses for the 17 nm and 1.7 nm particle plots, hence these cross-sections vary by more than 10 orders of magnitude for the two-order of magnitude variation in particle size. The plots are in semi-log to show the effects due to varying particle size.

Figure 3.7 [3] shows the extinction efficiency as a function of parameter.

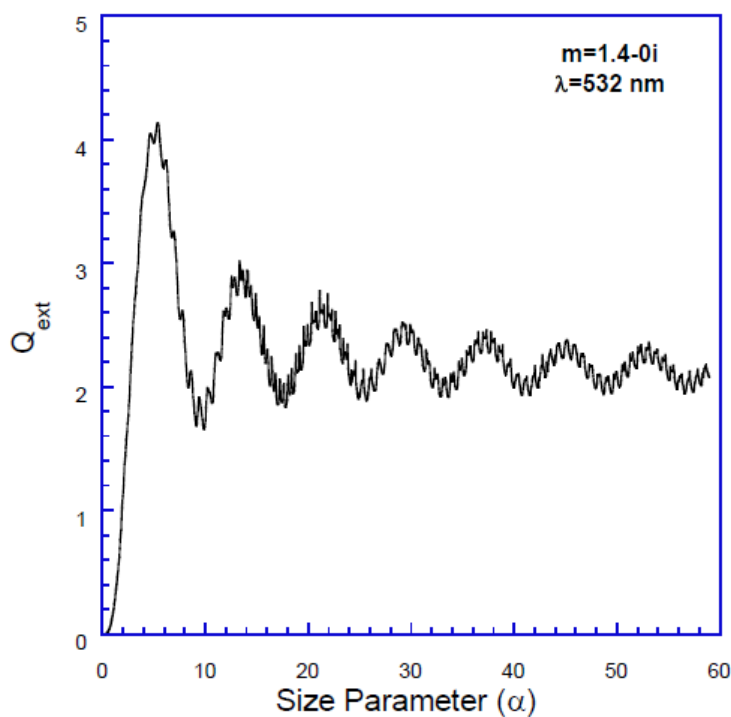


Figure 3.5 Extinction efficiency vs size parameter [3].

The extinction efficiency is the extinction cross section (σ_{ext}) normalized by the geometric cross section (πa^2). For Rayleigh sized particles, the extinction efficiency is much less than 1. For particles in the Mie regime, two characteristics are noted. The ripple or resonance structure observed in the angular scattering plot is also present with extinction, although not as pronounced. In addition, the asymptotic limit of the above plot is 2, which means that in the large particle limit, twice as much energy is removed as expected based on the geometric cross section. This is contrary to observation, and is referred to as the extinction paradox. In reality, one half of the energy is removed by scattering/extinction, while the second half is removed via near-forward angle diffraction. Since the observer generally “sees” the diffracted energy, it appears that a large particle only removes energy equal to its actual geometric cross-section.

Figure 3.8 [3] shows the differential scattering cross-section at a fixed angle of 15° , for various sizes of a particle with different refractive indices at an incident wavelength, $\lambda = 532 \text{ nm}$.

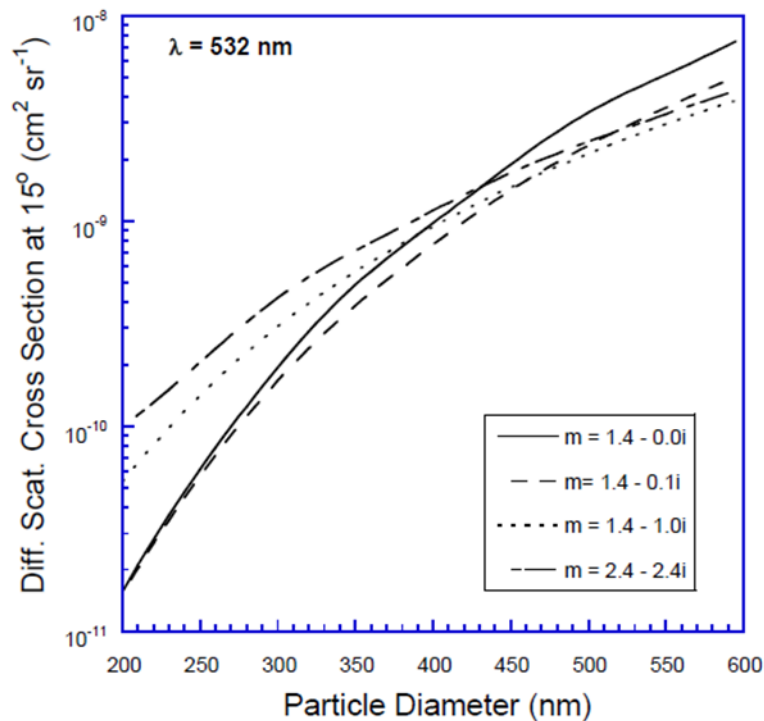


Figure 3.6 Differential scattering cross-section vs Particle diameter [3.]

Figure 3.8 [3] presents the differential scattering cross section (σ_{scat}) at a fixed angle of 15° as a function of scattering particle diameter for various particle refractive indices. Data are presented for a dielectric, as well as increasingly absorptive particles, and finally for a particle with enhanced refraction and absorption. The main point illustrated from these plots is the complex nature of the dependency of Mie scattering on refractive index. It is very difficult to make prior assumptions about the relative magnitude of scattering for a given particle size and scattering angle with regard to the value of refractive index m .

REFERENCES

1. H.C. van de Hulst, "*Light scattering by small particles*", John Wiley & Sons, New York, 1957.
2. C.F. Bohren and D.R. Huffman, "*Absorption and scattering of light by small particles*", John Wiley & Sons, New York, 1983.
3. David W. Hahn, "*Light Scattering Theory*", Department of Mechanical and Aerospace Engineering, University of Florida, July 2009.
4. M. Kerker, "*The scattering of light and other electromagnetic radiation*", Academic, New York, 1969.

Chapter 4 System Level Design

For any multi-disciplinary project, especially sensors, the performance is dependent on a multitude of factors, imposing complex trade-offs which puts a lot of emphasis on system level optimization of the sensor. In this chapter, the system level design aspects of the sensor will be discussed at various levels.

The system level design can be broadly classified into the following levels:

- Optics
- Circuit design
- Embedded systems/interfacing
- CAD/prototyping

Each level will be discussed and various trade-offs and design methodology will be covered in the following sections. A system level block diagram can be represented by Figure 4.1.

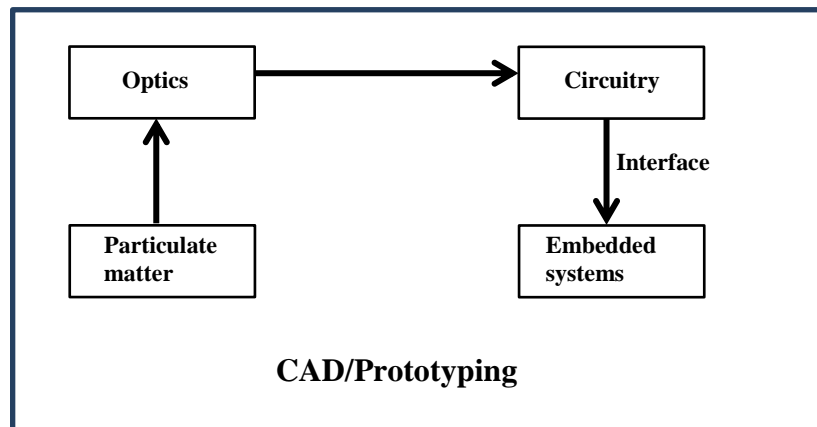


Figure 4.1 System level block diagram.

The particulate matter introduced in the system is collected by the reflective optics, which is then focused onto the photodiode, interfaced with transimpedance amplifier circuit. This is then interfaced with the embedded systems block, which deal with analog to digital conversion and processing of signals. The processed data is then displayed on an LCD. Finally, the 3D printed CAD design encloses everything.

4.1. Optics

Optics provides the foundation around which the rest of the sensor is built. This is the most important aspect in the entire design. As explained in Chapters 1 and 3, Mie scattering phenomenon is leveraged to detect particulate matter. The intensity vs scattering angle plot gives details about the intensity distribution of the scattered light pulses as a function of angle for a given refractive index and size of the particle. Figure 4.2 - 4.4 show the scattered intensity distributions as a function of angle for particles of diameters 2.5 μm , 5 μm and 10 μm respectively with a refractive index of 1.33 (water).

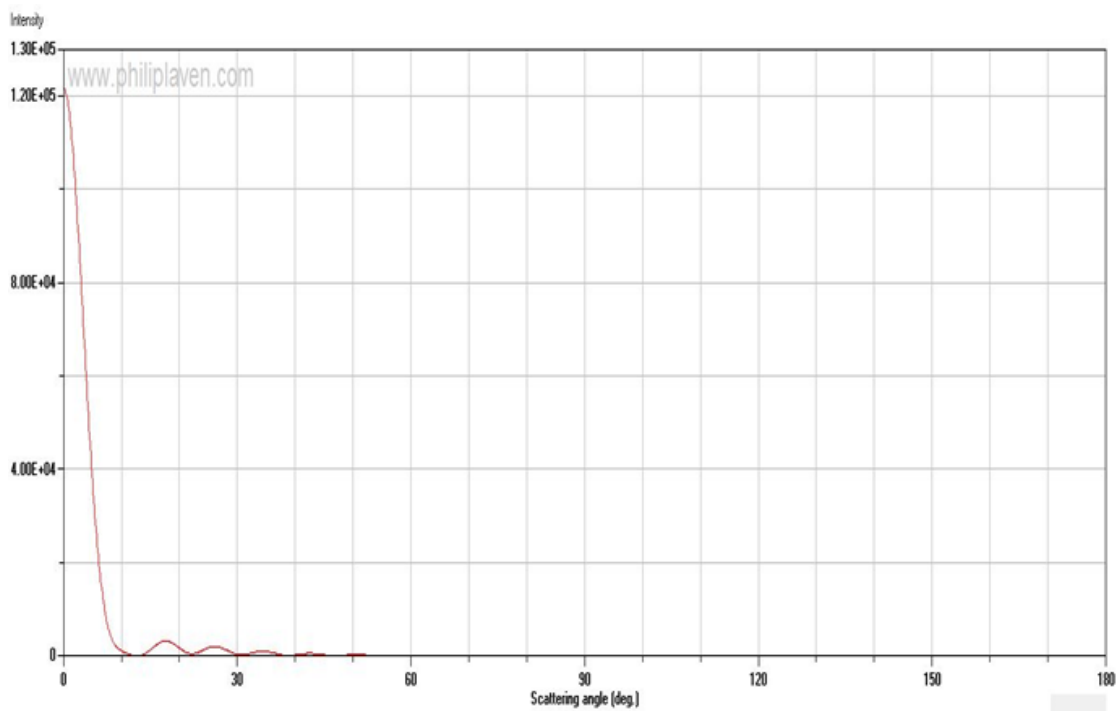


Figure 4.2 Intensity distribution of scattered light for 2.5 μm particle with $n = 1.33$.

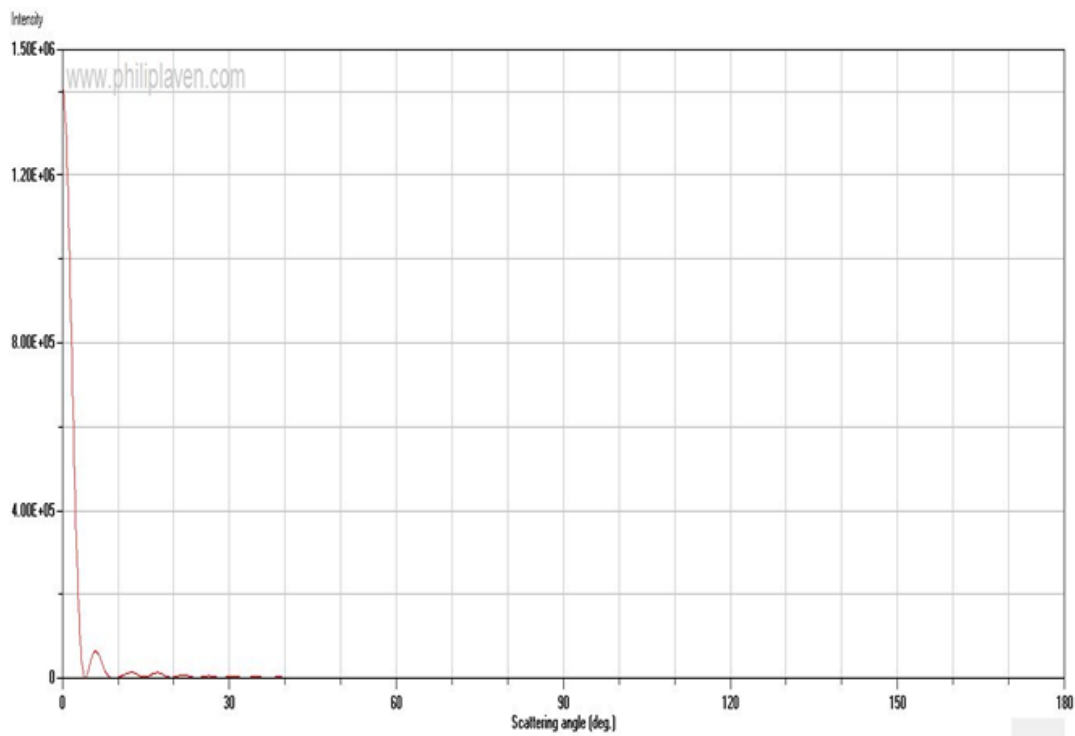


Figure 4.3 Intensity distribution of scattered light for 5 μm particle with $n = 1.33$.

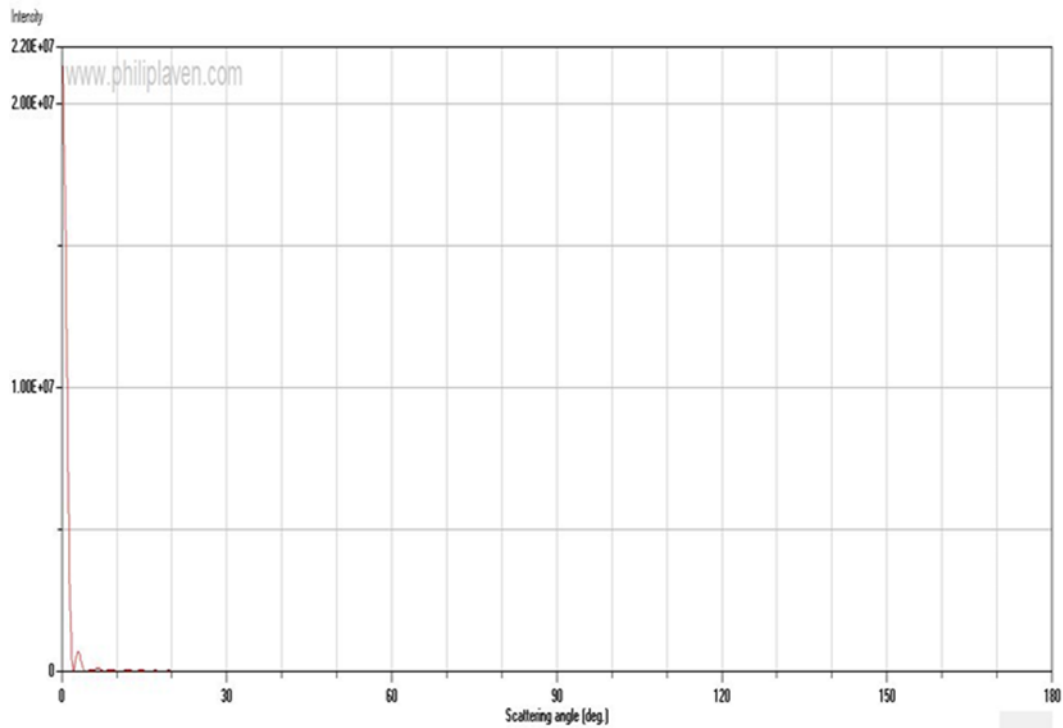
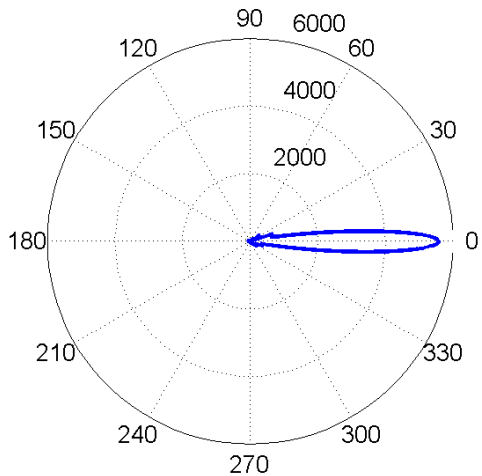


Figure 4.4 Intensity distribution of scattered light for 10 μm particle with $n = 1.33$.

From the plots, it can be seen that the intensity of the forward scattered light with $\pm 5^\circ$ is orders of magnitude higher than the higher angles and it falls off faster for larger sized particles. This can also be seen the following polar plots which show the angular distribution of the scattered intensity for water drops with a refractive index of 1.33 of sizes 2.5 μm , 5 μm and 10 μm respectively. These are shown by Figures 4.5 – 4.7.

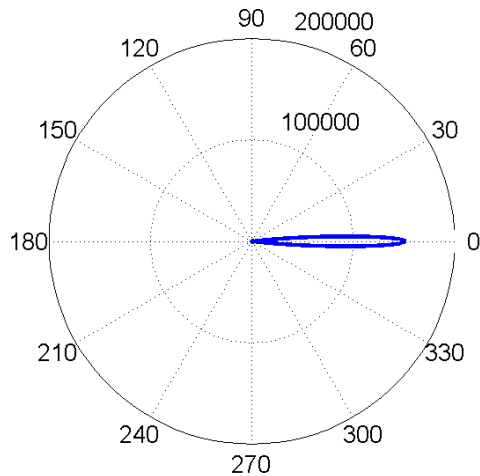
Mie angular scattering: $m=1.33+0i$, $x=12.42$



Scattering Angle

Figure 4.5 Angular distribution of scattered intensity for 2.5 μm water drop.

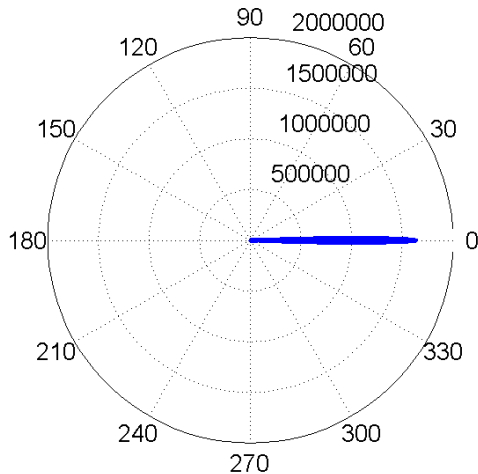
Mie angular scattering: $m=1.33+0i$, $x=24.854$



Scattering Angle

Figure 4.6 Angular distribution of scattered intensity for 5 μm water drop.

Mie angular scattering: $m=1.33+0i$, $x=49.708$



Scattering Angle

Figure 4.7 Angular distribution of scattered intensity for 5 μm water drop.

This can be leveraged via an optical design which focuses the forward scattered light at such small angles onto a photodetector. This inherent *optical gain* boosts the signal to noise ratio and enables the use of low cost photodiodes and minimal circuitry. A reflective optical design is proposed in order to realize this. The design is built around a Thorlabs off-axis parabolic mirror (MPD127127-90-G01). Figures 4.8 [1] and 4.9 [1] show the schematic diagram and key specifications of this mirror.

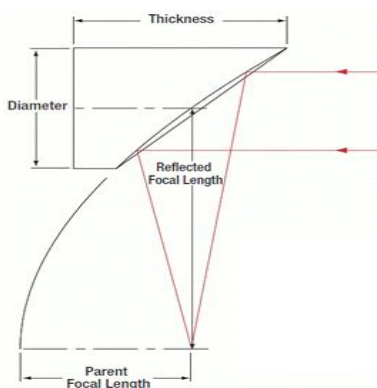


Figure 4.8 Schematic of the parabolic mirror [1].

Item #	MPD127127-90-G01
Diameter ^a	1/2" (12.7 mm)
Reflected Focal Length (RFL) ^a	1" (25.4 mm)
Parent Focal Length ^a	1/2" (12.7 mm)
Thickness ^a	0.74" (18.8 mm)
Off-Axis Angle	90°

Figure 4.9 Key specifications of the parabolic mirror [1].

Using this mirror, a $2f$ - $2f$ (f is the focal length of the mirror) reflective design is proposed as shown in Figure 4.10.

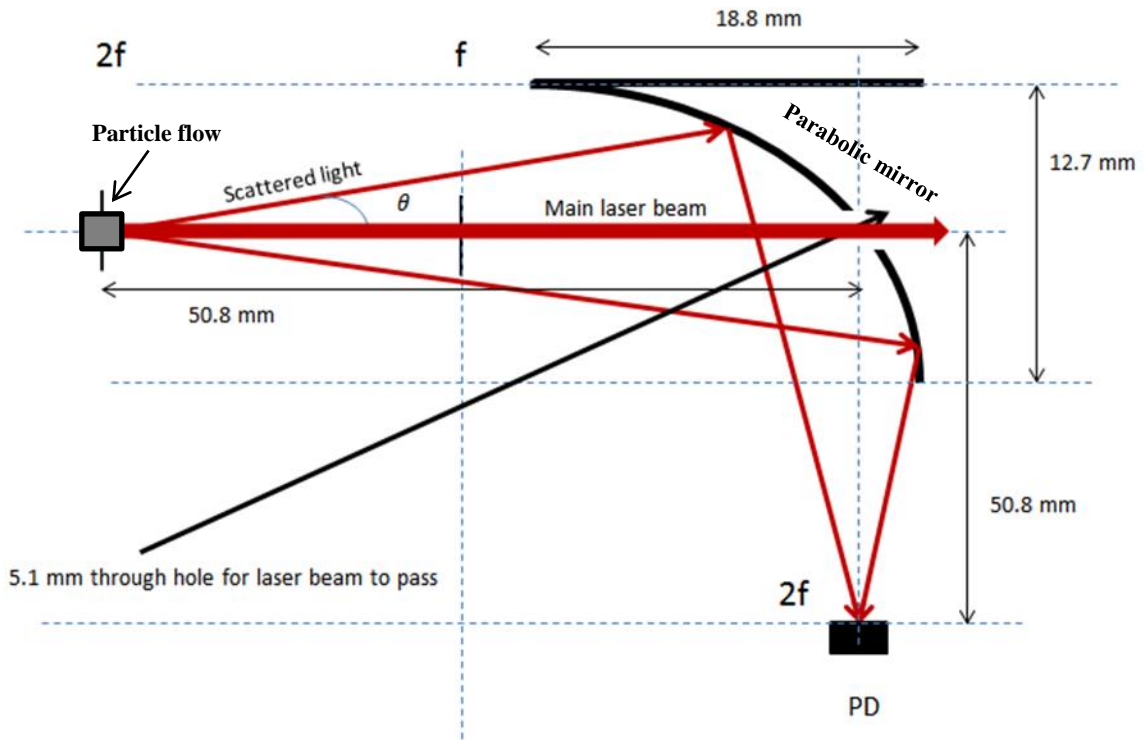


Figure 4.10 Optical design of the sensor.

In this design, the scattering takes place just after the laser diode aperture, which is at a distance $2f$ away from the mirror. The scattered light, after getting reflected from the surface of the mirror, was focused on to a photodetector, at a distance $2f$ from the mirror. θ is the angle of scattered light, which was limited by the size of the through-hole and the aperture of the mirror which acts as a stop. Assuming that the scattering takes place at the center of the beam, the range of θ can be given by:

$$\theta_{max} = \tan^{-1} \left(\frac{\text{Mirror diameter}/2}{2 \times \text{Focal length}} \right) \quad (4.1)$$

$$\theta_{min} = \tan^{-1} \left(\frac{\text{Hole diameter}/2}{2 \times \text{Focal length}} \right) \quad (4.2)$$

where θ_{max} and θ_{min} are the maximum and minimum angles of scattered light which can be detected. With the mirror diameter, hole diameter and focal length being 12.7 mm, 5.1 mm and 25.4 mm, **θ ranges from 2.87° to 7.125°**. This covers the range of angles for high intensity forward scattered light pulses, which upon reflection, are focused to a photodiode. The laser diode used was an Infiniter VLM-650-03 module with an integrated driver circuit. The main reasons for using this laser diode were its compact size (7mm x 2mm), low cost (\$6), red emission wavelength (readily available photodiodes at this range) and relatively low power consumption (5mW output optical power at 5V DC supply and 30 mA current). Figure 4.11 shows a picture of the laser diode.



Figure 4.11 Laser diode [2].

The choice of the photodiode was driven by size restrictions, cost and aberrations introduced by the parabolic mirror. The major first order optical aberrations include ***spherical aberration, astigmatism and coma***, which are described in detail here [3].

These aberrations produce a spot size which is larger than ideal. This can be visually represented by Figures 4.12 and 4.13 [4].

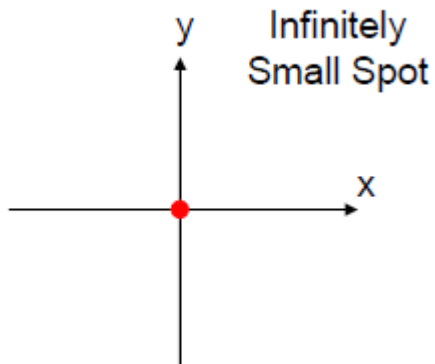


Figure 4.12 Spot size in ideal case [4].

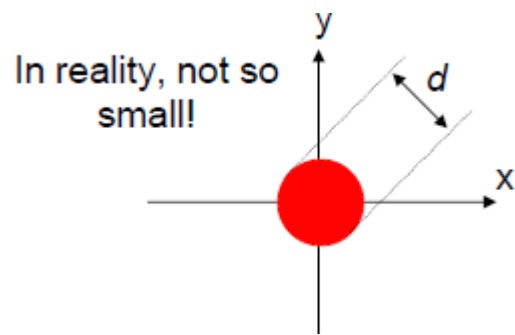


Figure 4.13 Spot size in reality [4].

In addition to this, a major limitation is *optical misalignment*, due to which the photodetector area needs to be sufficiently large to ensure that the scattered light pulses are reliably collected.

The photodiode used is a Thorlabs FDS1010. The main factors influencing the choice of the photodiode are size, ease of integration and cost. Figures 4.14 and 4.15 [5] show photodiode and its responsivity plot, respectively.



Figure 4.14. Thorlabs FDS1010 photodiode [5].

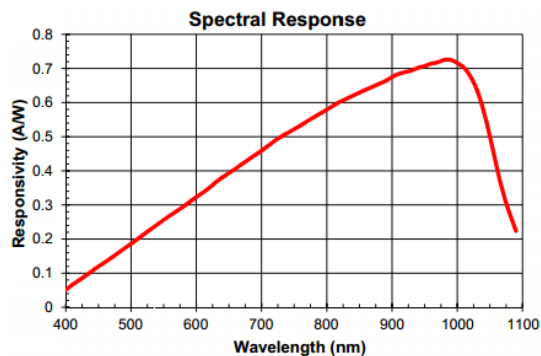


Figure 4.15. Responsivity of FDS1010 [5].

4.2. Circuit Design:

The circuit design section will discuss the considerations in the circuit design process and highlight trade-offs, which need to be kept in mind to maximize the sensor performance. A system level block diagram showing the various circuit blocks is shown in Figure 4.16.

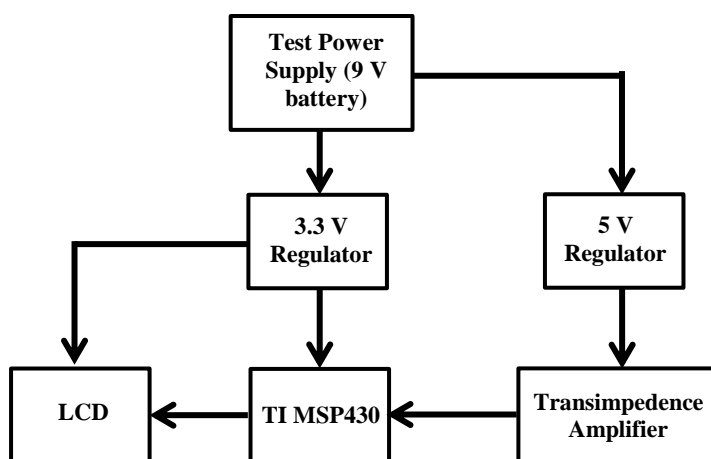


Figure 4.16 Circuit level block diagram.

A 9 V battery is used as a test power supply for experiments. The 3.3 V regulator fed power to the TI MSP430 microcontroller and LCD display modules. The 5 V regulator fed the Op-Amp used in the transimpedance circuit. The transimpedance amplifier boosted the electrical signal fed by the photodiode. These signals were then converted to digital form using the 10 bit SAR ADC module of the TI MSP430 microcontroller. The particle counting algorithm, implemented in the microcontroller generated the particle count which was then displayed by the LCD.

4.2.1. Transimpedance amplifier

A transimpedance circuit is used to convert an input current from a current source (typically a photodiode) into an output voltage. The analysis in this section closely follows [6] and [7]. The simplest method to achieve this conversion is to use a resistor connected to ground. However, the achievable gain using this method is limited by the following factors:

- Desired bandwidth
- Load Impedance
- Current source input impedance.

A closed-loop approach, using an operational amplifier, is beneficial to most applications as it has the potential of eliminating those issues. A typical circuit with all necessary components for this analysis is shown in Figure 4.17 [6].

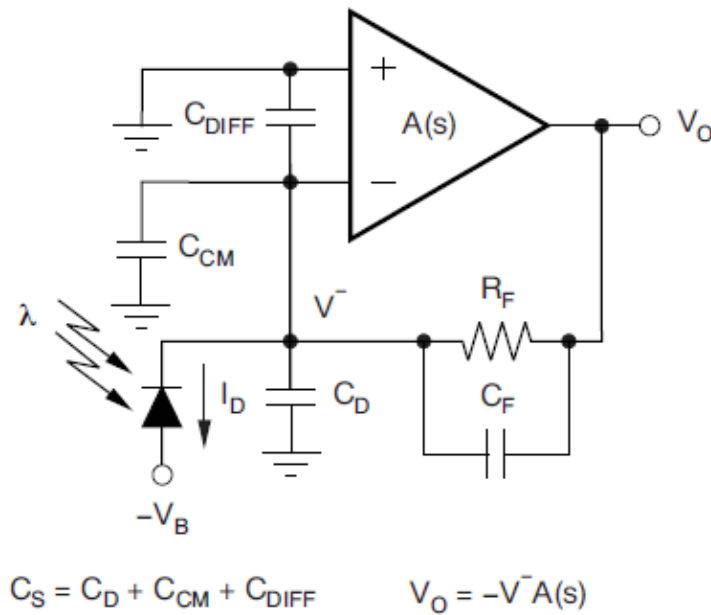


Figure 4.17 Transimpedance Circuit with Modeled Elements [6].

In this circuit, the photodiode converts photons into current. This current is then amplified by the feedback resistor R_F . For an ideal amplifier, the entire signal generated by the photodiode is going to be converted to the output because no bias current is present. The source impedance is not a concern here as it is isolated from the output. The output is low impedance, allowing a wide variety of load to be connected. The bandwidth is a function of the source capacitance (C_S), the feedback capacitance (C_F), and the gain bandwidth product (GBW) of the actual amplifier used. The source capacitance (C_S) is the sum of the photodiode capacitance (C_D), the common-mode capacitance of the amplifier (C_{CM}), and the differential capacitance of the amplifier (C_{DIFF}). C_{CM} and C_{DIFF} include both the board layout and the op amp parasitic capacitance [6].

The output voltage gain is set by the feedback resistor, given by [6]:

$$V_o = I_D R_F \quad (4.3)$$

where, V_o is the output voltage, I_D is the photodiode current, R_F is the feedback resistance. A feedback capacitor is also often needed control the frequency response of the circuit as at higher frequencies the signal increases with a gain of [6]:

$$Gain = 1 + \frac{Z_F}{Z_S} = 1 + \frac{2\pi f R_F C_S}{1 + 2\pi f R_F C_F} \quad (4.4)$$

where, Z_F is the impedance of the feedback part of the circuit, Z_S is the impedance of the input of the circuit, and f is the frequency. The value for the feedback capacitor needed to roll off this gain can be calculated from [6]:

$$C_F = \sqrt{\frac{C_S}{R_F \pi f_{GBW}}} \quad (4.5)$$

where $C_S = C_D + C_{CM} + C_{DIFF}$, with C_D being the photodiode capacitance, C_{CM} being the common mode input impedance of the op-amp, and C_{DIFF} the differential input impedance of the op-amp. The capacitance of the photodiode can be changed by altering the bias voltage applied to it, which also changes the dark current and bandwidth of the photodiode. The C_{CM} and C_{DIFF} are fundamental characteristics of the op-amp used. The feedback capacitance is usually very small and can sometimes be neglected due to the parasitic capacitance caused by the surface mount nature of the op-amp. The smallest value C_F is this parasitic capacitance. The bandwidth of the circuit is given by [6]:

$$f_{3dB} = \sqrt{\frac{f_{GBW}}{2\pi R_F C_F}} \quad (4.6)$$

In terms of the photodiode capacitance and feedback resistance, the bandwidth can also be expressed as [7]:

$$f_{BW} = \sqrt{\frac{f_{GBW}}{4\pi R_F C_D}} \quad (4.7)$$

With the roll-off (pole) of the high frequency gain set by [7]:

$$f_{pole} = \frac{1}{2\pi R_F C_F} \quad (4.8)$$

Next, some noise considerations will be discussed. The op-amp has two characteristic sources of noise, *input voltage noise*, e_n , and *input current noise*, i_n [6]. The other major source of noise in low noise circuits is *Johnson-Nyquist* noise which is a fundamental source of noise caused by thermal fluctuations of the charge carriers in all resistors in the circuit and is given by [6]:

$$e_{JN} = \sqrt{4k_B T R} \quad (4.9)$$

$$i_{JN} = \sqrt{\frac{4k_B T}{R}} \quad (4.10)$$

where k_B is the Boltzmann constant, T is the temperature, R is the resistance of the resistor. Dark current from the photodiode leads to a DC offset noise, which is unimportant in this case but also has a *shot noise* associated with it given by [6]:

$$i_{shot} = \sqrt{2q i_{dark} f_{BW}} \quad (4.11)$$

where, i_{shot} is the dark current shot noise, q is the charge on an electron, and i_{dark} is the dark current.

The input current noise of the op-amp is the lowest possible current noise in a circuit and is only reached in certain circumstances and the total current noise in a given transimpedance circuit is given by [6]:

$$i_{TOT} = \sqrt{i_N^2 + \frac{4kT}{R_F} + \left(\frac{e_N}{R_F}\right)^2 + \frac{(e_N 2\pi C_S B)^2}{3} + i_{shot}^2} \quad (4.12)$$

where, i_{TOT} is the total input current noise of the circuit. This equation is only correct when the bandwidth of the noise/circuit is less than the frequency given in Equation 4.7. The 1st term in this equation comes from the op-amp input current noise, the 2nd term comes from the Johnson noise on the feedback resistor, the 3rd term comes from the op-amp input voltage noise converted to current via the feedback resistor, the 4th term comes from the voltage noise being converted to current via the input impedance of the circuit which changes with frequency and that is why the relevant bandwidth (B) is important and the last term comes from the shot noise of the dark current of the photodiode [6]. To get the total output voltage noise the total input current noise should be multiplied by feedback resistor:

$$V_{noise} = i_{TOT} R_F \quad (4.13)$$

4.2.2. Bandwidth and SNR calculations

Next, the bandwidth requirement of the circuit will be calculated and will be related to the detectable size ranges of particles.

The *lower limit of the bandwidth requirement* is set by the *flow rate* and *particulate matter concentration*. Let P be the flow rate in lpm (liters per minute). This can be represented in the units of cm^3/s by:

$$P = \frac{100P}{6} \quad (4.14)$$

Let the particulate matter concentration be Q #particles/cm³. Then the bandwidth (BW) set by these two factors can be given by:

$$BW = \frac{100PQ}{6} \text{ Hz} \quad (4.15)$$

Considering a modest flow rate of 1 lpm and a particulate matter concentration of 10000 #particles/cm³, the BW required comes out to be ~167 kHz.

From the knowledge of Mie theory, it's known that the Scattering cross-section area (C_{scat}) is given by:

$$C_{scat} = \frac{\text{Scattered Power}}{\text{Incident illumination intensity}} \quad (4.16)$$

This can be normalized using:

$$Q_{scat} = \frac{C_{scat}}{\pi a^2} \quad (4.17)$$

Where, Q_{scat} is the normalized scattering cross section, a is the radius of the particle.

Theoretically, the maximum signal to noise ratio is possible when the circuit is Shot noise limited. The minimum condition for which signal can be detected by the sensor can be expressed as:

$$i_{signal} \geq i_{shot} \quad (4.18)$$

Where, i_{signal} is the signal current and i_{shot} is the shot noise current. In the sensor, TI OPA 656 op-amp was used, with $f_{GBW} = 500\text{MHz}$. R_F was set to $150\text{ k}\Omega$ and C_D of the photodiode used in the sensor (Thorlabs FDS 1010) is 432 pF . Using these values and equation 4.7, $f_{BW} = 783.59\text{ kHz}$, which is the bandwidth of the circuit. i_{dark} of the given photodiode is 1.05 nA . The incident power on the particles is the laser diode output power, $P_{inc} = 5\text{ mW}$. The beam radius (r) of this laser diode is around 1.5 mm . The responsivity, $R(\lambda)$ of the photodiode at the red wavelength (633 nm) is 0.4 A/W .

The signal current can be expressed as:

$$i_{signal} = R(\lambda)C_{scat} \frac{P_{inc}}{\pi r^2} \quad (4.19)$$

Using equations 4.11, 4.17 and 4.18, it can be shown:

$$C_{scat} \geq \frac{\pi r^2 \sqrt{2q i_{dark} f_{BW}}}{R(\lambda) P_{inc}} \quad (4.20)$$

Using the given values, $C_{scat} \geq 5.718 \times 10^{-14} \text{ m}^2 \text{ sr}^{-1}$

Using Equation 4.17, minimum detectable diameter (d) of a particle which can be detected can be expressed as:

$$d = 2 \sqrt{\frac{C_{scat}}{\pi Q_{scat}}} \quad (4.21)$$

From Mie theory, it is known that Q_{scat} oscillates between 2 and 4. This can be shown graphically as well. Taking the lower limit of $Q_{scat} = 2$, $d = 0.19 \mu\text{m}$. This calculation indicates that, theoretically, the *minimum size of a particle that can be detected is 0.19 μm or 190 nm.*

Equation 4.20 offers key insights about the various trade-offs.

4.3. Embedded systems/interfaces

The microcontroller used was the TI MSP430 G2553. This is shown by Figure 4.18. [8].



Figure 4.18 TI MSP 430 G2553 [8].

The use of microcontroller enabled a sensor to be in a wearable form factor. The primary use of the microcontroller was to make use of the ADC10 module and display the particulate matter concentration on an LCD.

4.3.1. ADC considerations

The MSP430 G2553 has a 10 bit SAR (Successive Approximation Register) ADC which was programmed to count digitize the analog signals from the sensor and count the number of particles above a set threshold. The ADC10 gives a multiple options of selecting a reference voltage for the ADC conversion. It can either be an external reference, internal 2.5V or internal 1.5V. For achieving the highest resolution, internal 1.5 V was selected. The least significant bit (Δ) of an n bit ADC with V_{ref} reference voltage is given by:

$$\Delta = \frac{V_{ref}}{2^n} \quad (4.22)$$

This gives $\Delta = 1.46 \text{ mV}$. The ADC internal oscillator running at 5 MHz was selected as its clock source.

4.3.2. Static threshold counting algorithm

Initially, 100 samples were stored and then converted by the ADC in an array. However, this turned out to be quite slow and inefficient as there was lag time between those 100 samples. The fact that the ADC takes 13 clock cycles for conversion for each measurement after the sampling time adds to this. The algorithm can be illustrated by the flow chart shown in Figure 4.19.

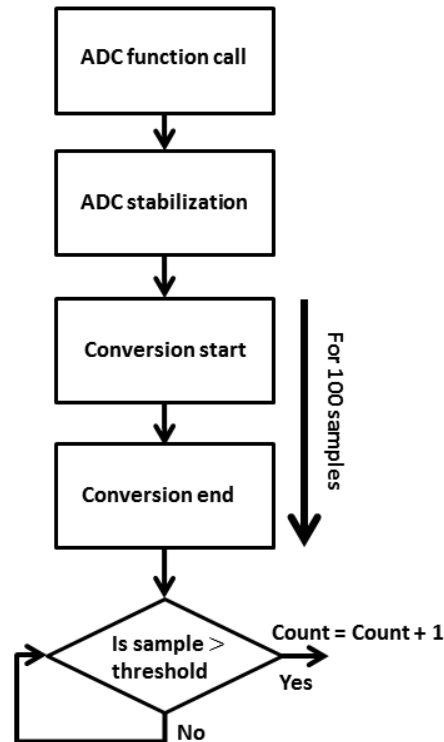


Figure 4.19 Static threshold counting algorithm.

After the ADC function was called, the ADC took some clock cycles to stabilize before sampling could take place. After this, 100 samples were sampled by the ADC and were converted to their corresponding digital values. It would be later experimentally shown that the peak to peak noise voltage amplitude was found to be around 1 mV. This analog value plus 0.5 mV were added and then converted to its corresponding digital value, which was set as the threshold. The 100 samples, which were stored in an array were compared against this threshold, and the count value was updated accordingly.

Code profiling using Timers was done to get an idea of how much each segment of the code was taking. The results are shown in Figure 4.20.

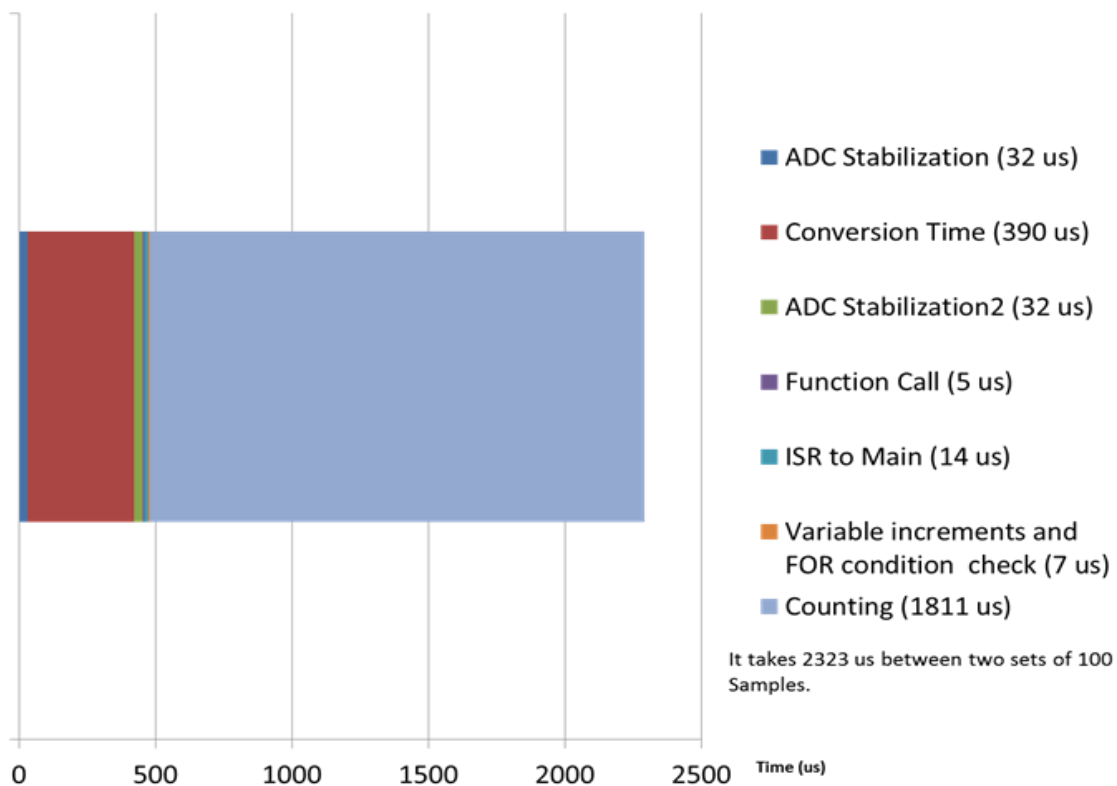


Figure 4.20 Code profiling results.

- The total time taken for the 1st 100 samples to process is given by the sum of ADC stabilization time and conversion time = 422 μ s.
- The time lag till the start of conversion of the next 100 samples is given by the sum of ADC stabilization time, function call time, time taken by the ISR to go to main function, variable increments and FOR loop condition check, and time taken for counting pulses above threshold value = 2323 μ s.

The long gap between each set of 100 samples makes this far from a real time acquisition, which shows the limitations of such a low cost, 8-bit microcontroller.

4.3.3. Dynamic threshold counting algorithm

Changes to the ADC algorithm were made in order to simplify the logic. Instead of storing a set of 100 measurements and converting them, each sample was then converted sequentially, and compared against a dynamic threshold. If the measured value was greater than the set threshold, the count was increased. The ADC conversion process for a single measurement was seen in the oscilloscope this time, shown in Figure 4.21.

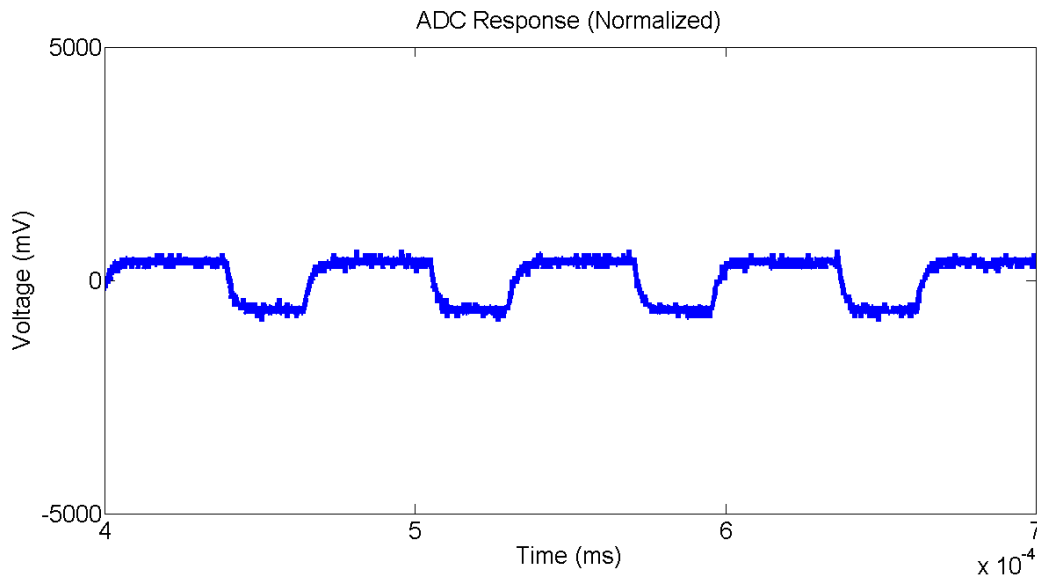


Figure 4.21 ADC response

It was found that *the entire processing time for a single sample, including the sampling, conversion, computation, etc was about 64 μ s. This corresponded to about 16 kHz.* This is still very low than the signal frequency, but an improvement from before. Another observation was the fact that the USB power supply to the MSP430 was injecting more than 100 mV peak to peak noise voltage. To fix this, the MSP 430 was power using a battery via a 3.3 V voltage regulator. The LCD (Nokia 5510 display) interfacing with the microcontroller is shown in Figure 4.22.

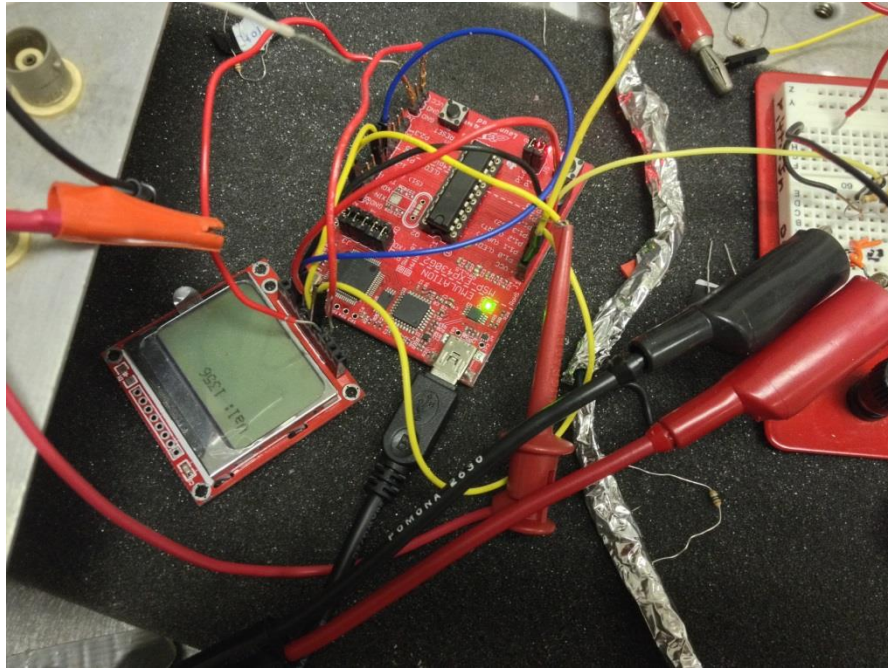


Figure 4.22 MSP430 interfacing to LCD.

For the lab experiments and data collection, the Tektronix DPO 4104 oscilloscope was used. To give a relative comparison with the oscilloscope sampling rate, during the experiments, the oscilloscope measured 10000 samples in a time interval of 100 ms. The MSP 430 was able to measure 1564 samples in 100 ms, which is roughly 6th sample for every sample measured by the oscilloscope.

The Static threshold counting algorithm described before suffered from one drawback. A major problem while counting with the microcontroller was the fluctuating DC level of the signal with the flow. In the previous algorithm, an absolute threshold value was

set based on the noise level. However, the noise and the signals ride on top of the DC level. Because of the static nature of the previous algorithm, if the DC level fluctuates during the measurement, many signal counts are missed. This made the counts random in nature.

A new counting algorithm was implemented to automate the process of threshold setting. To fix this, successive difference of the samples were measured to remove the dependence on the absolute value of the DC level. In the new counting algorithm, a feature was added which monitored the difference between the first 10,000 samples and then set the threshold difference value with the press of a button in the MSP430 Launchpad. At this moment, the flow was OFF. Next, the flow was turned ON and another button was pressed. The counts were then calculated by comparing the difference values of the next 30,000 samples against the threshold set during the previous step. This method added robustness to the counting algorithm to deal with variations during different measurements. Consistent particulate counts were observed with varying flow rates. This is illustrated using a flow chart in Figure 4.23. The results will be discussed in Chapter 5.

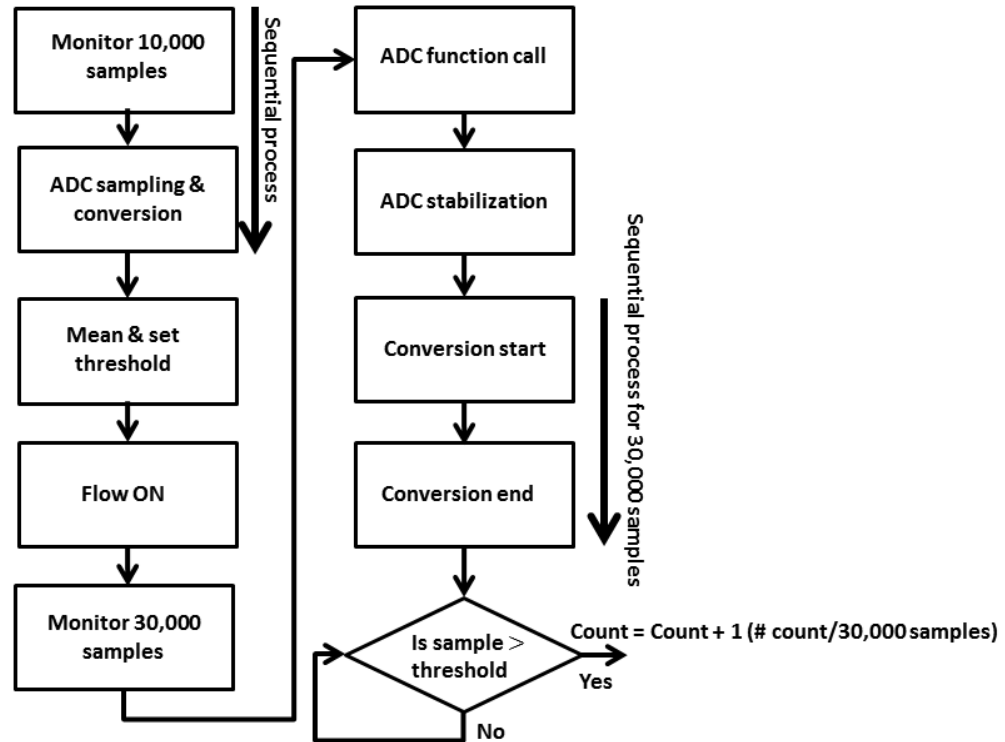


Figure 4.23 Dynamic threshold counting algorithm flowchart.

4.3. CAD/Prototyping

In this section some of the design aspects of the CAD design, which was 3D printed will be discussed. All the CAD designs were made using SolidWorks.

The initial design was to test a generic sensing scheme based in scattering but without using any optics. Various parts of the design are shown in Figures 4.24 - 4.26 respectively. The 3D printed design is shown in Figure 4.27

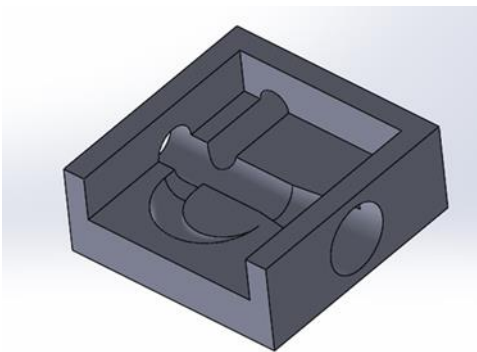


Figure 4.24 Top part of the prototype

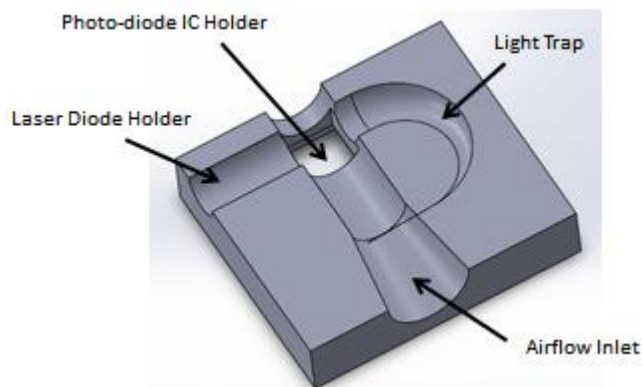


Figure 4.25 Bottom part of the prototype

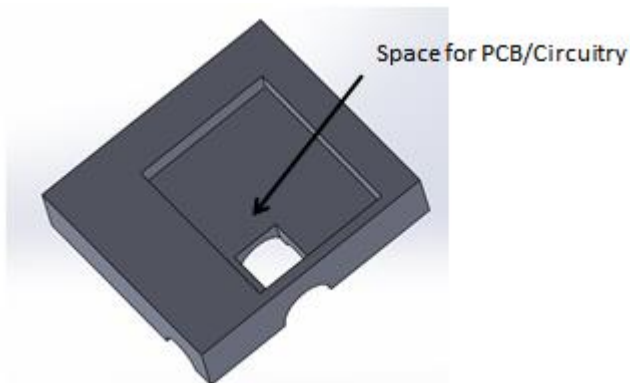


Figure 4.26 Bottom part of the prototype (Back Side view).

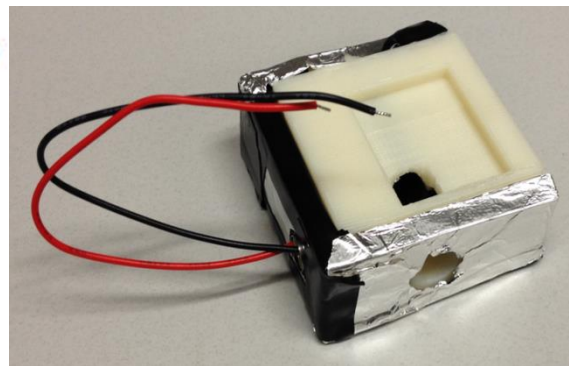


Figure 4.27 1st 3D printed prototype.

The initial version of the design was made into two parts for ease of printing and the dimensions were 5 cm x 5 cm x 2 cm. There were a couple of drawbacks because of which this design was not pursued further. The design was built around the TI OPT101 monolithic photodiode. However, it was later observed that its active area of 2.8 mm x 2.8 mm was too

small to focus the scattered light. Also, the light trap design was backreflecting the light back to the photodiode, resulting in incorrect measurements. Also, the airflow inlet was bigger than the laser diode beam diameter. The importance of this will be described in the design of the next version.

The CAD design is shown in Figures 4.28 and 4.29 respectively.

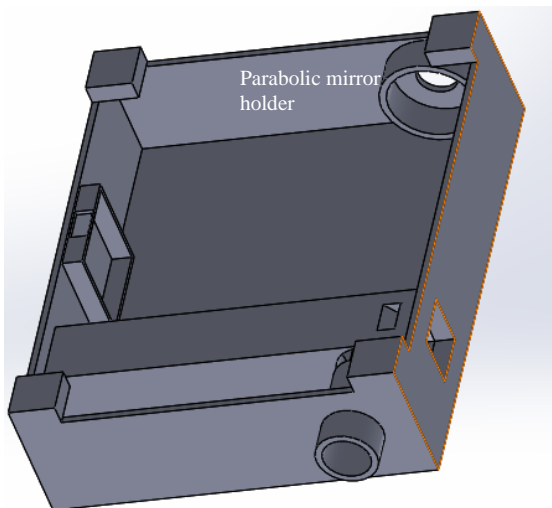


Figure 4.28 CAD design 2nd version.

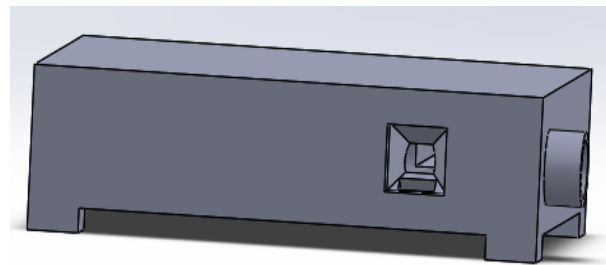


Figure 4.29 Tapered Flow inlet.

The printed design with components is shown in Figure 4.30.

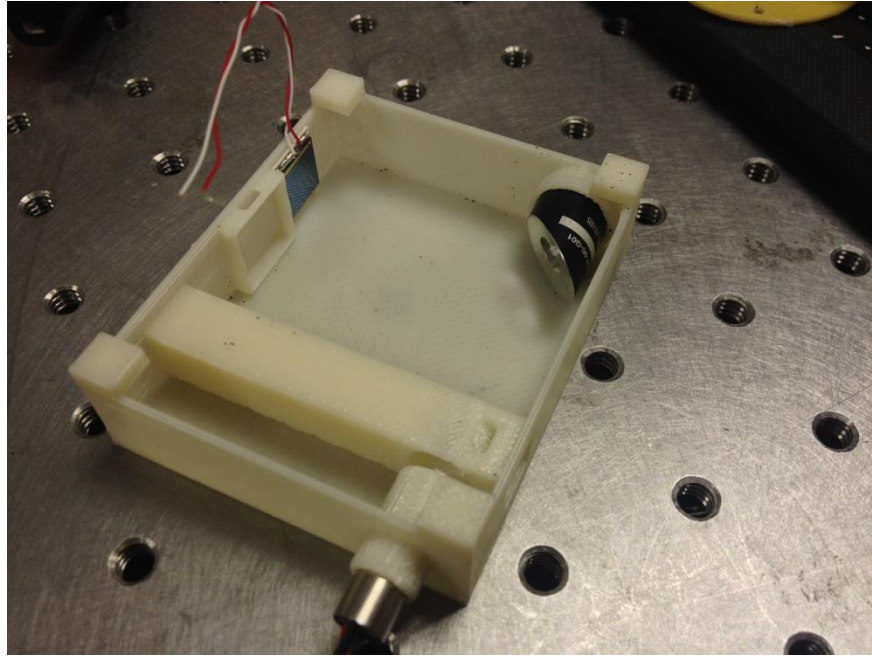


Figure 4.30 3D printed version.

The dimensions of this design is 6 cm x 4cm x 2 cm. Figure 26 shows the tapered design of the of the flow inlet. The importance of this is shown by Figure 4.31 [9].

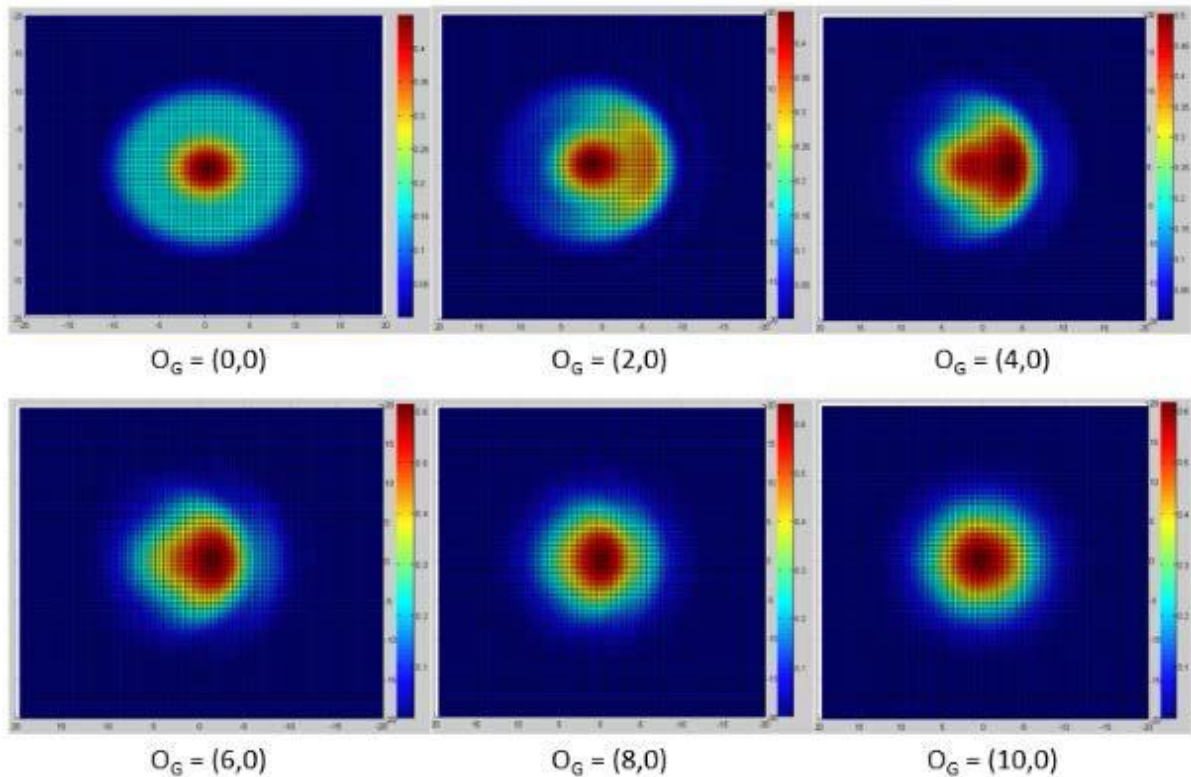


Figure 4.31 Total forward field after scattering by on-axis and off-axis particles, O_G [9].

It can be seen in that the fields deviate from the Gaussian profile when the particle is near the center of radiation. When the particle is far away from the beam axis, the influence of the particle decays and the resulting field roughly returns to a Gaussian profile. So, *it is important to distinguish between the signals obtained from a small particle going through the center of the beam and a large particle going through the edge of the beam as they have similar intensities*. In the CAD design, the flow inlet is tapered to 2 mm width, smaller than the beam width of 3mm, to reduce this problem.

4.4. Power consumption estimate

The major components which draw power in the sensor are the laser diode, Op-Amp, microcontroller and the photodiode.

- The laser diode draws 31 mA at 5 V supply. This is 155 mW.
- The LM 358 Op-Amp has a supply current of 0.5 mA at 5 V supply. This is 2.5 mW.
- Since the photodiode is not reverse biased, it draws negligible current, as the dark current is in the range of nA.
- The TI MSP430 draws only 250 μ A at 3.3 V supply. This is only 759 μ W or 0.759 mW.

So, **the total approximate power consumption is ~159 mW.** This can be effectively made better if the laser is run using a duty cycle.

REFERENCES

1. Thorlabs, Off-Axis Parabolic Mirrors,
http://www.thorlabs.com/newgrouppage9.cfm?objectgroup_id=7003.
2. Quarton Laser Module – Economical Dot Laser,
http://www.quarton.com/product_content/1/11/30/28/.
3. Vik Dhillon, ‘Reflectors and aberrations’,
http://www.vikdhillon.staff.shef.ac.uk/teaching/phy217/telescopes/phy217_tel_reflectors.html.
4. Photonics and Optical Communications, ECE 523 slides by Dr. Kudenov.
5. Thorlabs FDS1010 photodiode datasheet,
<http://www.thorlabs.com/thorcat/2700/FDS1010-SpecSheet.pdf>.
6. Xavier Ramus, ‘*Transimpedance Considerations for High-Speed Amplifiers*’, Texas Instruments, Application Report, SBOA122–November 2009.
7. Jerald Graeme, ‘*Photodiode Amplifiers: OP AMP Solutions*’, McGraw-Hill Professional; 1 edition (December 1, 1995).
8. Texas Instruments MSP430 G2553 Mixed-Signal Microcontroller datasheet, SLAS735J –APRIL 2011–Revised May 2013.
9. Yifan Wang, ‘*Airborne Particulate Matter Sensing with Micro-Optics*’, M.S. Thesis, North Carolina State University, Summer 2014.

Chapter 5 Experiments & Analysis of Results

In this chapter, the various experiments undertaken and the results obtained will be analyzed.

5.1. Initial bench-top experiment

The first experiment involved a proof of concept bench top experiment to mimic the actual optical sensor. This is shown in Figure 5.1.

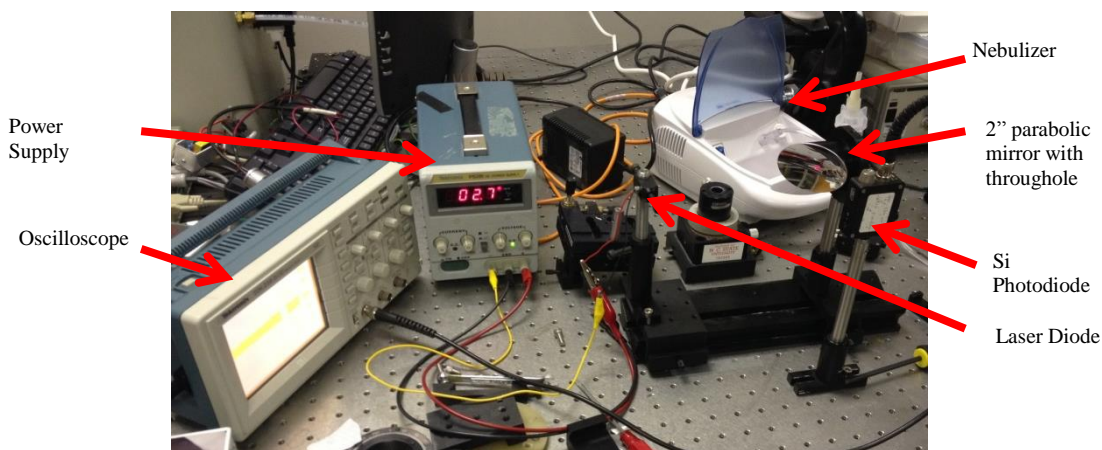


Figure 5.1 Initial bench top experiment.

From basic optics, it is known that, for a parabolic mirror, an object placed at a distance $2f$ (f is the focal length) or beyond, forms an image at f . The laser diode was placed at a distance greater than $2f$, so that the scattered light, after being reflected from the mirror is focused onto the photodetector. This configuration was chosen because of its known characteristics

and ease of setting up. The photodetector used here was a Thorlabs DET10A Si detector, with no adjustable gain. The laser diode was given a bias of 5V and the nebulizer was held by hand close to the laser diode aperture to introduce the particles in the beam. The response when the flow was OFF is shown in Figure 5.2.

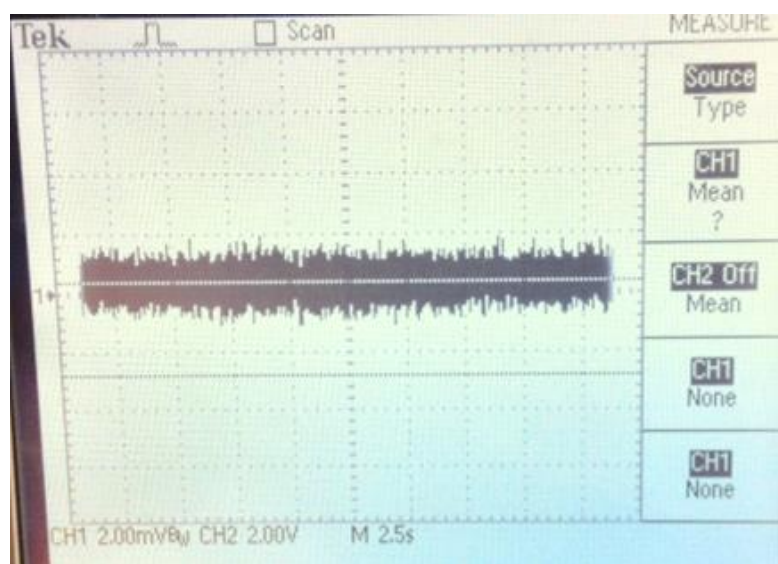


Figure 5.2 Response with flow OFF.

When the flow was OFF, there was no scattering as there was no external force to drive the particles in the path of the laser beam. The peak to peak noise voltage amplitude was around 2 mV. Part of this noise was contributed by the stray light, which adds a DC component to the Shot noise.

The response, when the flow was turned ON, is shown in Figure 5.3.

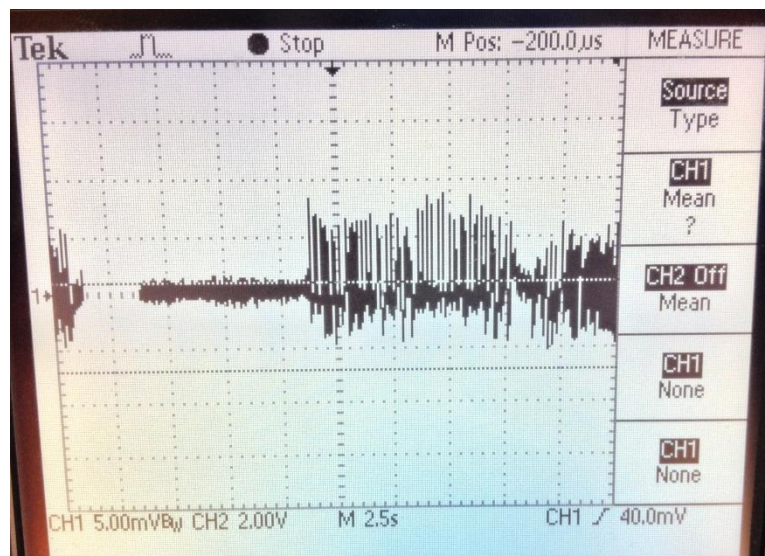


Figure 5.3 Response with flow ON.

The response shows positive spikes with peaks around 9 mV. The peaks started to occur when the flow was turned ON. The nebulizer output particle size ranges from 0.5 μm to 10 μm . The peaks show that the photodiode was able to detect this size range. The amplitude of the peaks is proportional to the size of the particles passing through the beam, as discussed before.

In the next experiment, the DET10A photodiode was replaced with a higher performance, PDA100A Si amplified detector. The detector was set to 60dB gain setting to see the effect of photodetector performance on the measurements. The oscilloscope was changed from Tektronix TDS 210 to Tektronix DPO 4104 to store data in .csv format so that it could be processed in MATLAB for better analysis. The acquisition time was set to 100 ms. The response is shown in Figure 5.4.

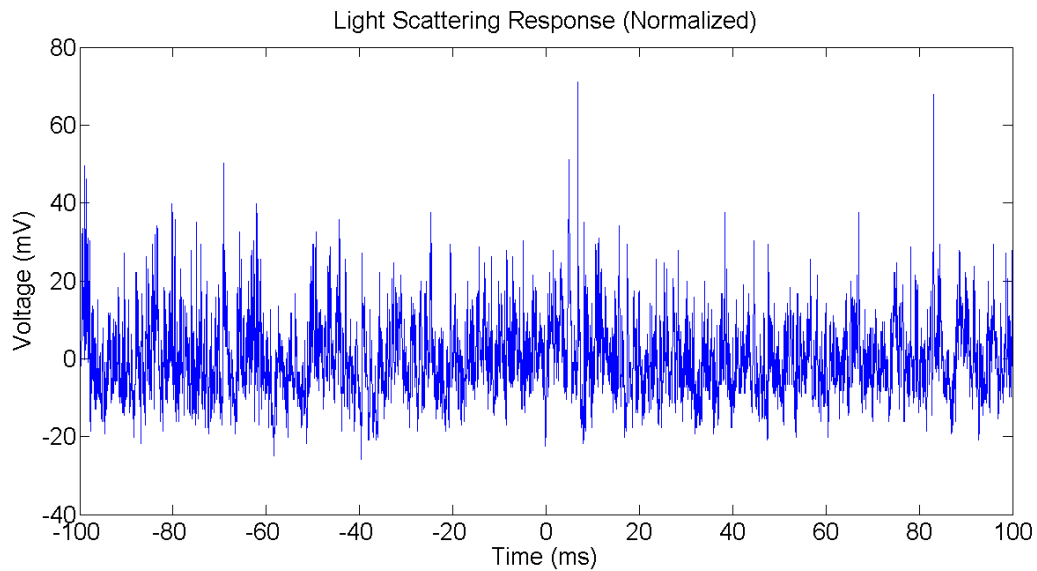


Figure 5.4 Response with Si amplified photodetector.

The data acquired from the oscilloscope was normalized to the mean value and plotted using MATLAB. This shows distinct, high amplitude positive spikes which show the performance of the amplified photodiode. The maximum amplitude of the positive peak was around 70 mV. This kind of response makes the data analysis much easier but it is important to note that the gain amplification also amplifies the noise amplitude. This was seen by the amplified negative spikes greater than -10 mV. Even though, at first glance, the response looks impressive, it is important to account for the noise amplification, which might make the signal to noise ratio smaller than what it looks like. The above experiments demonstrate the feasibility of the sensor design. The Signal to Noise Ratio (SNR) of this experiment can be defined by:

$$SNR = 20 \log \left(\frac{V_{signal}}{V_{noise}} \right) \quad (5.1)$$

Where, V_{signal} and V_{noise} are peak values of signal and noise, respectively. For this experiment, the peak signal amplitude is 70 mV and peak noise amplitude is 10 mV, resulting in an ***SNR of ~17 dB.***

To see what the response looks like in the frequency domain, a FFT (Fast Fourier Transform) was taken for the response shown in Figure 5.4. The FFT response is shown in Figure 5.5.

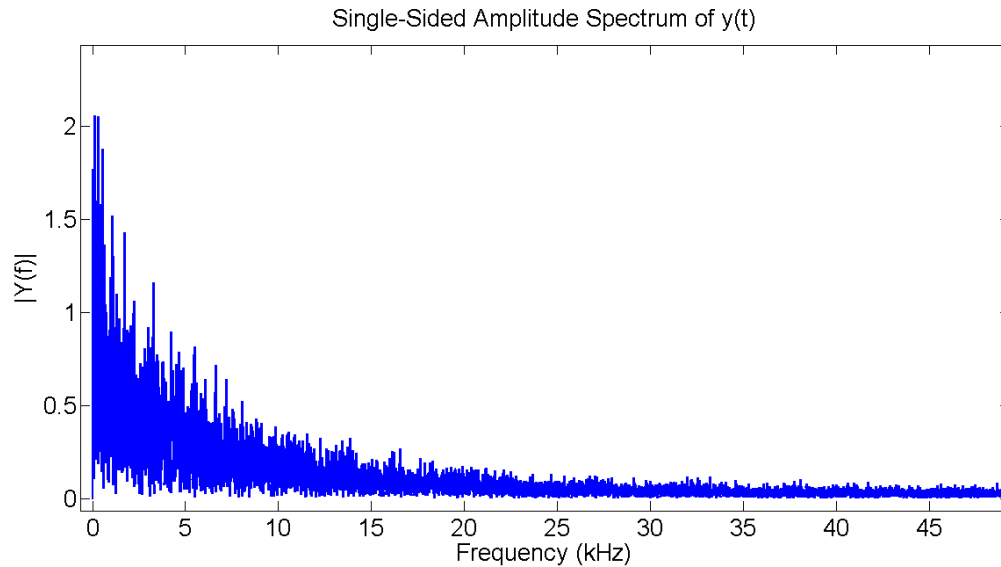


Figure 5.5 FFT of response with Si amplified photodetector.

It is observed that the DC component of the response has the maximum signal power. The particle flow causes light scattering which results in signal peaks of different amplitudes at different frequencies. This is observed in FFT by the signal peaks in frequencies ranging from 0-20KHz.

5.2. Sensor design test

In the next experiment, the proposed optical sensor design was put to test. A schematic of the test setup is shown below in Figure 5.6.

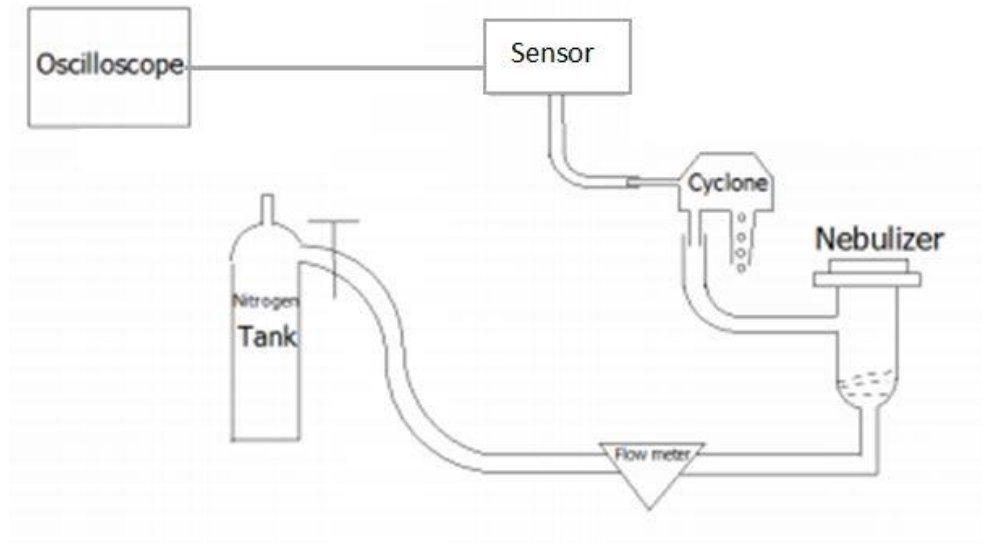


Figure 5.6 Schematic of the sensor test setup.

The source of particle generation was the medicine cup of the Mabis CompMist compressor nebulizer. It mixes water with a stream of air to form water particulates of sizes ranging from $0.5 \mu\text{m}$ to $10 \mu\text{m}$. A nitrogen tank was used as a controlled source of air flow. The flow was regulated using the valves attached with the tank and the flow rate was measured using TSI 4040 flow meter. The particles generated by the nebulizer were directed into a SKC conductive plastic segregating the particles based on the cut point vs flow rate curve for the cyclone. The segregated particles were then introduced in the sensor device via a pipe where light scattering occurred and the scattered light pulses were focused onto the photodiode by the parabolic mirror. The converted electrical signal from the photodiode was displayed in the oscilloscope (Tektronix TDS210). The acquisition time was set to 100 ms.

The amplitude of the scattered light pulses indicate the size of the particle detected, given that the refractive index of the particle is known.

The plastic cyclone was introduced in the experimental system to restrain the largest particle size in the particle blend passing through it. It is a simple and popular way to separate particles since it is fairly easy to maintain. As described in [1], the ‘dirty’ air flow enters the cyclone tangentially. Since the heavier particles tend to revolve in a larger radius, their trajectory is closer to the sidewalls. Thus, they slide down along the wall and are removed from the bottom opening. Lighter particles revolve in a smaller radius and get out of the cyclone from the top, along with the air flow. The cut-off particle size of the cyclone is related to the air flow rate through it. Usually, a larger flow rate would generate smaller cut-off size. Although the exact data of the product in our experimental system was not found, a curve illustrating the relation between flow rate and the 50% cut-off point for a similar cyclone (which is made of aluminum) was found on the website of SKC company. Since the aluminum cyclone is of the same series of products, plus the fact that only two known data points of the plastic cyclone both lie near the curve, it was assumed that the following curve is also applicable for the plastic cyclone. Figure 5.7 [2] shows the curve.

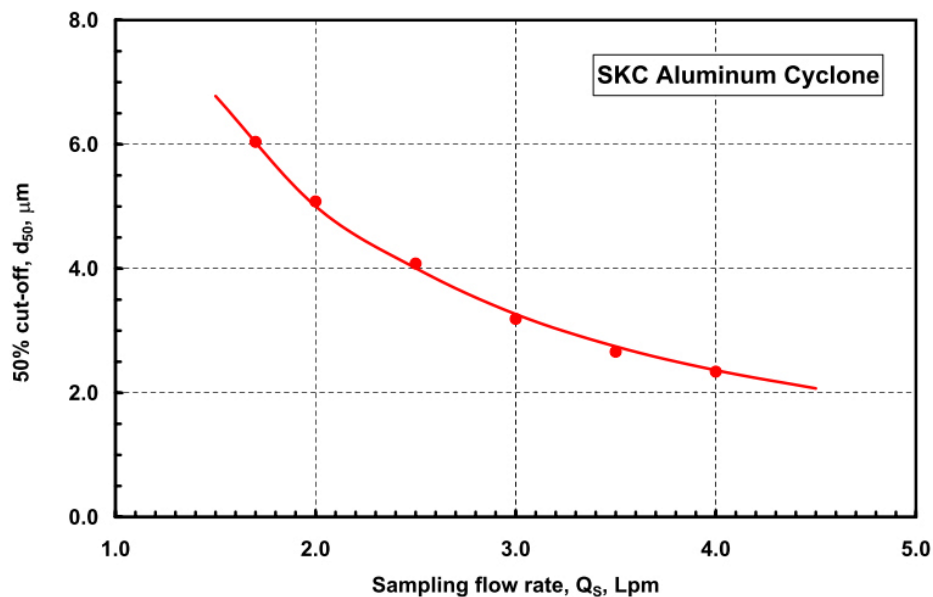


Figure 5.7 SKC cyclone: relation between input flow rate and 50% cut-off point of particle size [2].

The 50% cut-off point is the particle size at which the cyclone separation efficiency is at 50%, is an important parameter for cyclone particle samplers. Using the data points from this curve, another curve was plotted in MATLAB and shape-preserving extrapolation was used to find the 50% cut off points for flow rates ranging from 1.5 lpm to 4.7 lpm. This is shown in Figure 5.8.

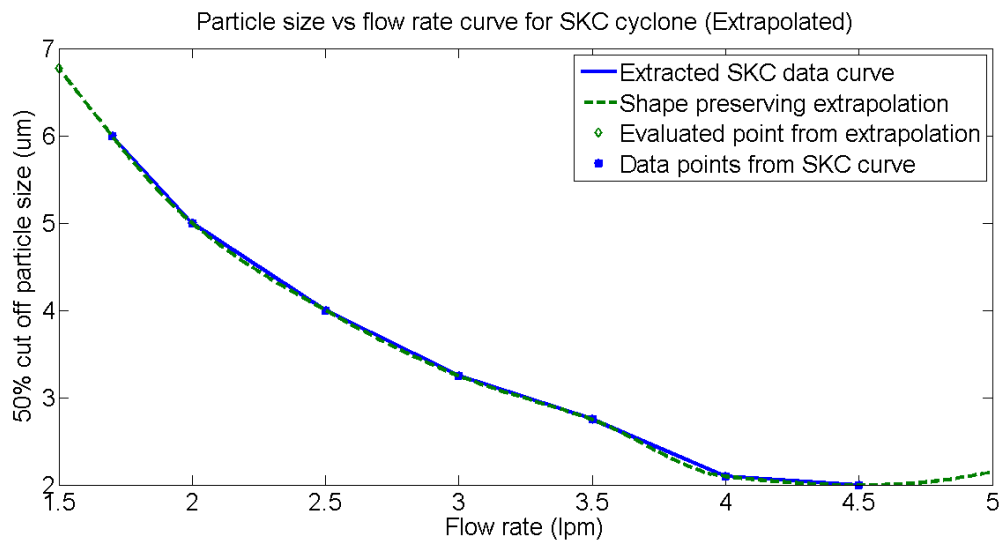


Figure 5.8 Extrapolated particle size vs flow rate curve.

The picture of the actual setup is shown in Figure 5.9.

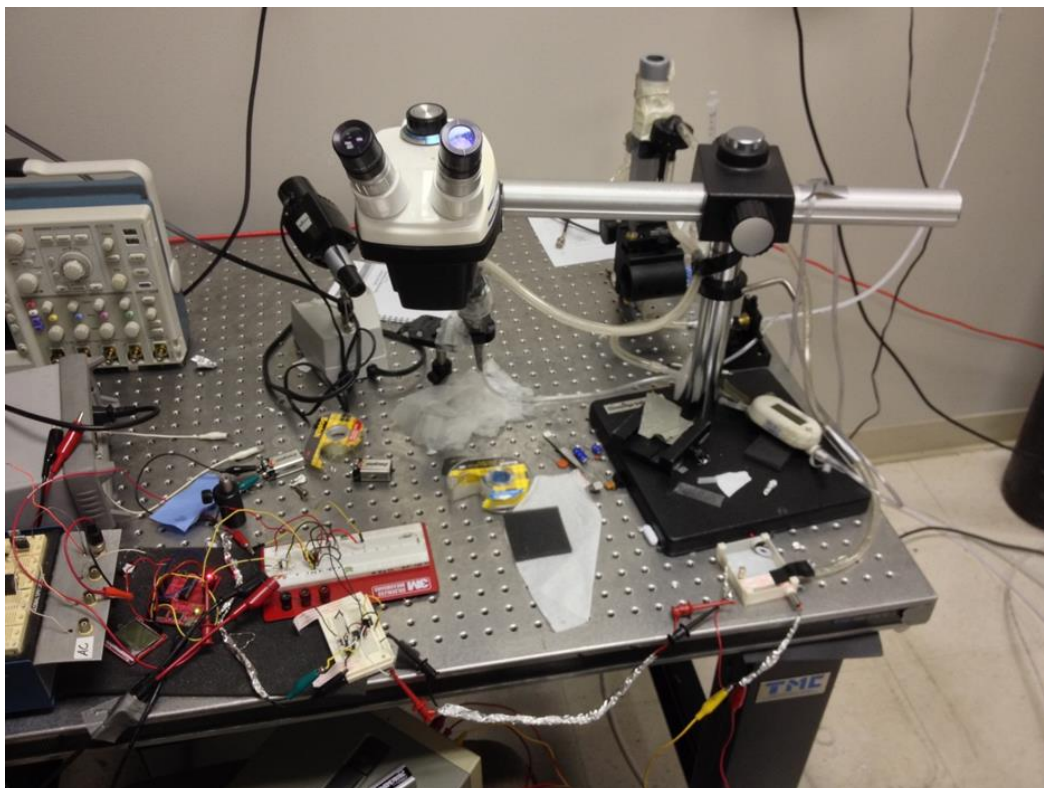


Figure 5.9 Picture of the sensor test setup.

In the first experiment using the sensor, the nebulizer was operated *without the cyclone*. The forward scattered light pulses then represented *the entire size range of the particles generated by the nebulizer (0.5 μm to 10 μm)*. As explained before, the gain of the photodiode signal depends on the value of the feedback resistor (R_F) used in the transimpedance op-amp. For the first two measurements, feedback resistors of 270 k Ω and 330 k Ω were used. The signal responses when flow is OFF, flow is ON (3 lpm) for $R_F = 270$ k and $R_F = 330$ k Ω are shown by Figures 5.10, 5.11 and 5.12 respectively. The acquired data from the oscilloscope was normalized to the mean value in MATLAB and plotted.

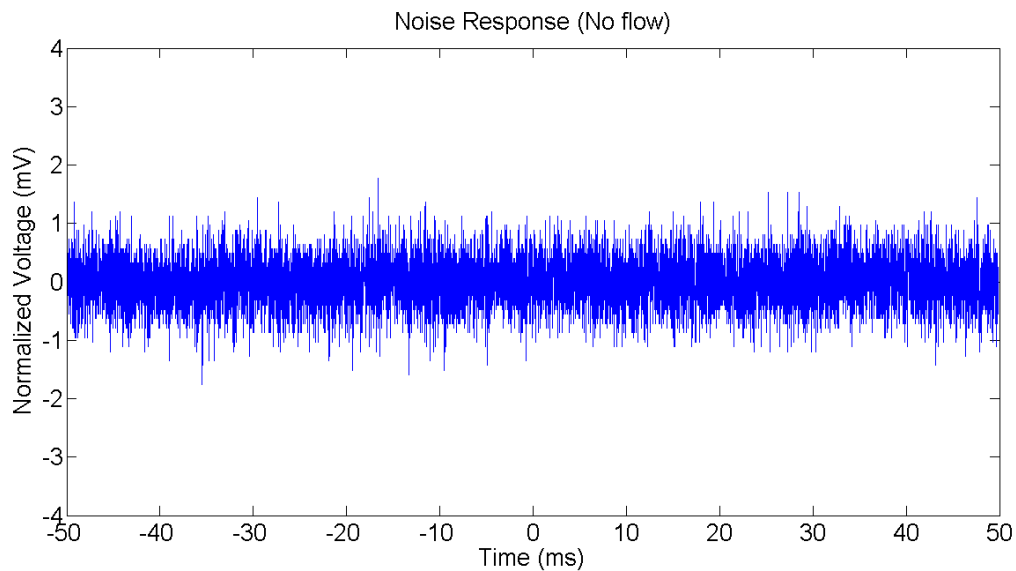


Figure 5.10 Response when flow is OFF.

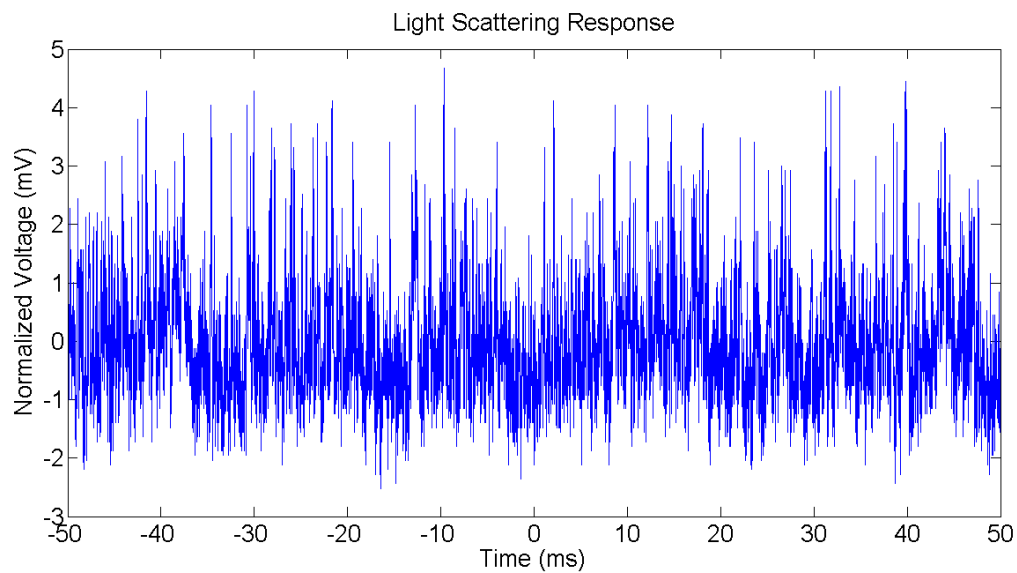


Figure 5.11 Light scattering response with $R_F = 270 \text{ k}\Omega$.

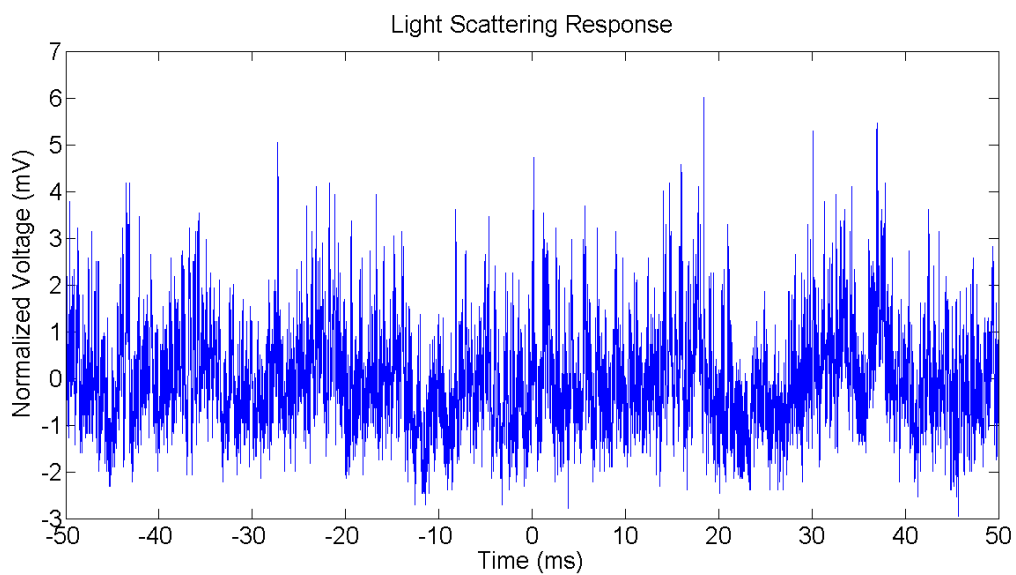


Figure 5.12 Light scattering response with $R_F = 330 \text{ k}\Omega$.

Figure 5.10 shows that the peak to peak noise voltage is below 1.5 mV. There are no positive spikes to show for forward scattering. Figures 5.11 and 5.12 show positive spikes illustrating forward scattering events. Also, it is observed that the signal peaks for $R_F = 330$ k Ω are higher when compared to the response with $R_F = 270$ k Ω . This is because R_F sets the gain of the transimpedance circuit as explained in Chapter 4. Compared to Figure 5.4, the DC levels of the responses are observed to be fluctuating a bit. This can be attributed to the circuit being unstable at high flow rates. This happens because at high flow rates, the signal frequency exceeds the bandwidth of the transimpedance amplifier circuit. This shows the superior performance of the expensive (~\$350) Si amplified photodetector with inbuilt circuitry and limitations of the cheap (~\$50) photodiode which needs external circuitry. However, the signal to noise ratio is still reasonable for particulate matter detection. The noise floor can be considered to be 1mV and the peak signal voltage is around 6 mV. This gives a *SNR (signal to noise ratio), defined by $20\log(V_{signal}/V_{noise})$ of 15.56 dB*. This seems pretty reasonable as compared to the SNR of 17 dB obtained with the bench top experiment using the high-performance Thorlabs PDA100A photodetector. This highlights the fact that increasing gain does not always help getting measurements. Noise and bandwidth trade-offs play an important role in determining the overall performance of the system.

The FFT plots for the above responses are shown by Figures 5.13-5.15.

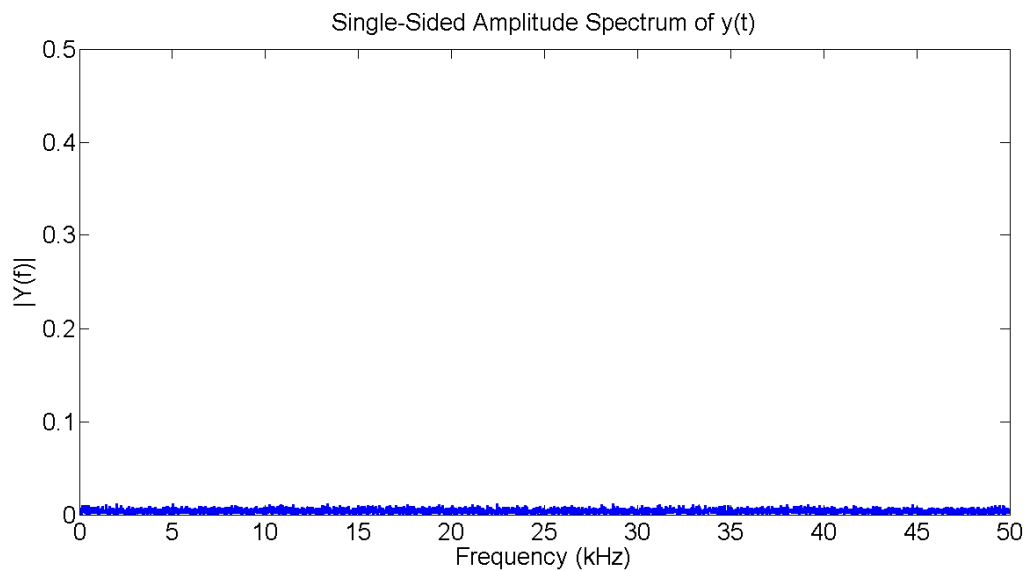


Figure 5.13 FFT when flow is OFF.

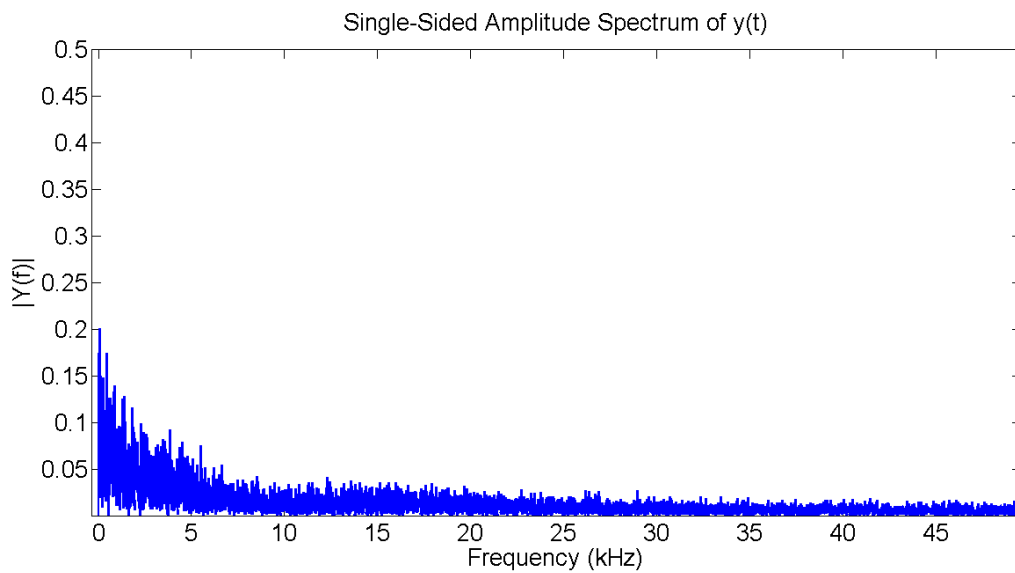


Figure 5.14 FFT of light scattering response with $R_F = 270 \text{ k}\Omega$.

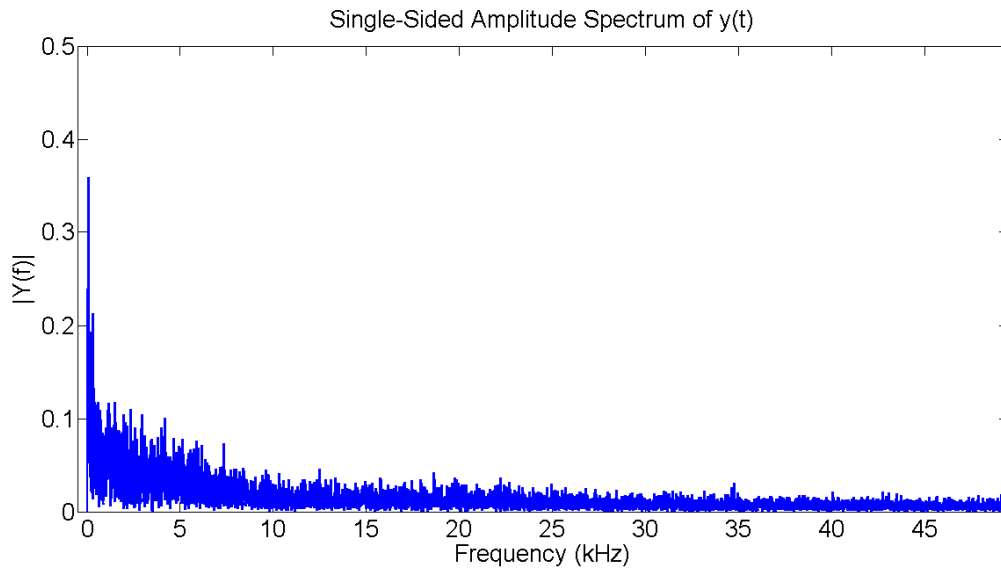


Figure 5.15 FFT of light scattering response with $R_F = 330 \text{ k}\Omega$.

When the flow is OFF, the FFT shows an absence of any signal characterized by the flat response. When the flow is turned ON, there are signal peaks in the low frequency range as were seen in Figures 5.14 and 5.15. For both the measurements, the flow rate was around 3.3 lpm. It was expected that the frequency response would not be much different. However, the higher gain set by the 330 k Ω feedback resistor results in slightly higher signal peaks at those frequency ranges, as compared to when the feedback resistor is set to 270 k Ω .

For the above measurements, the oscilloscope took 10,000 sample points in a period of 100 ms. This corresponds to a sampling frequency of 100 kHz. This was accounted for during the FFT computation in MATLAB and hence, the FFT spans upto half of the sampling frequency, i.e. 50 kHz, to avoid aliasing.

5.3. Statistical counting

Next, statistical counting of the forward scattered signals was undertaken. The noise threshold was set to 1 mV. The oscilloscope acquired 10000 samples in a period of 100 ms. Data acquired, was analyzed in MATLAB and number of particles were counted by setting a threshold. The number of particles obtained, were distributed according to the normalized scattered signal voltage obtained from the measurement. The particle counts were divided into bins of 5% scattered voltage amplitudes from the mean value. The number of particle counts in each bin was divided by the total number of particle counts over the threshold to calculate the probability distribution of the particles which results in specific ranges of scattered light pulse amplitudes. Figures 5.16 and 5.17 show this for $R_F = 270$ k and $R_F = 330$ k Ω , respectively.

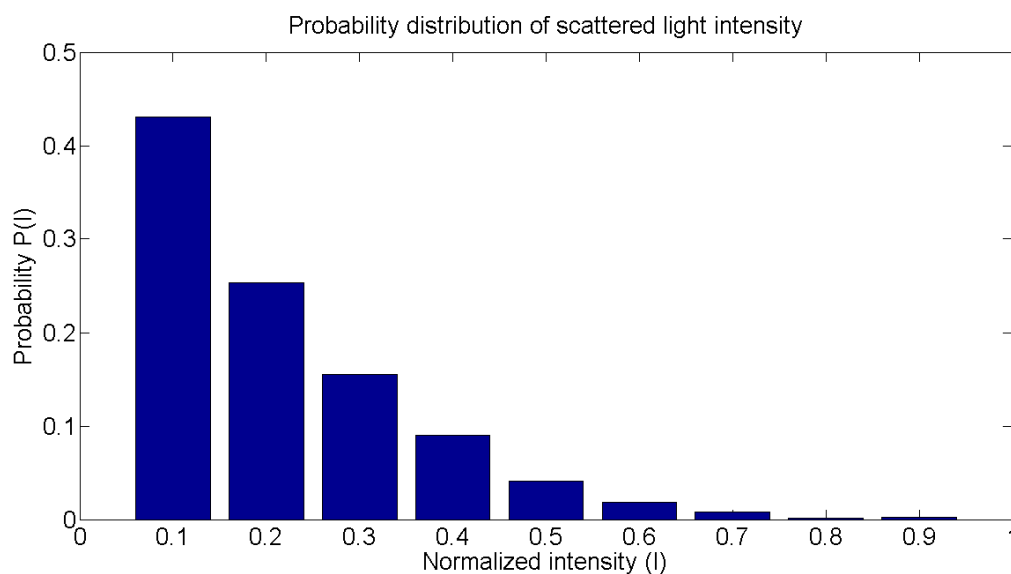


Figure 5.16 Probability distribution with $R_F = 270$ k Ω .

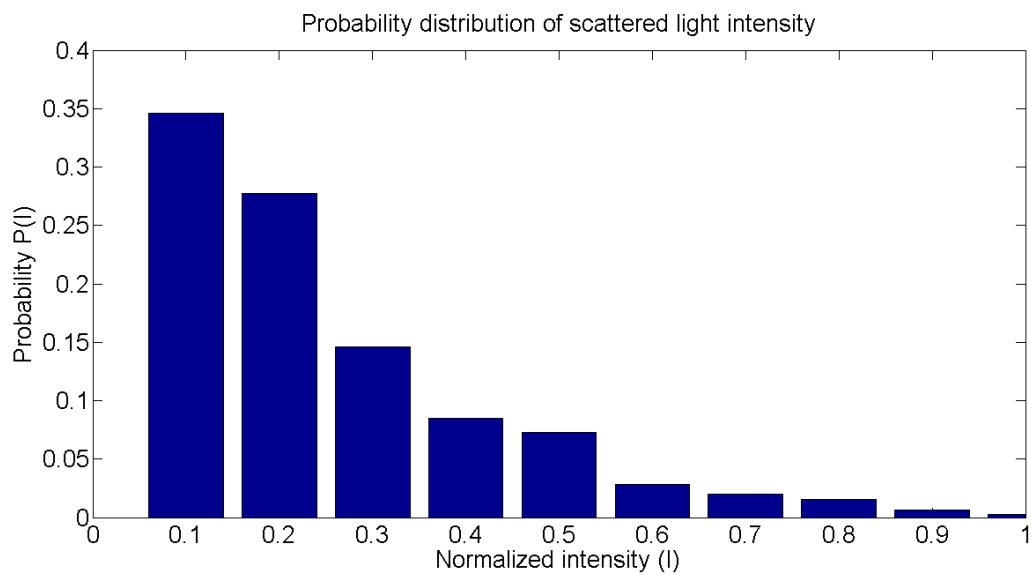


Figure 5.17 Probability distribution with $R_F = 330 \text{ k}\Omega$.

This is similar to the distribution obtained by Faxvog in 1973 in his extinction approach, as described in Chapter 2[1]. This is shown in Figure 5.18 [3].

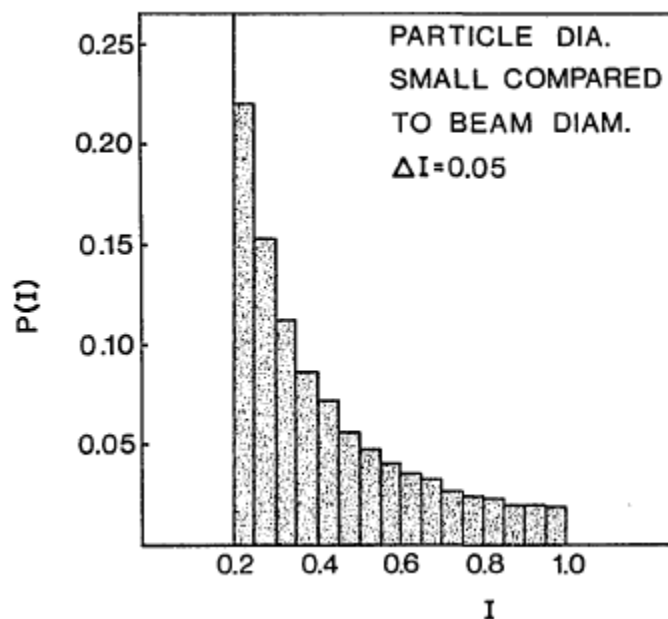


Figure 5.18 Probability distribution for small particles transiting various intensities of a focused Gaussian beam [1].

It can be seen that, the signal strength approximately follows a Gaussian distribution. This agrees with the general trend of particle size distribution from jet nebulizers [4].

5.4. Test with different flow rates

In the next experiment, the cyclone was introduced in the setup and the feedback resistor was changed to 150 k Ω to increase the bandwidth range of the circuit at high flow rates, used for testing. To verify the computation method that was proposed in the earlier chapters, theoretical curves of “Scattered amplitude vs Particle size” were drawn for water solution drops. Then tests were conducted under different flow rates, trying to fit the curves. The signal acquisition period was 100 ms for each flow rate. Only the largest pulse amplitude during this period is meaningful since the largest particle size is the only thing constrained by

the plastic cyclone. An underlying assumption is that, the largest energy drop was generated by the largest particle in the blend passing through the very center of laser beam profile. 17 measurements were taken with flow rates varying from 1.5 lpm to 4.75 lpm which correspond to 50% cut off point for particle sizes ranging from 6.39 μm to 1.5 μm . It was noted that the nebulizer started to generate particles reliably around 1.5 lpm. This is why the measurements were started from that flow rate. It is also noted that, the flow rate at the time of measurement can have upto 2% error, which might result in some offset while comparing theoretical and measured curves. The results are shown in Figure 5.19.

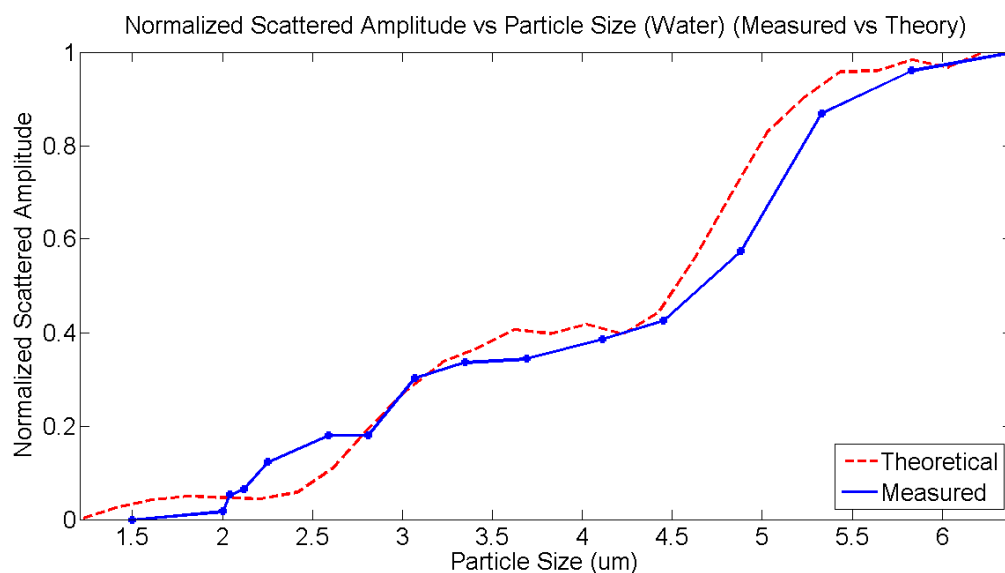


Figure 5.19 Measurements for water particles.

The measured curve follows the theoretical curve quite closely, especially for particle sizes between 2.8 μm and 4.45 μm . This is because these particle sizes correspond to flow

rates between 2.3 lpm and 3.3 lpm. The nebulizer performs better in terms of uniform particle generation after 2 lpm. As the flow rate is increased, the number of particles generated is increased, which corresponds to an increase in particulate matter concentration. Also, the increased flow rate means that the particles are faster through the beam. This increases the bandwidth requirement of the circuit as explained in Chapter 4. At high bandwidths, the feedback loop can become unstable which can result in oscillations. This can introduce some offset in the measurements at higher (>3.3lpm) flow rates. The upper limit of the particle size test was limited by the nebulizer as it starts to nebulize after 1.6 lpm which corresponds to a 50% cut off point of 6.39 μm . The lower limit of the particle size test is limited by the bandwidth of the circuit upto which measurements can be taken reliably and also the signal to noise ratio. This was found to be around 4.75 lpm which corresponds to a 50% cut off point of 1.5 μm . Another source of error is the cyclone itself. It is assumed that the maximum scattered amplitude in a measurement is due to the particle size given by the 50% cut off point of the cyclone at that given flow rate. However, larger particles can make their way through and be present during the measurement interval, resulting in amplitudes, larger than expected.

To understand the effect of flow rate on the frequency response, FFT's were taken for responses for flow rates of 1.92 lpm, 2.31 lpm and 4.51 lpm respectively. From the SKC cyclone data extrapolation done earlier, it is know that, these slow rates correspond to

particle sizes of 5.33 μm , 4.45 μm and 2 μm respectively. A comparative plot is shown in Figure 5.20. A zoomed in version is shown by Figure 5.21.

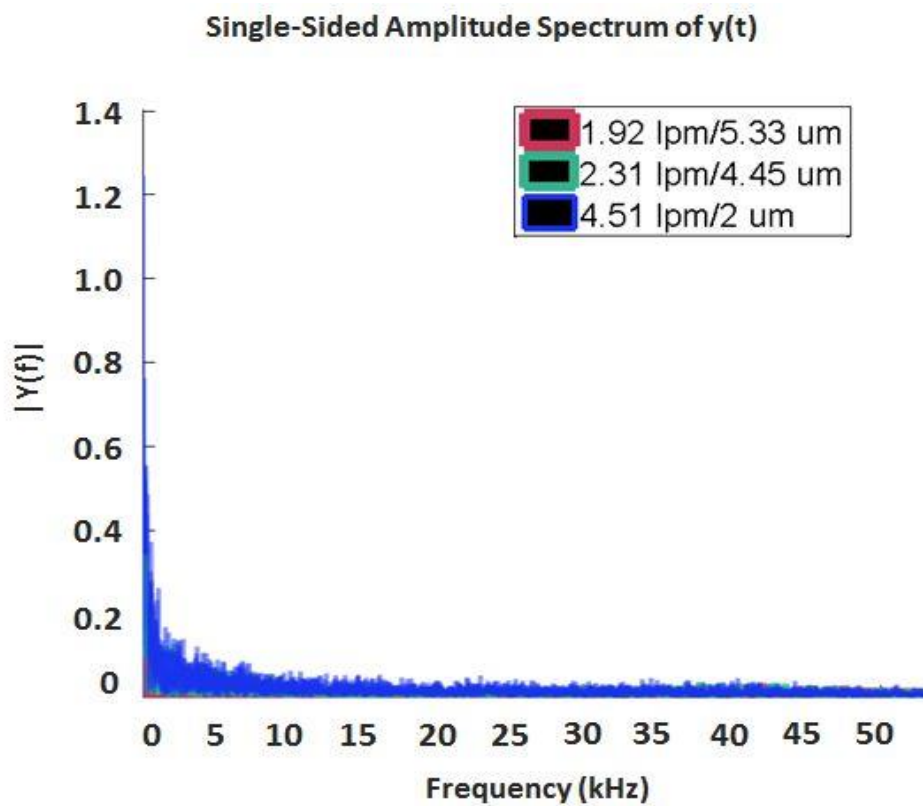


Figure 5.20 Comparative FFT analysis.

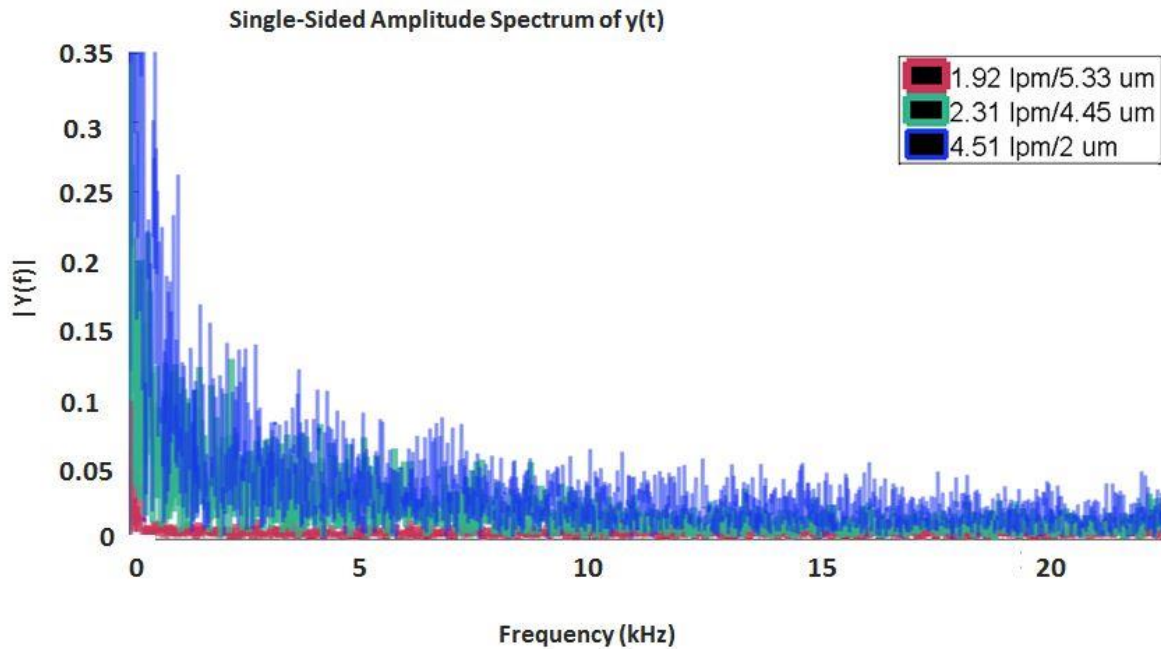


Figure 5.21 Comparative FFT analysis. (Zoomed in version).

It was observed that, the signal amplitude, increased at higher flow rates. This is because, more number particle pass through the laser beam and also the particle concentration generated by the nebulizer increases. This results in increased signal power at higher frequencies which are not prominent at lower flow rates. In this plot, the pink data represents 1.92 lpm. This is shown by low magnitude signal amplitudes. Also, it drops much sharper from the DC frequency. The green and blue data sets represent 2.31 lpm and 4.51 lpm respectively. As expected, the higher flow rate data shows higher signal amplitudes for frequency ranges that are not present for the lower flow rate data. Also, the high flow rate plots falls slowly from DC as compared to the low flow rate data.

Another test was done to isolate the signal peak due to single particle. In order to do this, the oscilloscope was set to a sampling frequency of 10 MHz and the response was zoomed in. This is shown in Figure 5.22.

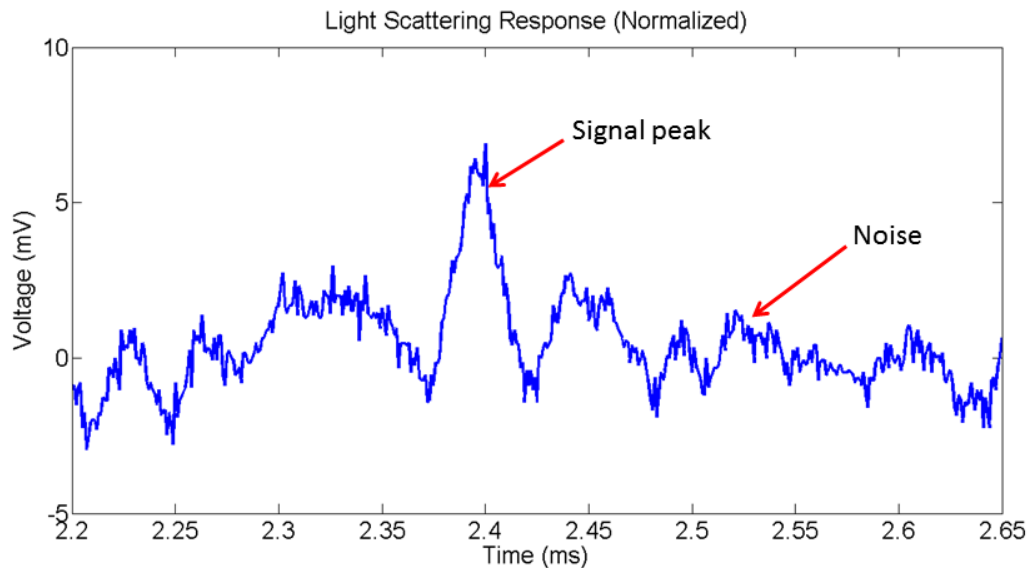


Figure 5.22 Signal peak due to individual particle.

For the response shown in Figure 5.22, the noise threshold is set to around 1.5 mV. The peaks above that are seen as signal peaks. The major sources of noise in the system are Shot noise, Johnson noise (Thermal) and noise due to stray light. The stray light is likely the limiting factor for this system. As such, the response due to the stray light will look similar to the response due to the signal, because both responses are due to optical signals, being converted into electrical signal by the photodiode and then amplified by the transimpedance amplifier.

However, beyond the set threshold value, the peaks tend to be more prominent in shape with narrow upward peaks, with a wide base region. The noise peaks, on the other hand don't have well defined peaks, and appear to be in a series of successive broken peaks and can't be isolated easily.

5.5. Test with smoke

In the next experiment, the sensor was tested with smoke produced from burning pieces of paper. The pipe from the nitrogen tank was now connected to a flask containing burnt pieces of paper which generated smoke. The outlet of the flask was connected to a sensor via a pipe. The flow was set to about 1 lpm to force the flow through the sensor. Figure 5.23 shows the result of this experiment. The probability distribution of the scattered light intensity is shown by Figure 5.24.

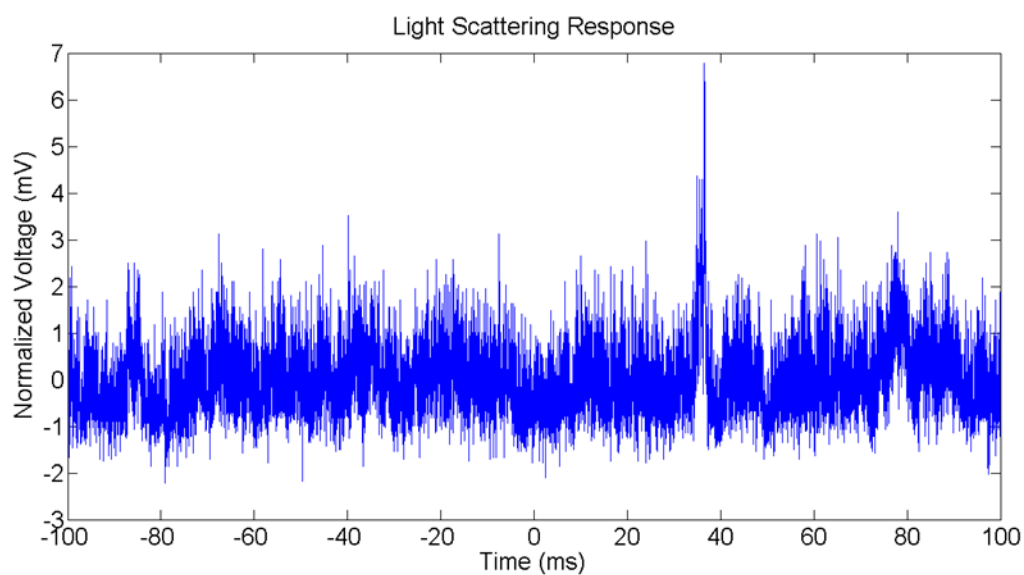


Figure 5.23 Test result from smoke experiment.

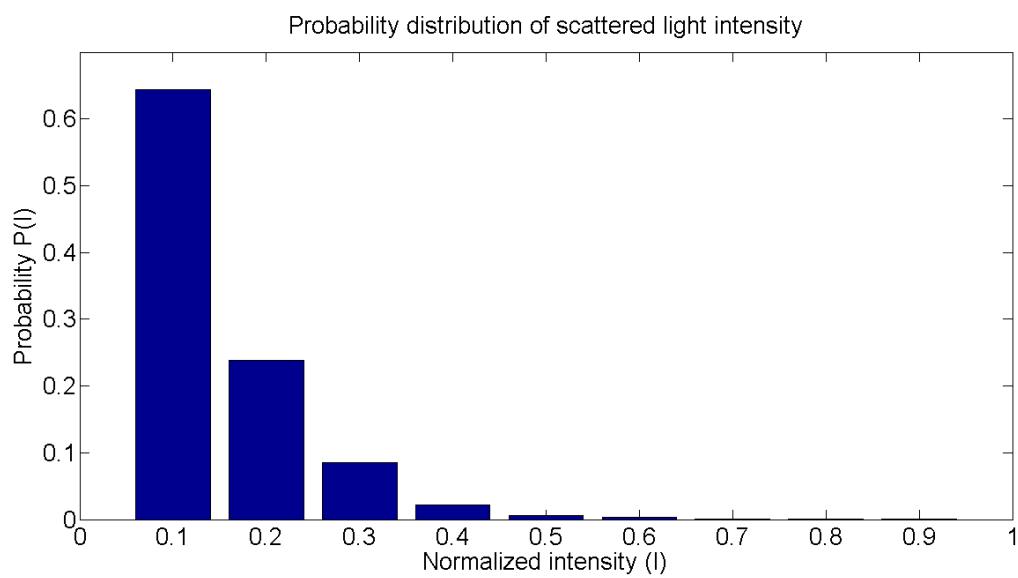


Figure 5.24 Probability distribution with smoke particles.

The major issue during the smoke experiment was to sustain uniform flow of smoke over long periods of time. This resulted in the number of smoke particles traversing through the beam to fall off quickly in about 20-30 seconds. This meant that by the time the measurement was finished, some of the high intensity peaks were lost, which is evident looking at the plot. Another issue is the bandwidth requirement for the smoke particle test. The burning of paper pieces produced a large concentration of smoke particles. Even though the flow rate was as slow as 1 lpm, the bandwidth is proportional to the concentration of the particles flowing through the beam. This resulted in DC level fluctuations, much higher than the water particle measurement. This made it harder to take consistent measurements. Nevertheless, the presence of some sparse, high amplitude peaks suggests that the sensor is capable of detecting smoke particles, given the circuit can cope up with the high bandwidth requirement and smoke can be generated for a long period of time. The probability distribution still shows Gaussian distribution. This confirms that the sensor can be used in practical scenarios.

5.6. Test after interfacing to TI MSP430 microcontroller and LCD

In the next experiment, the sensor is interfaced to the MSP430 microcontroller and the particle counts were displayed on a LCD screen hooked up to the microcontroller. This is shown in Figure 5.25

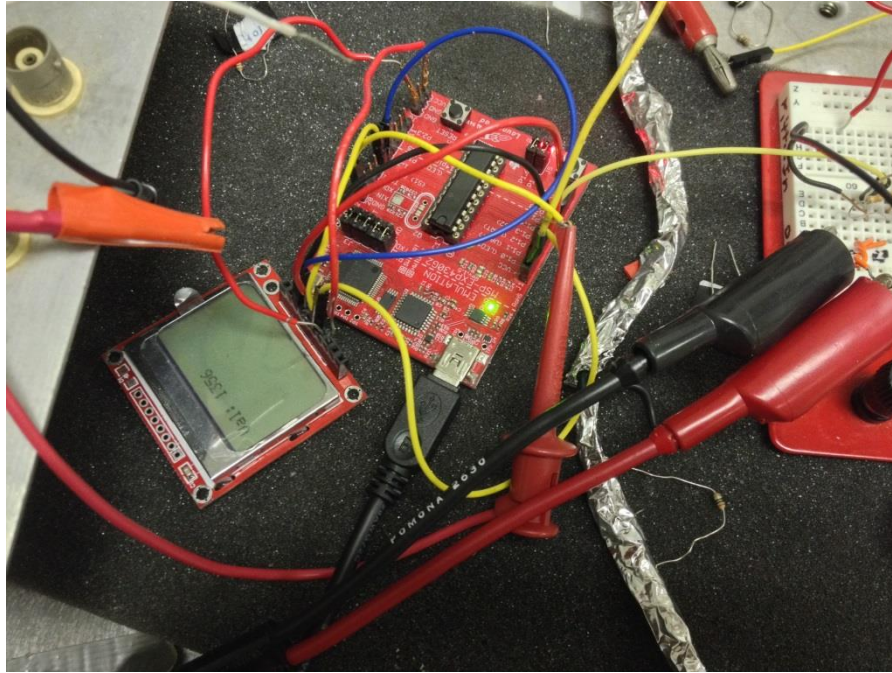


Figure 5.25 Test with microcontroller.

The reason that the particle counts were displayed on the LCD instead of the Code Composer Studio debugger in computer was because of noise injection by the USB supply to the supply rails of the circuit. When the microcontroller was powered by the USB, it injected noise in excess of 100 mV peak to peak, much higher than the signal amplitude. To fix this, the microcontroller was powered via battery, with a 3.3 V regulator.

Another major issue was the interference of the digital and analog grounds. Essentially, the clock source of the microcontroller oscillates the analog ground along with it, injecting high frequency noise in the response. To fix this, a separate breadboard was used to power the microcontroller. The two breadboard grounds were shorted via a wire. This is

analogous to PCB where analog and digital ground planes are shorted at a single point. This minimizes the interference to a large extent. Figures 5.26 and 5.27 show this.

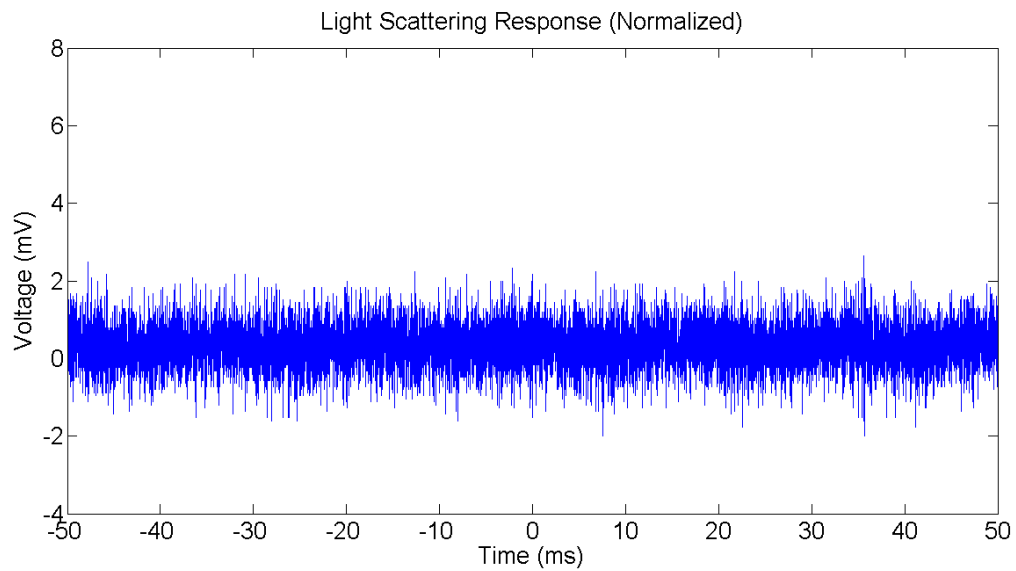


Figure 5.26 Noise when microcontroller is OFF.

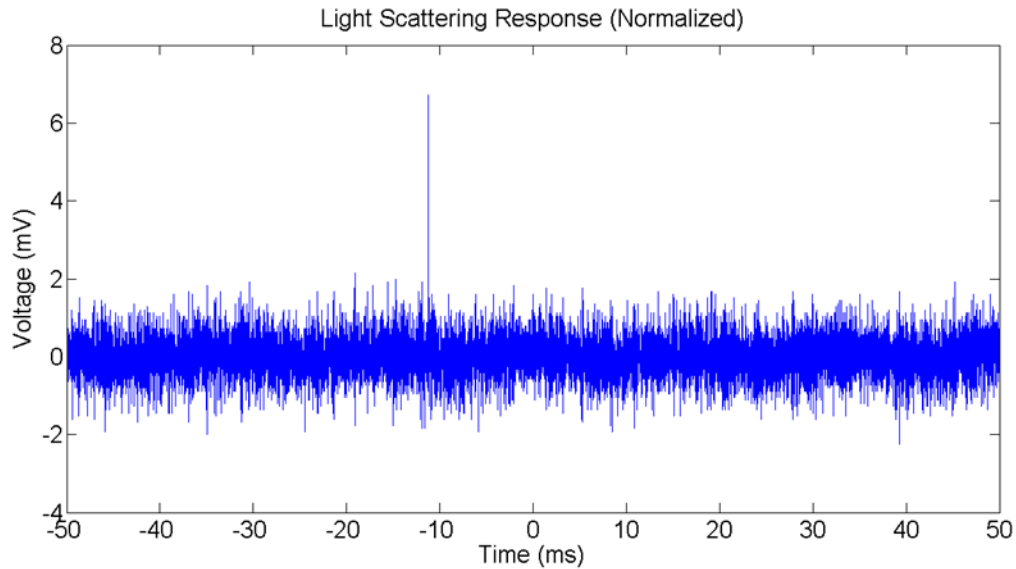


Figure 5.27 Noise when microcontroller is ON.

Figure 5.27 shows a sparse high amplitude peak as noise injected by the digital ground.

Next, the particle counting algorithm was implemented in the microcontroller as discussed in Chapter 4. The major problem while counting with the microcontroller was the fluctuating DC level of the signal with the flow. This makes the counts random in nature. To fix this, successive difference of the samples were measured to remove the dependence on the absolute value of the DC level. A feature was added which monitored the difference between the first 10,000 samples and then set the threshold difference value with the press of a button in the MSP430 Launchpad. At this moment, the flow was OFF. Next, the flow was turned ON and another button was pressed. The counts were then calculated by comparing the difference values of the next 30,000 samples against the threshold set during the previous

step. This method added robustness to the counting algorithm to deal with variations during different measurements. Consistent particulate counts were observed with varying flow rates. With increase in flow rate, it was expected that the number of particles crossing the threshold will increase per unit time and also, the particulate matter concentration will increase, generated by the nebulizer at higher flow rates. So, it was expected that the LCD display will show an increase in the particulate count as the flow rate was increased. To account for the sparse, high amplitude noise spikes, introduced by the digital ground of the microcontroller, 10 measurements were taken when the flow was OFF to find out the number of counts due to noise only. The mean number of counts indicated that 603 samples out of the 30,000 sample measurement acquisition were due to noise. This value was subtracted from the consequent measurements to account for the noise. The result of this experiment is shown by Figure 5.28. The sudden jumps in the number of counts can be attributed to non-uniform particle generation by the nebulizer. Another variable during the measurements was the water level in the nebulizer mixer chamber. The number of particles gets reduced quite a bit if the water level went down. So, the water level was replenished after every 2-3 measurements. However, this adds some randomness to the experimental conditions which might lead some offsets in the readings.

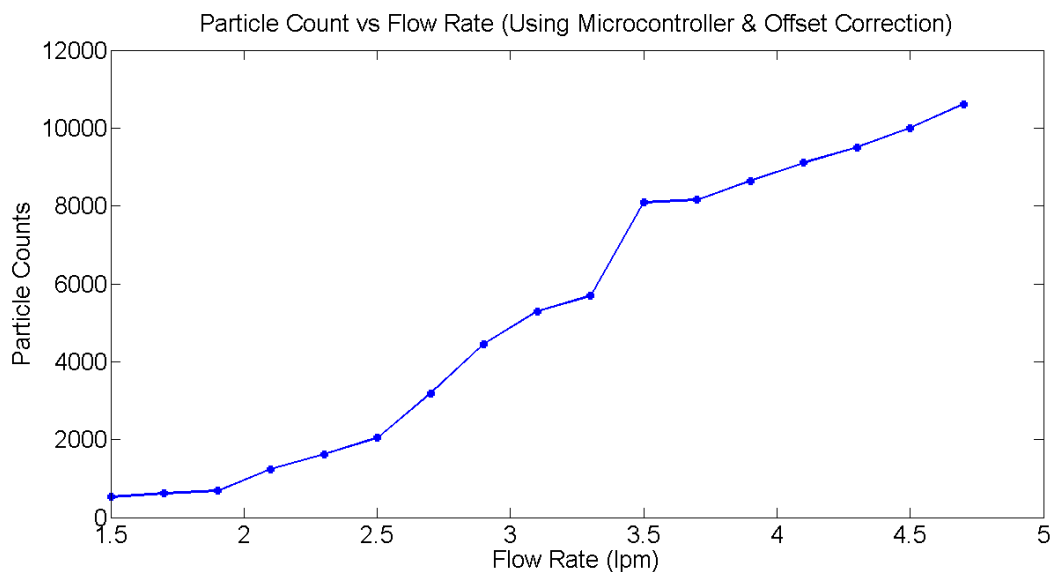


Figure 5.28 Result of test using microcontroller.

This concludes the experiments and summary of results conducted with the sensor. To summarize, sensor was able achieve a max SNR of 15.56 dB, with tests showing reliable detection of particle sizes ranging from 1.5 μm to 6.39 μm . Sensitivity to smoke particles is also demonstrated and a complete sensor system interfaced to a microcontroller and LCD display is demonstrated.

REFERENCES

1. Deval Pandya. (2010). "A low cost micro scale cyclone separator design and computational fluid dynamics analysis." A master thesis submitted to the Faculty of the Graduate School of The University of Texas at Arlington.
2. SKC Cyclone datasheet, <http://www.skcinc.com/prod/225-01-01.asp>.
3. Frederick R. Faxvog, "Detection of Airborne Particles Using Optical Extinction Measurements", Applied Optics, Vol. 13, No. 8, August 1974.
4. Nicolas Lelong, Laurent Vecellio, and Yann Sommer de Ge'licourt et al. (2013). "Comparison of Numerical Simulations to Experiments for Atomization in a Jet Nebulizer." Nov, Vol. 8, Issue 11, PLOS ONE.

APPENDICES

Appendix A – MATLAB Code

1. abcd factors calculation

```
function result = mie_abcd(m,x)
% Computes a matrix of Mie coefficients, a_n, b_n, c_n, d_n,
% of orders n=1 to nmax, complex refractive index m=m'+im",
% and size parameter x=k0*a, where k0= wave number
% in the ambient medium, a=sphere radius;
% p. 100, 477 in Bohren and Huffman (1983) BEWI:TDD122
% C. Matzler, June 2002
nmax=round(2+x+4*x^(1/3));
n=(1:nmax); nu = (n+0.5); z=m.*x; m2=m.*m;
sqx= sqrt(0.5*pi./x); sqz= sqrt(0.5*pi./z);
bx = besselj(nu, x).*sqx;
bz = besselj(nu, z).*sqz;
yx = bessely(nu, x).*sqx;
hx = bx+i*yx;
blx=[sin(x)/x, bx(1:nmax-1)];
blz=[sin(z)/z, bz(1:nmax-1)];
y1x=[-cos(x)/x, yx(1:nmax-1)];
hlx= blx+i*y1x;
ax = x.*blx-n.*bx;
az = z.*blz-n.*bz;
ahx= x.*hlx-n.*hx;
an = (m2.*bz.*ax-bx.*az)./(m2.*bz.*ahx-hx.*az);
bn = (bz.*ax-bx.*az)./(bz.*ahx-hx.*az);
cn = (bx.*ahx-hx.*ax)./(bz.*ahx-hx.*az);
dn = m.*(bx.*ahx-hx.*ax)./(m2.*bz.*ahx-hx.*az);
result=[an; bn; cn; dn];
```

2. Generalized Mie scattering amplitude calculation

```
function result = mie_S12(m, x, u)
% Computation of Mie Scattering functions S1 and S2
% for complex refractive index m=m'+im",
% size parameter x=k0*a, and u=cos(scattering angle),
% where k0=vacuum wave number, a=sphere radius;
% s. p. 111-114, Bohren and Huffman (1983) BEWI:TDD122
% C. Matzler, May 2002
nmax=round(2+x+4*x^(1/3));
abcd=mie_abcd(m,x);
an=abcd(1,:);
bn=abcd(2,:);
pt=mie_pt(u,nmax);
pin=pt(1,:);
tin=pt(2,:);
gn = mie_Gn(x);
```

```
n=(1:nmax);  
n2=(2*n+1)./(n.*(n+1)).*gn;  
pin=n2.*pin;  
tin=n2.*tin;  
S1=(an*pin'+bn*tin');  
S2=(an*tin'+bn*pin');  
result=[S1;S2];
```

Appendix B – MSP 430 Code

1. Overall Code with ADC and LCD integration

```

#include "msp430g2553.h"
#include "LCD.h"

int adc,p_adc; //Sets up an array of 100 integers and zero's the values
int cnt = 0;

volatile int FLAG = 0;

// Function prototypes
void adc_Setup();
void tmr_setup();
void GPIO_setup();
void adc_Sam100();

void main()

{
    int i,thresh; float avg = 0.0;
    char str[20];

    WDTCTL = WDTPW + WDTHOLD;           // Stop WDT
    adc_Setup();                         // Fucntion call for adc_setup
    tmr_setup();
    GPIO_setup();
    LCD_Setup();
    adc = 0;
    for(i=0;i<10000;i++)
    {
        p_adc = adc;
        adc_Sam100();
        avg += (adc - p_adc);
    }
    avg = avg/10000.0;
    thresh = (int)avg + 1;

    sprintf(str,"Thr: %d",thresh);
    writeStringToLCD(str);

    while((P1IN & BIT3));
    adc = 0;
    for(i=0;i<30000;i++)
    {
        p_adc = adc;

```

```

        adc_Sam100();

        if((adc - p_adc) > thresh)
            cnt++;

    }
    clearLCD();
    sprintf(str, "Val: %d", cnt);
    writeStringToLCD(str);
    while(1);
}

// ADC10 interrupt service routine
#pragma vector=ADC10_VECTOR
__interrupt void ADC10_ISR(void)
{
    __bic_SR_register_on_exit(CPUOFF);    // Clear CPUOFF bit from 0(SR)
}

// ADC set-up function
void adc_Setup()
{
    ADC10CTL1 = 0;
    ADC10CTL1 = INCH_4;                    // Repeat single channel, A0
    ADC10CTL0 = SREF_1 + ADC10SHT_0 + MSC + ADC10ON + ADC10IE + REFON;    //
    // Sample & Hold Time + ADC10 ON + Interrupt Enable

    ADC10CTL0 &= ~REF2_5V;
    ADC10DTC1 = 0x01;                      // 1 conversions
    ADC10AE0 |= BIT4;                      // P1.4 ADC option
select
}

void tmr_setup()
{
    TACTL = TASSEL_2 + MC_2;
}

// ADC sample conversion function
void adc_Sam100()
{
    ADC10CTL0 &= ~ENC;                    // Disable Conversion
    while (ADC10CTL1 & BUSY);            // Wait if ADC10 busy
    ADC10SA = (int>(&adc);                // Transfers data to next array (DTC
auto increments address)
    ADC10CTL0 |= ENC + ADC10SC;          // Enable Conversion and conversion start
    __bis_SR_register(CPUOFF + GIE);    // Low Power Mode 0, ADC10_ISR
}

```

```

}

void GPIO_setup()
{
    P1SEL &= (~BIT2);
    P1SEL &= (~BIT3);
    P1DIR |= BIT2;
    P1DIR &= (~BIT3);
    P1REN |= BIT2;
    P1REN |= BIT3;
}

```

2. LCD Library and code

```

/*
 * LCD.c
 *
 * Created on: 23-Jul-2014
 * Author: admin
 */

#include <msp430g2553.h>
#include "LCD.h"

#define LCD5110_SCLK_PIN BIT5
#define LCD5110_DN_PIN BIT7
#define LCD5110_SCE_PIN BIT0
#define LCD5110_DC_PIN BIT1
#define LCD5110_SELECT P1OUT &= ~LCD5110_SCE_PIN
#define LCD5110_DESELECT P1OUT |= LCD5110_SCE_PIN
#define LCD5110_SET_COMMAND P1OUT &= ~LCD5110_DC_PIN
#define LCD5110_SET_DATA P1OUT |= LCD5110_DC_PIN
#define LCD5110_COMMAND 0
#define LCD5110_DATA 1

#define SPI_MSB_FIRST UCB0CTL0 |= UCMSB // or UCA0CTL0 |= UCMSB (USCIA) or
USICTL0 &= ~USILSB (USI)
#define SPI_LSB_FIRST UCB0CTL0 &= ~UCMSB // or UCA0CTL0 &= ~UCMSB or USICTL0 |=
USILSB (USI)

unsigned char currXAddr = 0; //TODO this will be used for tracking current addr
unsigned char currYAddr = 0; //not implemented

char testBlock[8] = {0x00, 0x7F, 0x7F, 0x33, 0x33, 0x03, 0x03, 0x03};
char testBlock2[8] = {0x00, 0x18, 0x18, 0x18, 0x7E, 0x3C, 0x18, 0x00};

void LCD_Setup(void) {

```

```

    WDTCTL = WDTPW | WDTHOLD; // Stop watchdog timer
    BCSCTL1 = CALBC1_1MHZ;      // 1MHz clock
    DCOCTL = CALDCO_1MHZ;

    P1OUT |= LCD5110_SCE_PIN + LCD5110_DC_PIN;
    P1DIR |= LCD5110_SCE_PIN + LCD5110_DC_PIN;

    // setup USIB
    P1SEL |= LCD5110_SCLK_PIN + LCD5110_DN_PIN;
    P1SEL2 |= LCD5110_SCLK_PIN + LCD5110_DN_PIN;

    UCB0CTL0 |= UCCKPH + UCMSB + UCMST + UCSYNC; // 3-pin, 8-bit SPI master
    UCB0CTL1 |= UCSSEL_2;                       // SMCLK
    UCB0BR0 |= 0x01;                            // 1:1
    UCB0BR1 = 0;
    UCB0CTL1 &= ~UCSWRST;                       // clear SW

    _delay_cycles(500000);
    initLCD();
    clearLCD();
    //
}

void writeStringToLCD(const char *string) {
    while(*string) {
        writeCharToLCD(*string++);
    }
}

void writeCharToLCD(char c) {
    unsigned char i;
    for(i = 0; i < 5; i++) {
        writeToLCD(LCD5110_DATA, font[c - 0x20][i]);
    }
    writeToLCD(LCD5110_DATA, 0);
}

void writeToLCD(unsigned char dataCommand, unsigned char data) {
    LCD5110_SELECT;
    if(dataCommand) {
        LCD5110_SET_DATA;
    } else {
        LCD5110_SET_COMMAND;
    }
    UCB0TXBUF = data;
    while(!(IFG2 & UCB0TXIFG))
        ;
    LCD5110_DESELECT;
}

```

```

void clearLCD() {
    setAddr(0, 0);
    int c = 0;
    while(c < PCD8544_MAXBYTES) {
        writeToLCD(LCD5110_DATA, 0);
        c++;
    }
    setAddr(0, 0);
}

void setAddr(unsigned char xAddr, unsigned char yAddr) {
    writeToLCD(LCD5110_COMMAND, PCD8544_SETXADDR | xAddr);
    writeToLCD(LCD5110_COMMAND, PCD8544_SETYADDR | yAddr);
}

void initLCD() {
    writeToLCD(LCD5110_COMMAND, PCD8544_FUNCTIONSET |
PCD8544_EXTENDEDINSTRUCTION);
    writeToLCD(LCD5110_COMMAND, PCD8544_SETVOP | 0x3F);
    writeToLCD(LCD5110_COMMAND, PCD8544_SETTEMP | 0x02);
    writeToLCD(LCD5110_COMMAND, PCD8544_SETBIAS | 0x03);
    writeToLCD(LCD5110_COMMAND, PCD8544_FUNCTIONSET);
    writeToLCD(LCD5110_COMMAND, PCD8544_DISPLAYCONTROL |
PCD8544_DISPLAYNORMAL);
}

```

PCD8544.h

```

/*
 * LCD.h
 *
 * Created on: 23-Jul-2014
 * Author: admin
 */

#include "PCD8544.h"
#include "stdio.h"

#ifndef LCD_H_
#define LCD_H_

void LCD_Setup(void);
void writeStringToLCD(const char *string);
void writeCharToLCD(char c);
//void writeBlockToLCD(char *byte, unsigned char length);
//void writeGraphicToLCD(char *byte, unsigned char transform);
void writeToLCD(unsigned char dataCommand, unsigned char data);

```

```
void clearLCD();  
//void clearBank(unsigned char bank);  
void setAddr(unsigned char xAddr, unsigned char yAddr);  
void initLCD();  
  
#endif /* LCD_H_ */
```